Spectroscopy and Microscopy on the Formation of Zeolitic Imidazolate Frameworks

Spectroscopie en Microscopie van de Vorming van Zeoliet Imidazolaat Structuren

(met een samenvatting in het Nederlands)

Proefschrift

ter verkrijging van de graad van doctor aan de Universiteit Utrecht op gezag van de rector magnificus, prof. dr. G. J. van der Zwaan, ingevolge het besluit van het college voor promoties in het openbaar te verdedigen op 18 december 2017 des ochtends te 10.30 uur

door

Zafer Öztürk

geboren op 16 november 1983 te Ankara, Turkije

Promotor: **Prof. dr. ir. B. M. Weckhuysen**

This work was financially supported by the Netherlands Research School Combination - Catalysis (NRSCC) and a European Research Council (ERC) Advanced Grant (no. 321140).

Your presence is a heaven for me..

To my dearest parents,

Anneme ve Babama

Author: Öztürk, Zafer
Title: Spectroscopy and Microscopy on the Formation of Zeolitic Imidazolate Frameworks
ISBN: 978-94-6233-829-6
Printed by: Gildeprint-The Netherlands
Cover design: Karabulut, Fikret

TABLE of CONTENTS

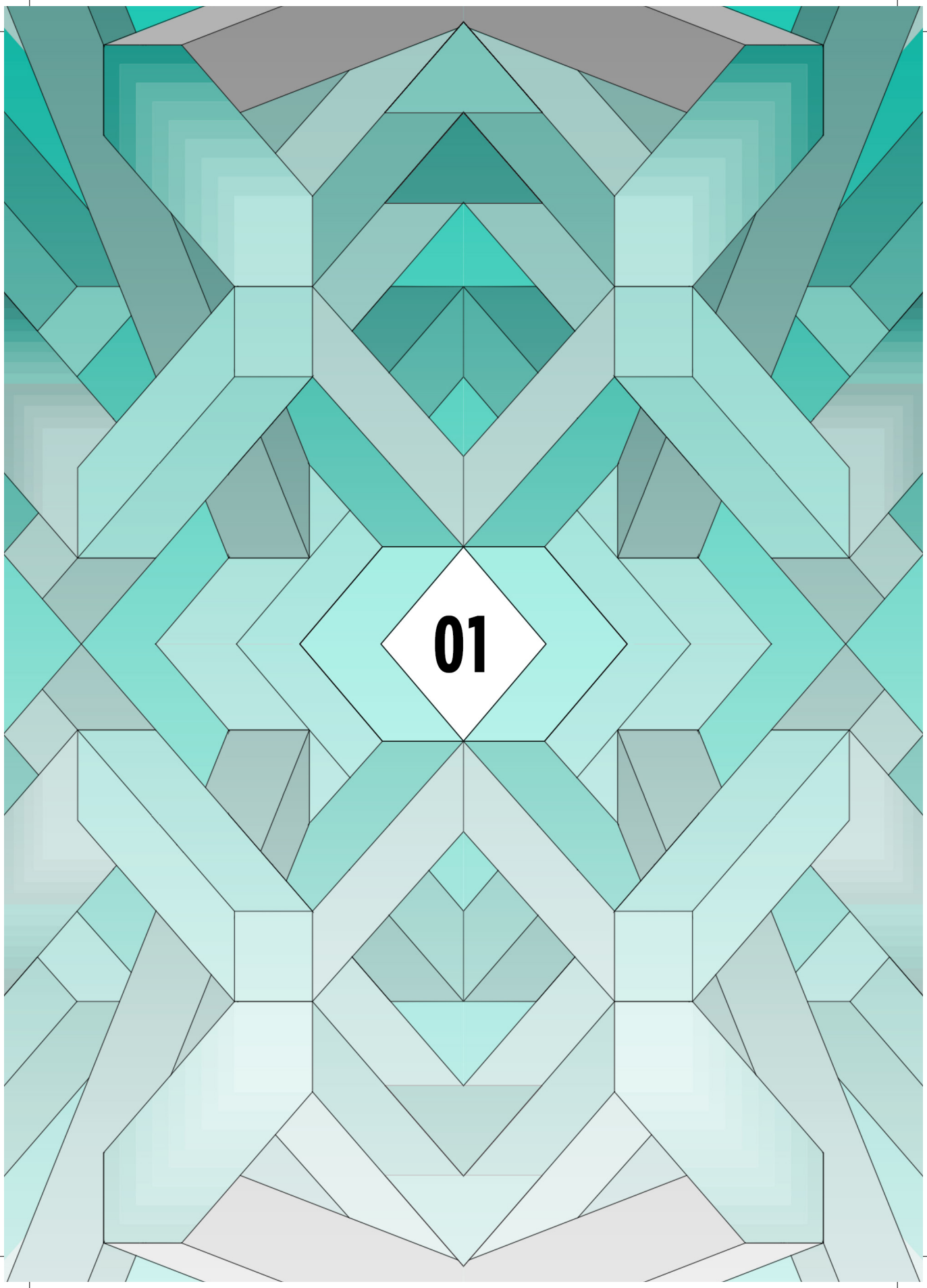
01

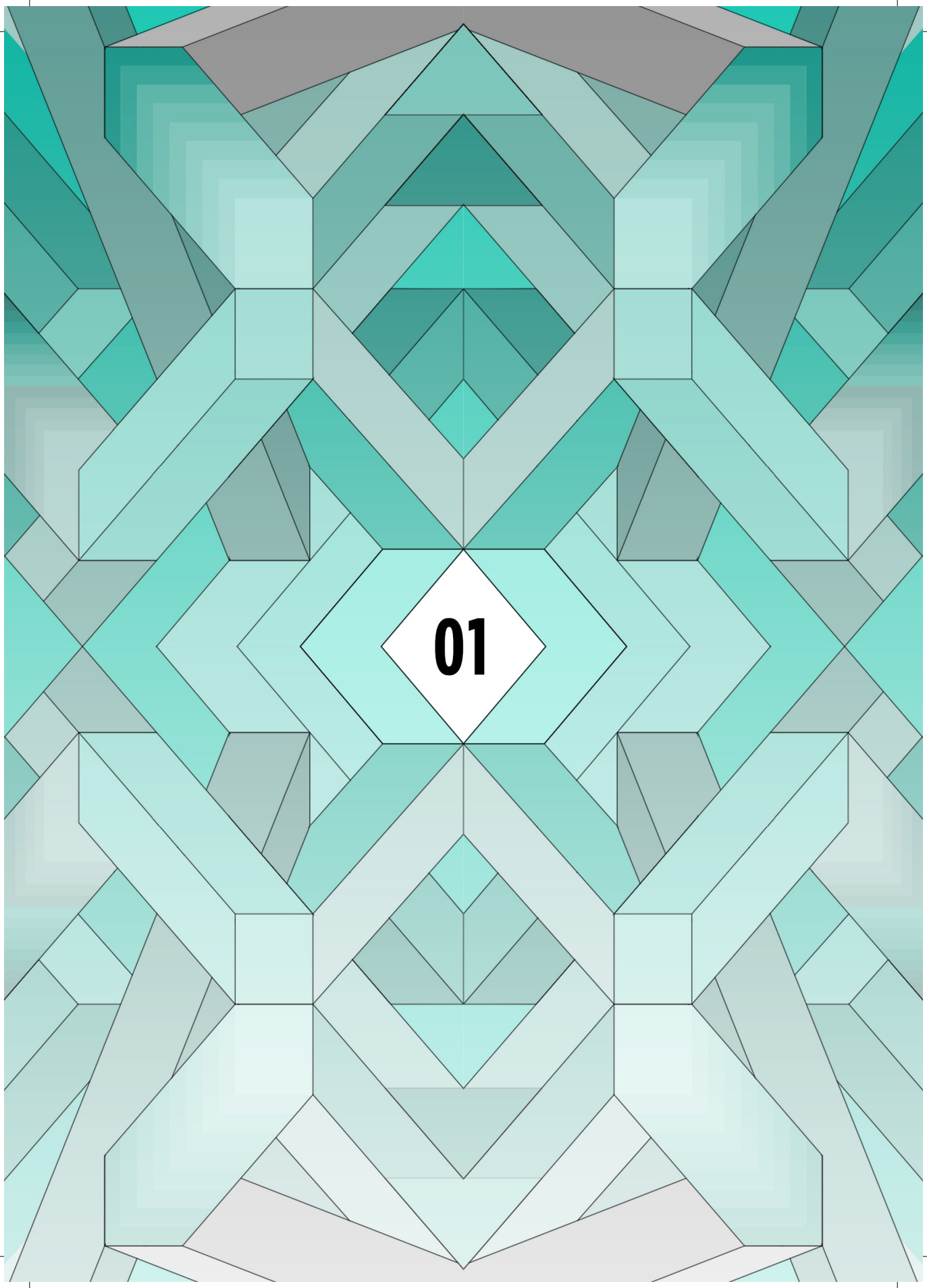
01

01

General Introduction

1.1. A Brief History: From Zeolites to Metal-Organic Frameworks

In today's world, porous materials are of great value. The ongoing interest for these porous materials can be attributed to their ability to react with the molecules at their surfaces. Most probably the most common examples of the porous materials family are activated carbon, aluminophosphates, alumina, titania, silica, and zeolites. The timeline for the evolution of these porous materials throughout the years are illustrated in Figure 1.1. These prototype porous solids can be distinguished in terms of their pore sizes and microporous (<2 nm pores), mesoporous (2-50 nm pores) and macroporous (>50 nm pores) are the three categories arising from the pore size of the solids. The performance of the porous material regarding a possible application is linked to how the size, shape and volume of the void space is distributed. Therefore, there has been a substantial interest in the preparation of porous materials with uniform distributions of these properties, which enables their use in advanced applications, such as gas separation and catalysis.[1]

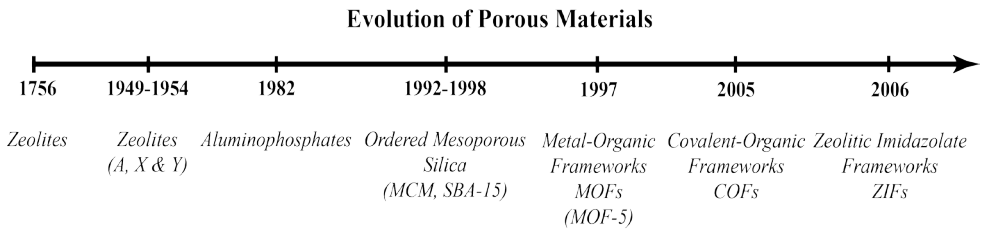

Figure 1.1. Timeline for the development of a variety of porous materials throughout years.

Among these porous materials, the class of zeolites stand out due to their porous structure, uniform pore sizes, high surface area and high thermal stability. Zeolites are naturally existing microporous aluminosilicate minerals with corner-sharing

AlO_4 and SiO_4 tetrahedra elementary structural units.[2–4] They have been widely used as sorbents, catalysts and ion-exchange materials.[2,5–7] In the early 1960s two important zeolites, namely faujasite X and Y, and later in the 1970s ZSM-5 (Zeolite Socony Mobil–5) have been commenced to be used as catalysts in the petrochemical industry for oil cracking in order to enhance the efficiency of this process.[8] By July 2017 today, 232 unique zeolite frameworks have been reported (International Zeolite Association).[9]

The success of synthesizing crystalline microporous aluminosilicates was followed by the emergence of another crystalline microporous materials namely, aluminophosphates in 1982.[10] Flanigen et al. reported the synthesis of the first zeolite analogue, microporous aluminophosphate solids containing no silica at all with an elementary structure unit of $AlPO_4$-n (n stands for the structural type).

In 1992, Mobil Corporation scientists discovered the silicate/aluminosilicate ordered mesoporous molecular sieves with exceptionally large uniform pore structures (MCM-41).[11] The discovery resulted in a significant amount of attention. The synthesis of this family of mesoporous materials is based on the combination of sol-gel and surfactant (templating) agents. In 1998, another type of ordered mesoporous silica material with hexagonal array of pores namely, Santa Barbara Amorphous no 15 (SBA-15) was discovered.[12] The discovery of the material has importance not only in terms of larger pores that it possesses but also in terms of thermal, mechanical and chemical resistance properties that it exhibits.

Another important milestone in the field of porous materials was initiated by the discovery of a new porous material, MOF-5, with a hybrid structure in the late 1990s, which was reported by Yaghi et al. and shown in Figure 1.2.[13] Porous coordination polymers (PCPs) also known as metal-organic frameworks (MOFs) have marked a new era owing to their inorganic-organic structures. MOFs are composed of organic ligands as linkers and inorganic coupling units, also known as secondary building units (SBU), as the connection points and ultimately resulting in a porous (micro to meso) framework. This hybrid structure enables the design of highly functional materials with desirable properties by combining a highly regular and well defined pore shape of inorganic porous materials with highly versatile properties of organic linkers.[14] According to the Cambridge Crystallographic Data Centre, 54,341 MOF structures have been reported so far.[15] MOFs have found applications in a wide variety of fields ranging from gas separation[16–18] to sensing[19,20] and from drug delivery[21,22] to catalysis[23,24].

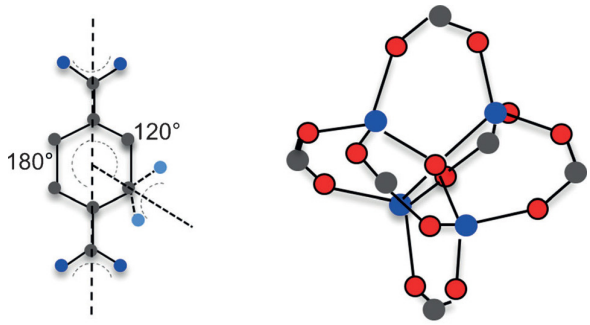

Figure 1.2. Metal–ligand coordination for a Benzene-1,4-dicarboxylate (BDC) linker where the M–BDC–M angle is around 120° resulting in an octahedral secondary building unit (SBU). M stands for Zn^{2+} metal ions for MOF-5. C: black, O: blue, metal: red. This figure has been adapted from literature.[13,25]

Owing to the industrial value of zeolites, MOF synthesis with zeolite topologies has become an important challenge to overcome. In the early development of MOF synthesis most of the synthesized MOFs are constructed from the linear benzenedicarboxylate (BDC) or benzenetricarboxylate (BTC; providing 120° bonding angles) linkers (Figure 1.2).[13] The accessible bonding angle was altered by the use of 5-membered ring imidazoles as organic linkers for which metal-imidazole based structures had been investigated intensely dating back to 1960[26] where copper-imidazole systems were studied. In 2002, Tian et al. explained the 145° bonding angles between adjacent metal centers upon use of an imidazole linker[27] and this gave rise to a remarkable attention for imidazolate-based materials. The angle of M-Im-M (where; M: metal, Im: Imidazolate) resembles the angle present in Si-O-Si in zeolites, as illustrated in Figure 1.3.

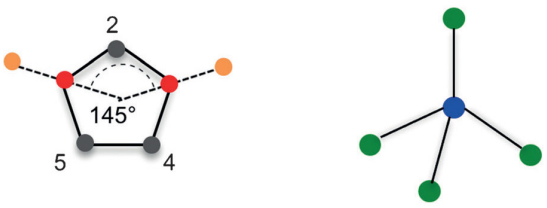

Figure 1.3. Metal–ligand coordination for imidazolate linkers where the M–Im–M angle is 145° resulting in a tetrahedral secondary building unit (SBU). C: grey, N: red and blue (left sketch and right sketch), metal: orange and blue (left sketch and right sketch). This figure has been adapted from literature.[25,27]

Further studies in the field of imidazolate based materials were performed by Park et al.. The term Zeolitic Imidazolate Frameworks (ZIFs) was used for the first time by Park et al. in 2006.[28] Meanwhile, another sub-class of MOFs, Covalent-Organic Frameworks (COFs) have been discovered in 2005.[29] COFs are porous and crystalline materials and they are composed of solely from light elements (H, B, C, N, and O), which are capable of forming strong covalent bonds with the organic building units.

ZIFs have emerged as a promising sub-class of MOFs during the last decade.[30] The received attention can be attributed to their similar coordination geometry compared to zeolites as mentioned before (Figure 1.3).[27,31,32] In addition to this, the attention for ZIFs can be further related to their permanent porosity, high chemical and thermal stability.[30] ZIFs are built up from transition metal ions (Co^{2+}, Zn^{2+}, Cu^{2+} or Fe^{2+}) tetrahedrally coordinated by bridging imidazolate linkers and the primary unit of the structure is $[M(Im)_4]$, where M stands for the transition metal and Im represents the imidazolate or a derivative.[33][34] ZIFs materials possessing zeolite-like tetrahedral topologies have been synthesized and reported previously.[28,32]

The advances in the MOF and ZIF field triggered the interest in the synthesis of these materials in the form of thin-films preferably anchored to an appropriate surface. Surface anchored crystalline thin-films of MOFs are called Surface-mounted Metal-Organic Frameworks (SURMOFs).[30,35,36] The coating of surfaces by the use of thin-films of crystalline porous materials offers the advantage of creating a maximum degree of flexibility required for their applications. This flexibility enables the modification of these substrates by giving the desired functionality in the pores of this molecular scaffold, which can host molecules such as dyes, metallic nanoparticles or molecular magnets.[35] Furthermore, these thin-films have found a wide variety of applications in the fields of gas separation,[37,38] QCM-based sensors,[39,40] and catalysis[41,42].

1.2. Synthesis of Metal-Organic Frameworks

As there is a growing knowledge in the synthesis of MOFs, it has started to become easy to synthesize MOFs with a plethora of desired chemical functionalities and structural topologies.[14] In this section, the principles of MOF synthesis will be the main concern. The main concept of synthesizing MOF is generating contact between the metal ions with more than one vacant or labile site and highly bridging ligand in order to form the desired open network structures. The framework obtained can be constructed from one-, two-, and three dimensional networks[43], as shown in Figure 1.4.

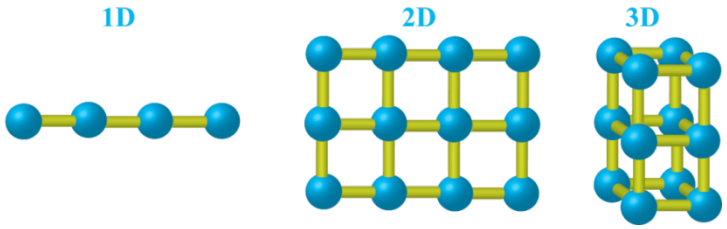

Figure 1.4. Basic illustration of porous coordination polymers with one, two and three dimensional networks where metal ions are represented with blue spheres and organic linkers are represented with yellow bars.

MOFs are crystalline hybrid materials with porous structures where the classical coordination bonds are formed between metal nodes, such as Zn^{2+}, and electron donors, such as carboxylates or amines. The MOF synthesis involves the self-assembly of these components, typically in N,N-dimethylformamide (DMF), ethanol or water. The resulting structures possess rigid pores, which are mostly resistant to the removal of solvent or other guest molecules during the evacuation of the pores; a process, which is called activation. [44] Activation of the as-synthesized MOFs is important not only in order to unlock the potential of the material for possible applications, but also to give the ultimate porous structure to the material.

The ability to vary both metal and organic linker for the synthesis of MOFs enables not only the chemical environment, but also the pore size to be tailored for a specific type of applications, which sets them prior to zeolites in terms of the flexibility they afford. The topology of the resulting framework is directly influenced by the coordination chemistry of the metal ion and the geometry of the organic linker under study.[45]

By taking the knowledge gained in the factors affecting the ultimate topologies, coordination environment of the metal, formation of inorganic building blocks and the geometry and functionality of the organic linker into account, one can deduce the parameters affecting the synthesis and one can direct the synthesis routes accordingly. Furthermore, one of the main concerns for the MOF synthesis is the establishment of the optimum synthesis conditions so that the organic linker does not decompose and the inorganic building blocks are formed in a well-defined manner. Furthermore, kinetics of the crystallization process should be suitable for the nucleation and the growth to take place with an ultimate desired phase formation. Additional parameters to investigate the MOFs formation fall in two categories: i.e., compositional and process parameters. The molar ratio of starting materials, pH of the mixture and choice of solvent belong to the compositional parameters, whereas reaction time, temperature and temperature range applied,

and pressure used fit in the process parameters category.[46]

There are many different synthesis routes and methods developed throughout the last two decades because of the fact that 1) the starting mixture does not necessarily yield the desired product and 2) the preparation of new functional materials suitable for advanced applications is vital.[45–47] The routes and methods applied not only may affect the reaction time, yields, morphology and particle size but also may not be compatible for their large-scale synthesis. Conventional synthesis still remains as one of the most used methods where the main principle of the method is based on conventional electric heating without any parallelization of reactions (Figure 1.5). For this method, the reaction temperature and the temperature range used are the main factors affecting the synthesis along with solvothermal and non-solvothermal reaction conditions.[48]

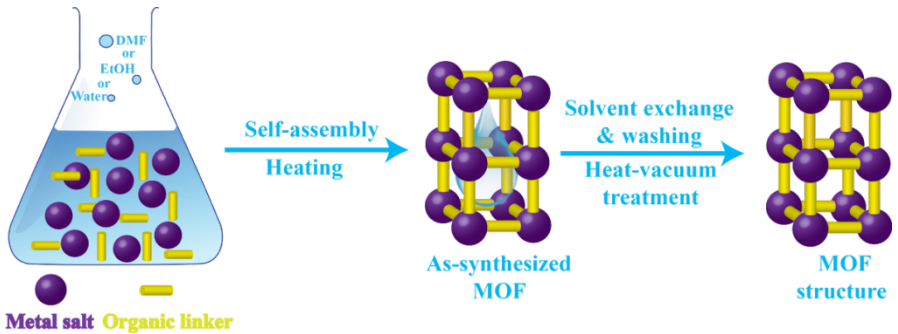

Figure 1.5. Illustration of a typical conventional MOF synthesis. Self-assembly is initiated by the heat applied for the formation of as-synthesized MOFs, which is followed by activation i.e. evacuation of the pores.

The solvothermal reaction can be described as a reaction occurring in a closed vessel system under autogenous pressure where the reaction temperature used is above the boiling point of the solvent used.[46,49] On the other hand, non-solvothermal reaction takes place under rather mild conditions such as under ambient pressure, below or at the boiling point of the solvent. Reactions taking place at room temperature can be placed in the non-solvothermal reaction category. The reaction temperature varies for both methods from room temperature to approximately 250 °C and as previously mentioned the energy required is generated through conventional electric heating.[47]

The prerequisite of the use of different synthesis methods stems from the need to synthesize new compounds, which cannot be synthesized through conventional synthesis. Moreover, the particle sizes, size distributions and morphology can also be

altered by using different routes. Microwave-assisted synthesis,[50] electrochemical synthesis,[40] mechanochemical synthesis,[51] and sonochemical synthesis,[52] are the methods applied and reported in the literature in order to diverse the possibilities for the synthesis (Figure 1.6).[46]

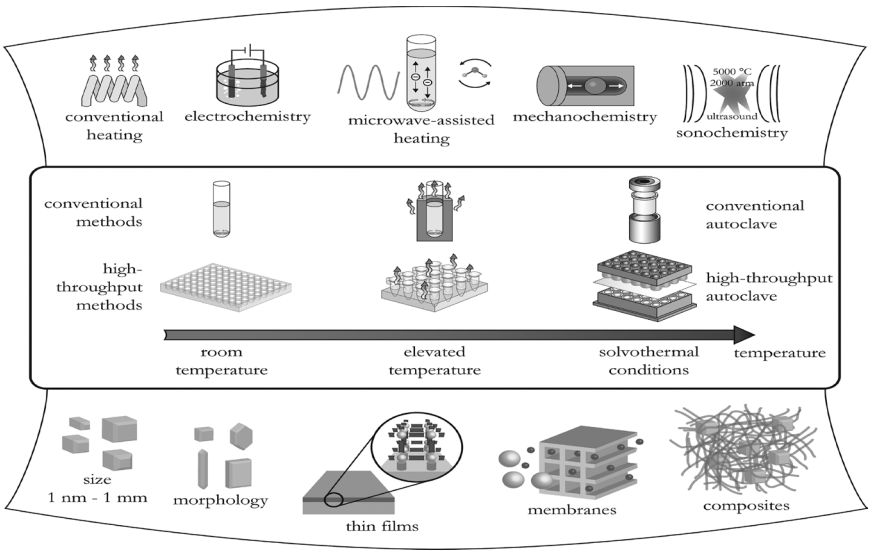

Figure 1.6. Alternative strategies (top) and conventional methods (bottom) developed for the synthesis of MOFs. This figure has been adapted from literature.[46]

1.3. Synthesis of Thin-Films of Metal-Organic Frameworks

As the knowledge acquired in the bulk synthesis and characteristics of MOFs has grown during the last two decades, more attention has been engaged in the growth of MOFs as thin-films owing to their promising properties for advanced applications as discussed in section 1.1. In addition to this, the idea of giving insights into the early growth stages of these porous crystalline hybrid materials has been the inspiration behind obtaining information on how the growth process takes place, which parameters affect the growth, or the direction of the growth. The possible answers to these questions are vital for attaining deeper knowledge in the formation mechanism of these materials, which can enable one to design MOFs with desired functionalities and as well as to establish synthesis, structure and property relationships. In this section, the emphasis will be given on the synthesis of these thin-film of MOFs with examples from literature.

MOF films can be divided into two sub-categories, which are polycrystalline films of MOFs and Surface-mounted Metal-Organic Frameworks (SURMOFs), as illustrated

in Figure 1.7. Polycrystalline films are formed through gathering of MOF crystals or particles with random orientation onto a substrate. The extent of randomness may vary and the surface of the substrate could be fully covered upon well inter-growth of crystals. To a certain extent, preferentially oriented films can be obtained if the attachment of the crystals is in one particular direction due to the favoured interactions with the surface. The resulting films possess a thickness in the micrometer range and the thickness is governed by the size of the MOF crystals under study. The second category is the aforementioned SURMOFs. They are constructed from nanometer range layers, which are flawlessly oriented in the direction of the growth. The properties of as-synthesized SURMOFs may show differences compared to their bulk analogues owing to their thickness and interactions with the surface upon close proximity. The intriguing properties of thin films open up new avenues towards structural or chemical modification of these materials for the desired purpose of applications due to their flexible natures of MOFs.[36]

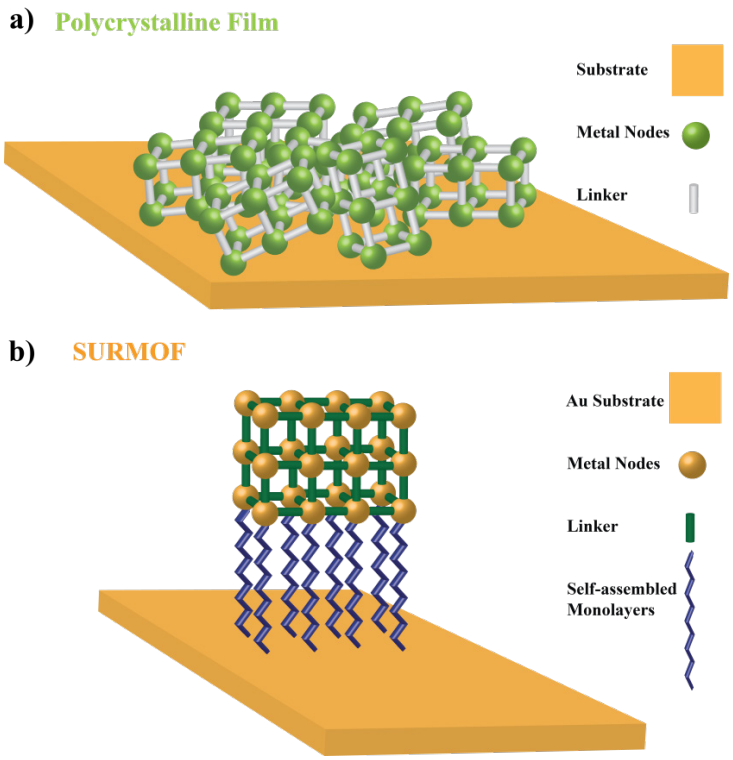

Figure 1.7. a) Polycrystalline and randomly oriented films of **a)** MOF and **b)** Surface-mounted perfectly oriented MOF multilayers (SURMOF).

Different methods for the deposition of MOFs onto solid substrates have been

proposed and reported in the literature. [35,36,53] The reason lying behind the differences in the proposed methods can be addressed to the type of the solid substrate used and the procedure used for the deposition method. To begin with, a wide variety of substrates can be utilized for the deposition ranging from metals to oxides and from polymers to textiles depending on the preferred application of the film or the selection of the deposition method. Depositions can be applied either onto a bare oxidic substrate or onto a modified surface through functionalizing with silane or thiolate-based self-assembled monolayers (SAMs) and hence, the choice of substrate is directly related to the deposition method used.

To illustrate, no surface functionalization is required for the most direct approach used for MOF deposition (functionalized substrates can also be used), which involves dipping of the substrate into a solution containing a suspension of MOF particles followed by evaporation of the solvent. This simple approach comes with the drawback of an unselective and unfixed attachment of MOF crystallites onto the substrate, which results in a restriction of their possible applications. On the other hand, in the layer-by-layer liquid epitaxy method, preferentially oriented growth can be achieved by surface functionalization with SAMs. Utilization of SAMs is of great importance as SAMs play a crucial role for directing the nucleation, orientation, as well as for the structure of the grown MOFs.[35,54–56]

For the preparation of polycrystalline films four main methods have been proposed and applied in the literature, which are direct synthesis, seeded growth, electrochemical approach and assembly of preformed MOF crystals. For the preparation of SURMOFs, there are two proposed and widely used methods available, namely liquid-phase epitaxy (layer-by-layer liquid epitaxy) and Langmuir-Blodgett (LB) layer-by-layer deposition methods. Table 1.1 summarizes different MOF films prepared with different techniques along with their characteristics and if applicable their application areas.[36]

Table 1.1. Overview of the MOF films prepared and adapted from literature.[36]

MOF Formula[a]	Substrate	Method	Characteristics, size or thickness	Application	Ref.
$[Cu_3(btc)_2]$ (HKUST-1)	alumina, silica wafers	mother solution at 120 °C	1µm		[57]
$[Cu_3(btc)_2]$ (HKUST-1)	α-alumina	seeded growth	10µm		[58]
$[Cu_3(btc)_2]$ (HKUST-1)	SAM on gold	mother solution at 25 °C	preferred orientation, 600 nm	sensing	[39,59]
$[Cu_3(btc)_2]$ (HKUST-1)	Copper mesh	mother solution at 120 °C	60 µm gas separation	gas separation	[60]
$[Cu_3(btc)_2]$ (HKUST-1)	Copper electrodes	electrochemically	2-20 µm	sensing	[40]
$[Cu_3(btc)_2]$ (HKUST-1)	Copper foil	galvanic displacement	crystallites 100-200 nm		[61]
$[Cu_3(btc)_2]$ (HKUST-1)	SAM on gold	liquid phase expitaxy	highly oriented,30-60 nm	mechanistic studies, diffusion coefficient	[62–64]
$[Cu_3(btc)_2]$ (HKUST-1)	micro-cantilever	stepwise deposition	100 nm	sensing	[65]
$[Cu_3(btc)_2]$ (HKUST-1)	Ag nanoparticles	stepwise deposition		sensing	[66]
$[Cu_3(btc)_2]$ (HKUST-1)	SAM on gold	gel layer	highly oriented		[67]
$[Cu_3(btc)_2]$ (HKUST-1)	α-alumina	seeded growth	25 µm	gas separation	[38]
$[Cu_3(btc)_2]$ (HKUST-1)	pulp fibers	mother solution at 85 °C			[68]
$[Cu_3(btc)_2]$ (HKUST-1)	glass slides	deposition of crystals	highly oriented crystals, 1µm		[69]
$[Cu_3(btc)_2]$ (HKUST-1)	SAMs on gold	deposition of crystals	highly oriented crystals, 0.5-1.5 µm		[70]

$[Cu_3(btc)_2]$ (HKUST-1)	copper slice	mother solution at 25 °C	5 µm		[71]
$[Cu_3(btc)_2]$ (HKUST-1)	copper slice	mother solution at 120 °C	1 µm	humidity sensor	[72]
$[Cu_3(btc)_2]$ (HKUST-1)	textile (polyester)	stepwise dosing of reagents	100 nm		[73]
$[Cu_3(btc)_2]$ (HKUST-1)	porous alumina	seeded growth	25 µm	gas separation	[74]
$[Cu_3(btc)_2]$ (HKUST-1)	polymer, oxide, polymer oxide beads	mother solution at 120 °C or 25 °C	crystallites 1-5 µm or 150 nm		[75]
$[Cu_3(btc)_2]$ (HKUST-1)	porous polymer monoliths	mother solution at 130 °C	crystallites 0.2 - 10 µm		[76]
$[Cu_3(btc)_2]$ (HKUST-1)	SAMs on gold	mother solution (precipitatingsolvent)	highly oriented 90 nm		[77]
$[Cu_3(btc)_2]$ (HKUST-1)	SAMs on gold	liquid phase expitaxy	highly oriented 1 µm	mechanic studies	[78]
$[Cu_3(btc)_2]$ (HKUST-1)	SAMs on gold	liquid phase expitaxy	oriented	optical	[79]
$[Cu_3(btc)_2]$ (HKUST-1)	silica wafer	spin coating	175 nm		[80]
$[Cu_3(btc)_2]$ (HKUST-1)	Functionalized silica wafer	layer-by-layer	70-120 nm	Dielectric and optical properties	[81]
$[Cu_3(btc)_2]$ (HKUST-1)	SAMs on gold electrodes or silica micro-cantilevers	crystallization direct synthesis	highly oriented 500 nm	sensing	[82]
$[Cu_3(btc)_2]$ (HKUST-1)	FTO	electrophoretic deposition (direct synthesis)	4-5 µm		[83]
$[Cu_3(btc)_2]$ (HKUST-1)	FTO	layer by layer		photovoltaic	[84]
$[Cu_3(btc)_2]$ (HKUST-1)	alumina, gold electrodes of QCM	drop coating	1-2.5 µm	sensing	[85]
$[Cu_3(btc)_2]$ (HKUST-1)	Conducting polyaniline Pt electrode	mother solution	40-50 µm		[86]

$[Cu_3(btc)_2]$ (HKUST-1)	polymer hollow fiber	pressure-assisted room temperature growth	3 µm	gas separation	[87]
$[Cu_3(btc)_2]$ (HKUST-1)	Silica pre-patterned with Pt	liquid phase epitaxy	100 nm	electrical conductivity	[88]
$[Cu_3(btc)_2]$ (HKUST-1)	quartz	liquid phase epitaxy		optical	[89]
$[Cu_3(btc)_2]$ (HKUST-1)	gold-coated polyethylene terephthalate	liquid phase epitaxy	130 nm		[90]
$[Cu_3(btc)_2]$ (HKUST-1)	modified silica wafer	liquid phase epitaxy automated spray system	80-135 nm	optical sensing	[91]
$[Cu_3(btc)_2]$ (HKUST-1)	ALD of alumina coated polypropylene fibers	layer by layer	117 nm	adsorption	[92]
$[Cu_3(btc)_2]$ (HKUST-1)	quartz	dipping robot, layer by layer	highly oriented 100 nm	optical	[93]
$[Cu_3(btc)_2]$ (HKUST-1)	SAMs on magnetic silica microparticles	liquid phase epitaxy		separation	[94]
$[Cu_3(btc)_2]$ (HKUST-1)	quartz	spin coating and thermal treatment	41-856 nm		[95]
$[Cu_3(btc)_2]$ (HKUST-1)	SAMs on gold	liquid phase epitaxy		optical	[96]
$[Cu_3(btc)_2]$ (HKUST-1)	alumina	spin coating in a liquid phase epitaxy manner	3 µm		[97]
$[Cu_3(btc)_2]$ (HKUST-1)	SAMs on gold, QCM sensors	liquid phase epitaxy	70 nm		[98]
Cu-TCPP	gold/silver waver or quartz	modular assembly	highly oriented 15 nm		[99]
Cu-TCPP	SAMs on gold	layer by layer	40-115 Å		[100]
Cu-UHM-3 (dmcdip)	SAMs on gold	liquid phase epitaxy automated spray system	highly oriented 80 nm	gas adsorption and separation	[101]

$Cu_2(bdc)_2 \cdot x H_2O$	SAMs on gold	spin coating in a liquid phase epitaxy manner	highly oriented 140-220 nm	adsorption	[97]
$Cu_2(bdc)_2 \cdot x H_2O$	Porous stainless steel, silica, glass	spin coating in a liquid phase epitaxy manner			[97]
Cu-TCNQ	SAMs on gold and FTO	liquid phase epitaxy, e-beam lithography	400 nm	conductance	[102]
$[Zn_4O(bdc)]$ (MOF-5)	oxides wafers, SAM on gold	mother solution, 25°C	500 nm		[103], [104]
$[Zn_4O(bdc)]$ (MOF-5)	graphite / AAO	mother solution in MW	preferred orientation, 5 µm		[105]
$[Zn_4O(bdc)]$ (MOF-5)	graphite / AAO	seeded growth	preferred orientation, 30 µm	gas separation	[37]
$[Zn_4O(bdc)]$ (MOF-5)	α-alumina	mother solution (solvothermal)	25 or 85 µm	gas separation	[106]
$[Zn_4O(bdc)]$ (MOF-5)	alumina wafer photoresist on silicon	seeded growth	crystallites 20-100 µm		[107]
$[Zn_4O(bdc)]$ (MOF-5)	SAMs on gold electrodes or silica micro-cantilevers	crystallization direct synthesis	highly oriented 500 nm	sensing	[82]
$[Zn_4O(bdc)]$ (MOF-5)	quartz	solvent evaporation	micro-sized	fluorescence	[108]
$[Zn_4O(bdc)]$ (MOF-5)	SAMs on gold-coated (QCM)	Liquid Phase Hetero-epitaxial Growth	0.5- 1 µm	adsorption	[109]
$(Et_3NH)_2$-MOF-5	solid phase micro-extraction (SPME) fiber	in situ cathodic electrodeposition	12.5 µm	extraction	[110]
$Zn_2(N_3\text{-}bdc)_2(dabco)$	SAMs on gold	liquid phase epitaxy	highly oriented	post-synthetic modification	[111]
IRMOF-3 $Zn_4O(H_2N\text{-}bdc_3)$	silica wafer	spin coating	175 nm		[80]
ZIF-8	silica wafers	dip coating in mother solution	1 - 5 µm	sensing	[112]

ZIF-8	silica wafers	dip coating from colloidal solution	40 – 500 nm	sensing	[113]
ZIF-8	porous titania	mother solution in MW	20 – 30 nm	gas separation	[114], [115]
ZIF-8	α-alumina	seeded growth	preferred orientation, 5-12 µm	gas separation	[116]
ZIF-8	tubular α-alumina	seeded growth	5 or 9 µm	gas separation	[117]
ZIF-8	α-alumina	mother solution at 120 °C	20 µm	gas separation	[118]
ZIF-8	flexible nylon membrane	slow diffusion (contra diffusion)	16 µm	gas separation	[119]
ZIF-8	silica wafers	solvent free synthesis (ZnO)	1-5 µm		[120]
ZIF-8	Si/silica/QCM	atomic layer deposition / magnetron sputtering / microwave synthesis	80 – 100 nm	adsorption	[121]
ZIF-8	APTES functionalized quartz capillary	flow method	3.4 µm		[122]
ZIF-8	Poly-vinylidene fluoride (PVDF) hollow fibers	secondary growth	2 µm	separation	[123]
ZIF-8	SAMs on α-alumina	liquid phase epitaxy dipping robot	500 nm	gas separation	[124]
ZIF-8	alumina	spin coating in a liquid phase epitaxy manner	3 µm	gas separation	[97]
ZIF-8	2-D colloidal crystal arrays,	direct synthesis	500 nm	sensing, separation	[125]
ZIF-8	gold	direct synthesis	100-350 nm		[126]
ZIF-7	porous alumina	seeding then mother solution in MW	preferred orientation, 1.5 µm	gas separation	[127–129]
ZIF-7	α-alumina	mother solution at 120 °C	1 µm	gas separation	[118]
ZIF-9	Poly-tetra-fluoroethylene (PTFE)	plasma polymer coating			[130]

ZIF-22	porous titania	mother solution at 150 °C	40 µm	gas separation	[131]
ZIF-67	gold	direct synthesis	250-900 nm		[126]
ZIF-69	α-alumina	mother solution (solvothermal)	preferred orientation, 50 µm	gas separation	[132]
ZIF-90	α-alumina	mother solution at 100 °C	20 µm	gas separation	[133], [134]
$[Cu_2(pzdc)_2(pyz)]$	silica wafers	dip coating in mother solution	preferred orientation, 3 µm		[135]
SIM-1	α- and γ-alumina beads	mother solution at 85 °C	15 µm (α-Al_2O_3 only)	hetero-geneous catalysis	[41]
SIM-1	tubular α-alumina	mother solution at 85 °C	25 µm	gas separation	[136]
NAFS-1	silica wafers	Langmuir - Blodgett method	highly oriented, 21 nm		[137]
NAFS-2	gold, silicon	Langmuir - Blodgett method	highly oriented, 40 nm		[138]
MOF-508	SAMs on gold	liquid phase epitaxy	highly oriented, 40 nm		[139]
$[Cu_2(ndc)_2(dabco)]$	oxides wafers	stepwise dosing of reagents	preferred orientation, 120 nm		[140]
$[Cu_2(ndc)_2(dabco)]$	porous alumina	stepwise dosing of reagents	30 µm	gas separation	[141]
$Cu_2(atbdc)_2(dabco)$	SAMs on gold	liquid phase epitaxy	highly oriented, 80 nm	adsorption	[96]
$[M(L)(dabco)_{0.5}]$, M=Cu,Zn; L=ndc,F_4bdc	SAMs on gold	liquid phase epitaxy	preferred orientation, 20 - 50 nm		[142-144]
CPO-27-M, M=Ni,Co,Mg, Mn,Zn	alumina wafers	mother solution at 110 °C	2 - 20 µm		[145]
MIL-47	Polyacrylo-nitrile	mother solution in MW	several micrometers		[146]
IRMOF-3/ MOF-5	Glass slides	mother solution at 105 °C	10 µm		[147]
IRMOF-3/ MOF-5	porous alumina	mother solution at105 °C	10 µm	separation	[148]
$[Mn(HCOO)_2]$	α-alumina, graphite	mother solution at 115 °C	preferred orientation, 300 µm		[149]

[Al(bdc)] MIL-53	porous alumina	seeding, then mother solution at 220 °C	8 µm	liquid separation	[150]
[Al(bdc)] MIL-53	FTO	electrophoretic deposition (direct synthesis)	4-5 µm		[83]
MIL-96	porous alumina	seeded growth	10 µm	liquid separation (pervaporation)	[150]
$[Al_4(OH)_2(OCH_3)_4(H_2N\text{-}bdc)_3].H_2O$ (CAU-1)	SAMs on gold	mother solution at 25 °C	highly oriented, 150 nm	sensing	[151]
$[Zn_2(bdc)_2(dabco)]$	oxide wafers	mother solution at 120 °C	1 µm		[57]
$[Cu(hfipbb)(H_2hfipbb)_{0.5}]$	porous alumina	seeded growth	preferred orientation, 20 µm	gas separation	[152]
In(OH)(bdc)	silicon wafer stainless steel plate aluminium slice α-alumina	seeded growth	5 µm		[153]
Fe-MIL-88B	SAMs on gold	mother solution at 25 °C	highly oriented, 500 nm	sensing	[154, 155]
Fe-MIL-88B-NH_2	SAMs on gold	slow diffusion (gel layer)	preferred orientation, 40 nm		[67]
Fe-MIL-88B-NH_2	silica wafers	spin coating	50-500 nm	sensing	[156]
$Fe(pz)[Pt(CN)_4]$ $Fe(pz)[M(CN)_4]$ (M = Ni, Pd	SAMs on Au/ Cr/Si	liquid phase epitaxy	highly oriented		[157–159]
Fe(btc), Ni(btc), Fe/Ni(btc)	Nickel Foam (NF)	electrochemical deposition	5 µm	oxygen evolution	[98]
MIL-89	silica wafers	dip coating from colloidal solution	40-80 nm	sensing	[160]
MIL-101 (Cr)	silica wafers	dip coating from colloidal solution	20-100 nm	sensing	[161]
MIL-101 (Cr)	α-alumina, cordierite monoliths	Seeded growth	10 µm	hetero-geneous catalysis	[42]
$Zn_3(btc)_2$	zinc slide	mother solution at 140 °C	20 µm	sensing	[162]
$Sr_{1-x}Eu_x(Im)_2]$	functionalized alumina	in-situ coating	100 nm up to 1.5 mm	luminescence	[163]

$Sr_{1-x}Eu_x(Im)_2$]	Functionalized Silica wafers and indium tin oxide-coated (ITO) glass	Layer-by-layer	25-50 nm	fluorescence	[164]
[5,15-Bis[4-(pyridyl) ethynyl]-10,20-diphenyl porphinato] zinc(II)	Poly imides	In-situ interfacial polymerization	50–150 nm	Organic Solvent Nano-filtration	[165]
ZIF-8 NH_2-MIL-53(Al) MIL-53(Al) MIL-101(Cr)	Fluorine-doped Tin Oxide conductive glass (FTO)	electrodeposition	500 nm	luminescent sensor	[166]
[[Eu(HBPTC) $(H_2O)_2$]· 2DMF}$_n$]	ITO	spin coating		luminescence	[167]
MOF-253–Ln Ln(OH)(bpydc) (Ln= Eu, Tb, Sm)	Quartz	post synthetic method	100 nm	luminescence	[168]
MOF-253–Ln Ln(OH)(bpydc) (Ln= Eu, Tb, Yb)	α-alumina, silica	seeded growth	0.5 - 10 μm	thermo-chromism	[169]
Cu_2(EBTC) $(H2O)_2$.[G] [G]= DMF, DMSO and H_2O	FTO	electrophoretic deposition (direct synthesis)	4-5 μm		[83]
Cu_2(EBTC) $(H2O)_2$.[G] [G]= DMF, DMSO and H_2O	QCM	layer-by-layer	100 nm		170]
UiO-66 Zr(bdc)	Titania coated nanofiber	direct synthesis		degradation	[171]
UiO-66 UiO-66-NH_2 UiO-67	FTO	electrophoretic deposition (direct synthesis)	4-5 μm		[83]
NU-1000	SAMs modified gold coated QCM	liquid phase epitaxy		adsorption	[172]
$(Zr_6(\mu_3–OH)_8$ $(OH)_8(TBAPy)_2)$	SAMs modified gold	liquid phase epitaxy		isomerization	[173]

$(Zr_6(\mu_3–OH)_8(OH)_8(TBAPy)_2)$	functionalized glass	layer by layer and doctor blade coating			[174]
$Cu_2(bdc)_2$ (AzoBipyB) $Co_3(ndc)_3DMF_4$	tin oxide-coated (FTO) glasses	layer-by-layer		light harvesting	[175]
Co-MOF Co(bdc) Co(ndc)	SAMs modified gold coated QCM	Layer-by-layer QCM cell	80 nm	adsorption	[176]
$Cu_2(Dcam)_2$ (BiPy) $Cu_2(Dcam)_2$ (dabco)	glass	direct spin coating		sensing	[177]
$(Zn_8(ad)_4(bpdc)_6O\cdot 2Me_2NH_2)$	SAMs on gold coated QCM	liquid phase epitaxy		adsorption	[178]
Zn-DE [Zn4O(3,5-dialkyl carboxy pyrazolate)3] Zn-MI [Zn4O(3-methyl-5-isopropyl-4-carboxy pyrazolate)3]	SAMs on interdigitated electrodes (IDEs)	direct growth		sensing	[179]

[a] bdc=1,4-benzene dicarboxylate; ndc=1,4-naphthalene dicarboxylate; btc = benzene-1,3,5-tricarboxylate; H_2hfipbb = 4,4′-(hexafluoroisopropylidene)-bis(benzoic acid); dabco=1,4-diazabicyclo(2.2.2)octane; pyz=pyrazine; F_4bdc=tetrafluoro-1,4-benzenedicarboxylate;pzdc=pyrazine-2,3-dicarboxylate;4,4′-bipy=4,4′-bipyridine; TCPP=5,10,15,20-tetrakis(4-carboxyphenyl) porphyrin;(bptc=benzophenone-3,3’,4,4’-tetracarboxylate); (bpydc=2,2’-bipyridine-5,5’-dicarboxylic);1,1-Ethynebenzene-3,3’,5,5’-tetracarboxylate;H_4TBAPy=1,3,6,8-tetrakis(p-benzoic acid) pyrene;AzoBipyB=4,4’-(2-(phenyldiazenyl)-1,4-phenylene)dipyridine)];Dcam=(1R,3S)-(+)-Camphoric acid; BiPy=4,4’-bipyridine; dmcdip=5,5’-(dimethylsilanediyl)diisophthalic acid; APTES=3-aminopropyltriethoxysilane;bpdc=biphenyl-4,4’-dicarboxylic acid; Ad= adenine; fum=fumarate; TCNQ= tetracyanoquinodimethane.

1.3.1. Synthesis of Polycrystalline Films of Metal-Organic Frameworks

1.3.1.1. Direct Synthesis

This straightforward deposition method can be applied either onto a bare substrate or onto a functionalized surface. There are a few strategies developed for this method. The in-situ crystallization strategy is one of the widely applied direct synthesis method and illustrated in Figure 1.8. This strategy involves solvothermal synthesis conditions where the substrate is placed into a reaction vessel (autoclave) preferably vertically in order to avoid sedimentation. The reaction mixture is heated to the desired temperature (in a conventional or microwave oven) under autogenous pressure. In-situ crystallization takes place on the surface of the substrate or in the solution and results in anchoring of the MOF crystals onto the substrate. Crystalline, dense and homogeneous MOF films with micrometer thickness can be applied with this method either on a functionalized surface,[57] a metal slice [60,72] or even on a polymer[146]. However, there are limitations to this strategy as high reaction temperature, chemically aggressive reaction mixture and pressure should allow substrate to maintain its stability.[36]

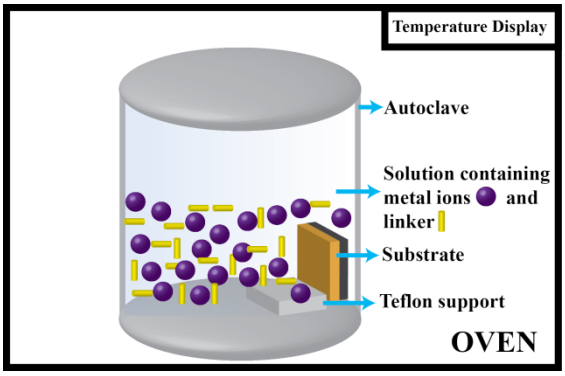

Figure 1.8. Illustration of the direct growth method under solvothermal conditions. The substrate is placed vertically in order to avoid sedimentation.

Owing to the sensitive nature of many substrates at elevated reaction temperatures, alternative direct synthesis strategies were developed. Room temperature deposition from a solvothermal mother liquor comes into prominence because of the benefits this strategy offers, which are the ease of the deposition and preservation of the stability of a substrate.[36,180] As the name implies, this approach involves deposition of MOFs from a solvothermal mother solution after the reaction onto the bare or functionalized surface again. To illustrate this, the reaction mixture for the MOF synthesis is prepared and the solvothermal reaction is allowed to take

place. After the reaction, the mixture is cooled down to room temperature and filtered, then the substrates are immersed into the mother liquor solution for the deposition. This approach was first introduced by Hermes et al. where they show the selective growth of MOF-5 on a functionalized Au (111) surface.[103] Later on this method was utilized also for the growth of different MOFs. [59,145,155] The drawback of this strategy is the long reaction times required for the synthesis of MOFs and the poor morphology of the MOF crystals.[36] Moreover, the films prepared are often discontinuous.[36,46] Other strategies that can be covered in this section are dip-coating into the mother solution,[135] slow diffusion of reactants,[181] and controlled deposition of crystals at the surface[69].

1.3.1.2. Seeded Growth

Seeded growth, also referred to as the two-step crystallization method has been previously reported for zeolite film preparation.[182] The main requisite of this method for the deposition of MOFs onto a suitable substrate is the attachment of seeds onto the substrate, which is followed by crystal growth (secondary growth) as shown in Figure 1.9. Crystal growth sites can be generated by the use of seeds and this results in control over the crystal growth.[25,36,183]

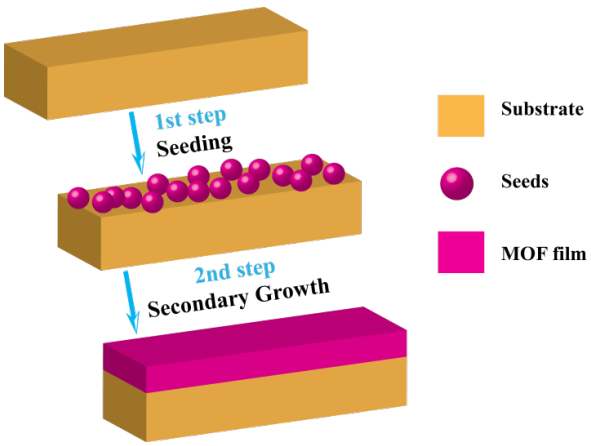

Figure 1.9. Illustration of the seeded growth (two-step crystallization) method.

Although not as simple as direct synthesis, seeded growth exhibits better control over the crystal orientation and thickness.[25,30,36,183] In the literature, as seeds MOF nano crystals,[152] non-MOF particles,[107] coordination polymers,[58] and MOF thin-films[140,147] have been used. For the seeding of the substrates, rubbing, dip coating, wiping, spin coating and heating are the techniques commonly used.[184] Even though this approach has drawbacks in terms of substrate stability under solvothermal

conditions, dense and oriented films of MOFs were shown to be prepared through the secondary growth method.[140] Furthermore, this method offers advantages over direct synthesis by producing mostly continuous MOF films.[46]

1.3.1.3. Electrochemical Synthesis

This method was originally pioneered by scientists at BASF for the large-scale preparation of MOF powders.[185] The basic principle of this method is the production of metal ions upon oxidation of a metal electrode in a solution where an organic linker and a conduction salt are present. In a paper by Ameloot et al., the authors managed to prepare coatings of HKUST-1 (Hong Kong University of Science and Technology-1).[40] HKUST-1 has been one of the widely studied MOFs and is composed of Cu^{2+} ions as metal nodes and tridentate 1,3,5-benzene tricarboxylic acid (trimesic acid / btc) as an organic linker.[186] In the paper reported, Cu^{2+} ions were produced upon applying voltage on the copper electrode where in the same solution trimesic acid was present. Densely packed, homogeneous MOF layers were formed in a short time with a possibility to vary the thickness of the coatings. Furthermore, the crystal size was controlled by changing two factors; changing the voltage applied in order to change the concentration of the metal ions introduced to the solution and changing the amount of water. As the applied voltage was increased, more Cu^{2+} ions were introduced, hence smaller crystals were obtained in the coatings. On the other hand, as the water content was increased nucleation was slower and bigger crystals were yielded in the coatings.[40] Although this method offers a lot, so far only HKUST-1 coatings were possible to be prepared by this method.

1.3.1.4. Assembly of Preformed MOF Crystals

MOF films can also be prepared by another approach namely, assembly of preformed objects. These preformed objects are usually nanocrystals and colloids. The main principle of this method is to prepare well-defined MOF particles and their deposition onto a substrate by dip-coating as illustrated in Figure 1.10.

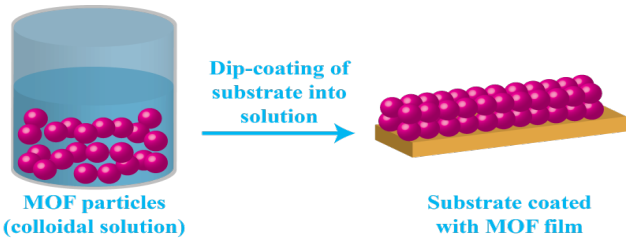

Figure 1.10. Illustration of the preparation of MOF films by assembly of preformed MOF crystals.

There has been papers both on the synthesis of MOF nanocrystals,[160] and on the preparation of MOF films based on this assembly of preformed MOF crystals.[113,160,161] This method allows one to control the particle size as well as the thickness of the as-prepared films. Dip-coating can be repeated as the preferred thickness is obtained. Furthermore, MOF films prepared using this method possess micro- and also mesoporosity owing to the poor anchoring of these films to the substrate. Therefore, these films can be used in certain fields requiring diffusion and permeation properties. However, the latter property comes with the limitation for other kind of applications whereby rigid attachment of the films to the substrate is required.[14,36]

1.3.2. Synthesis of Surface-Mounted Metal-Organic Frameworks

1.3.2.1. Layer-by-layer Liquid Epitaxy

In 1997, the layer-by-layer (LbL) technique was introduced for the fabrication of multilayer structures of poly-ions or other charged molecular or colloidal objects by Decher.[187] The main principle of the process is the adsorption of components from solution to the substrate and therefore, the method is not dependent on the nature of the substrate.[187] As component materials, polymers,[188–190] biomaterials,[191,192] inorganic substances,[193–195] and supramolecular assemblies,[196,197] have already been utilized in the LbL method. The knowledge gained in the fabrication of polyelectrolytes was later on transferred to coordination polymers and in 2007 Wöll et al. reported the use of the LbL approach for the growth of MOF thin-films on a substrate.[62] HKUST-1 was chosen for the demonstration of the method to prepare a thin-film of a MOF on a gold substrate modified with self-assembled monolayers (SAMs). SAMs used in this study were carboxylic acid terminated (functional group). Highly crystalline MOF films possessing the HKUST-1 bulk structure was successfully prepared by the LbL approach.[62] One of the important features of this method developed by Wöll et al. is that the thin-films obtained mostly have preferred or desired orientation due to the use of self-assembled monolayers (SAMs).

The garnered attention for SAMs can be ascribed to their ability to tailor surface properties, such as wetting behaviour, adhesion, corrosion and lubrication. In addition to this, SAMs are of great importance in order to gain further insights into self-organization, structure-property relationship and interfacial phenomena as one can tailor both the head and tail group of the SAMs under study.[198] Furthermore, the quality of the surface is so high upon functionalization. The thiol-based SAMs, such as alkane-thiols, can be prepared on gold surfaces and this system has been widely investigated.[55,199,200]The representation of thiol-based SAMs on gold is

shown in Figure 1.11.

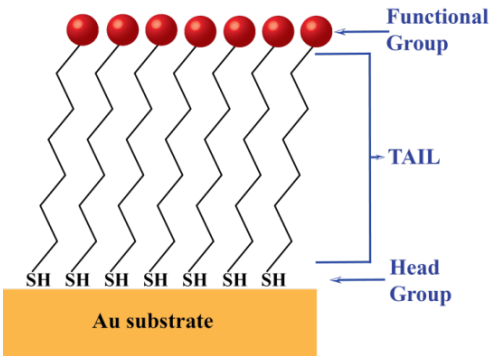

Figure 1.11. Illustration of thiol-based SAMs on a gold substrate.

For the preparation of thin-films of MOFs the by layer-by-layer liquid epitaxy method, surface functionalization with SAMs acts as a key role in directing the nucleation, orientation and the structure of the grown MOFs.[35,54–56] The synthesis starts with the modification of the gold surface with an appropriate SAM. SAMs have terminal (functional) groups, which are able to bind to the metal nodes in order to initiate the deposition. As functional groups, mostly COOH, OH, or pyridine terminated SAMs have been used. After the choice of SAMs with desired functional groups, the gold substrate is placed into a solution containing a diluted concentration of SAMs and the substrate is let to stay till the self-assembly is completed as shown in Figure 1.12.

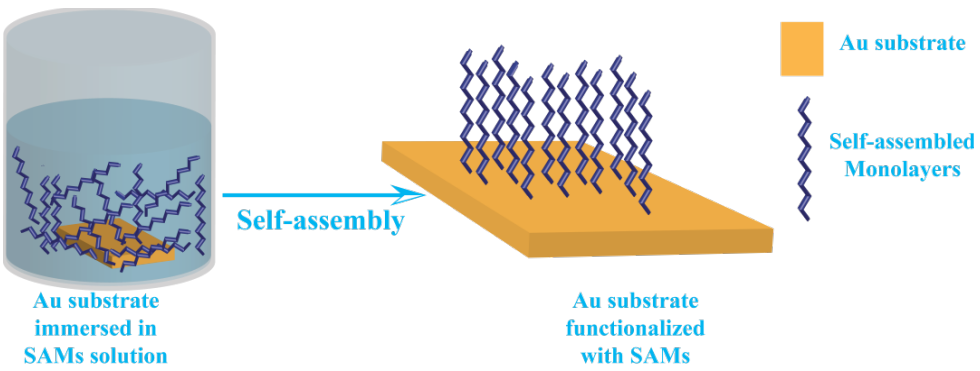

Figure 1.12. Illustration of the modification process of substrate with desired thiol-based SAMs.

The deposition process after the modification of SAMs involves four subsequent steps. The metal precursor solution and the organic linker solution are kept in

separate containers and the substrate is immersed in each of them after following intermediate washing steps. Adsorption of the components take place during immersion steps and washing off unreacted reactants (also excess adsorbed components) is provided by intermediate washing steps (Figure 1.13). The deposition can be performed either manually or via automated systems.

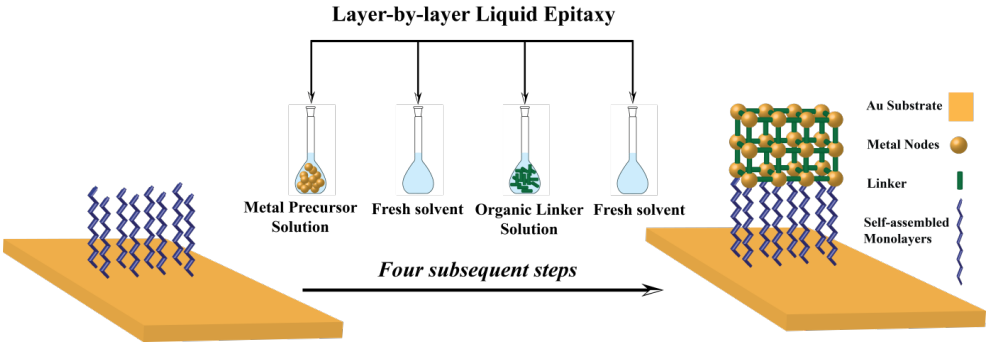

Figure 1.13. Illustration of the general deposition process in layer-by-layer liquid epitaxy method.

Thin-films grown by this method are crystalline and highly oriented. The final orientation of the thin-films are usually governed by the terminal groups of SAMs used.[63]

1.3.2.2. Langmuir-Blodgett Layer-by-Layer Deposition

Langmuir–Blodgett method appears as an outstanding approach for the preparation of well-ordered monolayers on liquid surfaces. These well-ordered monolayers further can be deposited and stacked onto solid substrates.[137] The Langmuir–Blodgett method has so far been employed to a wide variety of molecular systems and the assembly of well-organized 2D arrays were successfully prepared by this method.[201–203] As highlighted in the previous section, layer-by-layer growth technique involves the deposition of components in a sequential manner whereby unreacted or physisorbed components are washed off through intermediate washing steps with an appropriate solvent.

In 2010, coupling of the Langmuir-Blodgett technique with the layer-by-layer method for the fabrication of a MOF was first demonstrated by Makiura et al.[137] The developed method has the main principle of preparation of MOF layers in a Langmuir-Blodgett apparatus and the transfer of these layers in a sequential manner onto a substrate with intermediate washing steps. The layers pile up by weak interactions, such as π stacking between pendant groups. A NAFS-1 film

was successfully prepared by this method as illustrated in Figure 1.14. NAFS-1 is constructed from cobalt-containing porphyrine units (CoTCCP) and binuclear copper paddle-wheel units. The as-prepared 2D CoTCPP-py-Cu layers were deposited onto a substrate (Si(100) or quartz and horizontal dipping of the substrate at room temperature) and the stacking of the layers were achieved by applying layer-by-layer method. The substrate then immersed into a pure solvent between each step and then dried. The individual sheets obtained are remarkably ordered and this was explained by the π–π interaction, which has an essential stereo-electronic role leading to the perfect directional control in the growth of NAFS-1.[137]

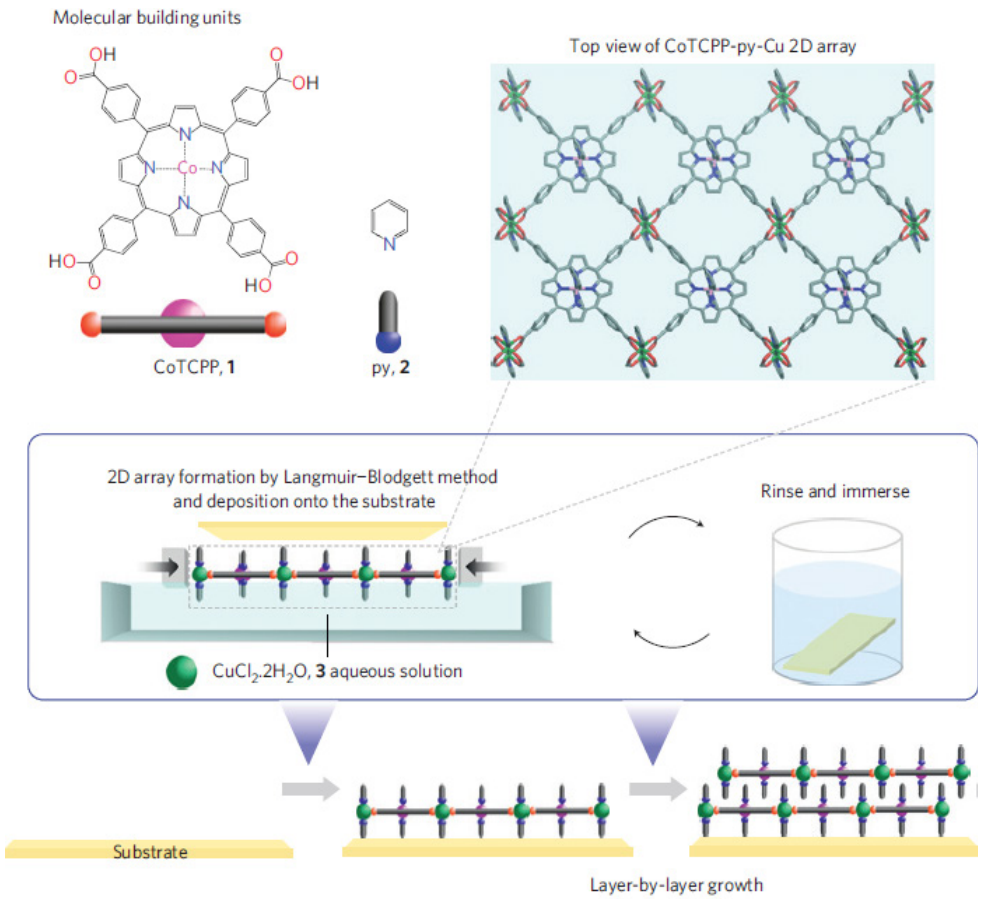

Figure 1.14. Illustration of the Langmuir-Blodgett layer-by-layer deposition method for the fabrication of NAFS-1. The solution mixture of CoTCPP (1) and pyridine (2) molecular building units is spread onto an aqueous solution of $CuCl_2{\cdot}2H_2O$ (3) in a Langmuir trough. This figure has been taken from literature.[137]

1.3.3. Synthesis of MOF Films: Comparison of Different Approaches

The methods available for the preparation of MOF films have been reviewed in the previous sections and it was concluded that none of these synthesis routes can be generalized for all different types of MOFs. The deposition methods should be chosen and altered depending on the desired properties of the MOF films. Among these methods, layer-by-layer liquid epitaxy and Langmuir-Blodgett are preferred since they lead to the formation of highly oriented crystalline films of MOFs. They also offer the potential for building heteroepitaxial structures. Last but not least, thickness and the surface roughness can also be controlled, which make them superior to the other preparation methods described. However, the choice of MOFs to be fabricated as films appear as limitations to these methods. In the case of LbL liquid epitaxy, the use of thiol-based SAMs (on gold substrates) and for the Langmuir-Blodgett technique the water/ambient air interface are restricting the general applicability of these methods.

1.4. Scope of This PhD Thesis

Metal-Organic Frameworks have emerged as promising hybrid, crystalline and porous materials. Bulk synthesis of MOFs plays an important role in order to understand the parameters affecting the structure and topology. For this reason, there has been many different preparation methods proposed. As our knowledge about bulk synthesis of MOFs increases, a growing interest has been directed towards the growth of MOF thin-films onto a suitable substrate (also known as SURMOFs) preferably in an oriented fashion by the use of self-assembled monolayers (SAMs). However, the synthesis and characterization of these MOF thin-films are still a challenge and new insights into the growth mechanisms and heterogeneities present in the films would be certainly helpful to further advance this field of research. This is the topic of this PhD thesis.

In Chapter 2, a phase-pure controlled synthesis of Co-ZIF-9 by pH adjustment method is presented. It was found that the reported Co-ZIF-9 synthesis procedure by Park et al. yielded in the formation of a secondary phase, namely cobalt formate. The reason for the formation of this secondary phase was addressed and related to the coordination flexibility and environment of Co^{2+} ions. A mechanism for the formation of second phase was proposed and a detailed characterization study was performed.

In Chapter 3, the preparation and detailed characterization of surface-mounted thin-films of ZIF-8 (SURZIF-8) will be discussed. A layer-by-layer liquid epitaxy method was used for the preparation of SURZIF-8 thin-films with 20 and 50 cycles

and the materials have been characterized with Raman spectroscopy and Atomic Force Microscopy (AFM). A detailed analysis of the mapping data with principal component analysis (PCA) revealed the existence of phase boundaries within the 20 cycle thin-film, while the 50-cycle thin-film is more chemical homogeneous. Density Functional Theory (DFT) calculations enabled us to provide spectroscopic fingerprints of the molecular vibrations associated with Zn-ZIF-8 thin-film materials. In this Chapter we will show the identification of several spectroscopic markers, indicative for the presence of defects sites (i.e., the free linker as well as a linker coordinated to only one Zn^{2+} ion) and it was found that the relative intensities of the ~ 1135, 1180 and 1498 cm^{-1} Raman bands, are diagnostic for the presence of structural defects and can be used for spectral zoning and Raman mapping.

In Chapter 4 we present a combined AFM-vibrational spectroscopy research strategy for the investigation of the chemistries governing the nucleation and growth of Zn-ZIF-8 and Co-ZIF-67 thin-films prepared through direct synthesis method. A single step direct synthesis approach is used to interrogate the influence of different synthesis parameters, namely, metal/linker ratio, temperature and metal type on the thin-film nucleation and growth behavior. While the metal/linker ratio has a pronounced effect on the thin-film nucleation rate, the temperature mainly influences the growth kinetics of nuclei forming the thin-film. In addition, the nucleation and growth of ZIF thin-films is shown to be highly dependent on the electronegativity of the metal type. Co^{2+} as the constituent metal in Co-ZIF-67 exhibits more reactive nucleation and growth behaviour compared to Zn^{2+} in the isostructural Zn-ZIF-8 material. Finally, the thin-film thickness control can be achieved by using a multistep synthesis strategy, implying repetitive application of single step deposition under identical synthesis conditions, for which a growth mechanism is proposed.

Chapter 5 summarizes the main conclusions from the previous Chapters with an outlook for possible future studies.

1.5. References

[1] M. E. Davis, *Nature* **2002**, *417*, 813–821.

[2] B. M. Weckhuysen, J. Yu, *Chem. Soc. Rev.* **2015**, *44*, 7022–7024.

[3] J. Weitkamp, *Solid State Ionics* **2000**, *131*, 175–188.

[4] M. E. Davis, R. F. Lobo, *Chem. Mater.* **1992**, *4*, 756–768.

[5] R. M. Barrer, *Hydrothermal Chemistry of Zeolites*, Academic Press, London, **1982**.

[6] D. W. Breck, *Zeolite Molecular Sieves*, Wiley, New York, **1974**.

[7] R. Szostak, *Molecular Siesves - Principles of Synthesis and Identification*, Van Nostrand Reinhold, New York, **1988**.

[8] A. W. Chester, E. G. Derouane, *Zeolite Characterization and Catalysis: A Tutorial*, Springer, Dordrecht, **2009**.

[9] "International Zeolite Association," can be found under http://www.iza-structure.org/databases/, **n.d.**

[10] S. T. Wilson, B. M. Lok, C. A. Messina, T. R. Cannan, E. M. Flanigen, *J. Am. Chem. Soc.* **1982**, *104*, 1146–1147.

[11] R. S. Hedge, S. R. Grossman, L. A. Liamins, P. B. Sigler, *Nature* **1992**, *356*, 133–135.

[12] D. Zhao, J. Feng, Q. Huo, N. Melosh, G. H. Fredrickson, B. F. Chmelka, G. D. Stucky, *Science (80-.).* **1998**, *279*, 548–52.

[13] H. Li, M. Eddaoudi, M. O'Keeffe, O. M. Yaghi, *Nature* **1999**, *402*, 276–279.

[14] D. Farruseng, Ed. , *Metal-Organic Frameworks: Applications from Catalysis to Gas Storage*, Wiley, New York, **2011**.

[15] "The Cambridge Crystallographic Data Centre (CCDC)," can be found under http://www.ccdc.cam.ac.uk/, **n.d.**

[16] J. A. Botas, G. Calleja, M. Sánchez-Sánchez, M. G. Orcajo, *Langmuir* **2010**, *26*, 5300–5303.

[17] G. Kumari, K. Jayaramulu, T. K. Maji, C. Narayana, *J. Phys. Chem. A* **2013**, *117*, 11006–11012.

[18] S. Couck, E. Gobechiya, C. E. A. Kirschhock, P. Serra-Crespo, J. Juan-Alcañiz, A. Martinez Joaristi, E. Stavitski, J. Gascon, F. Kapteijn, G. V Baron, *ChemSusChem* **2012**, *5*, 740–750.

[19] L. Zhang, Y. Jian, J. Wang, C. He, X. Li, T. Liu, C. Duan, *Dalt. Trans.* **2012**, *41*, 10153–10155.

[20] L. He, Y. Liu, J. Liu, Y. Xiong, J. Zheng, Y. Liu, Z. Tang, *Angew. Chem. Int. Ed.* **2013**, *52*, 3741–3745.

[21] K. M. L. Taylor-Pashow, J. Della Rocca, Z. Xie, S. Tran, W. Lin, *J. Am. Chem. Soc.* **2009**, *131*, 14261–14263.

[22] S. Keskin, K. Seda, *Ind. Eng. Chem. Res.* **2011**, *50*, 1799–1812.

[23] S. Horike, M. Dincă, K. Tamaki, J. R. Long, *J. Am. Chem. Soc.* **2008**, *130*, 5854–5855.

[24] L. T. L. Nguyen, K. K. A. Le, H. X. Truong, N. T. S. Phan, *Catal. Sci. Technol.* **2012**, *2*, 521–528.

[25] B. R. Pimentel, A. Parulkar, E.-K. Zhou, N. A. Brunelli, R. P. Lively, *ChemSusChem* **2014**, *7*, 3202–3240.

[26] J. A. J. Jarvis, A. F. Wells, *Acta Crystallogr.* **1960**, *13*, 1027–1028.

[27] Y.-Q. Tian, C.-X. Cai, Y. Ji, X.-Z. You, S.-M. Peng, G.-H. Lee, *Angew. Chem. Int. Ed.* **2002**, *41*, 1384–1386.

[28] K. S. Park, Z. Ni, A. P. Côté, J. Y. Choi, R. Huang, F. J. Uribe-Romo, H. K. Chae, M. O'Keeffe, O. M. Yaghi, *Proc. Natl. Acad. Sci. U. S. A.* **2006**, *103*, 10186–10191.

[29] A. P. Cote, A. I. Benin, N. W. Ockwig, M. O. Keeffe, A. J. Matzger, O. M. Yaghi, *Science* **2005**, *310*, 1166–1171.

[30] J. Yao, H. Wang, *Chem. Soc. Rev.* **2014**, *43*, 4470–4493.

[31] S. R. Venna, M. A. Carreon, *J. Am. Chem. Soc.* **2010**, *132*, 76–78.

[32] A. Phan, C. J. Doonan, F. J. Uribe-Romo, C. B. Knobler, M. O'Keeffe, O. M. Yaghi, *Acc. Chem. Res.* **2010**, *43*, 58–67.

[33] J. Kahr, J. P. S. Mowat, A. M. Z. Slawin, R. E. Morris, D. Fairen-Jimenez, P. A. Wright, *Chem. Commun.* **2012**, *48*, 6690–6692.

[34] J. Zakzeski, A. Dębczak, P. C. A. Bruijnincx, B. M. Weckhuysen, *Appl. Catal. A Gen.* **2011**, *394*, 79–85.

[35] O. Shekhah, J. Liu, R. A. Fischer, C. Wöll, *Chem. Soc. Rev.* **2011**, *40*, 1081–1106.

[36] A. B?tard, R. A. Fischer, *Chem. Rev.* **2012**, *112*, 1055–1083.

[37] Y. Yoo, Z. Lai, H.-K. Jeong, *Microporous Mesoporous Mater.* **2009**, *123*, 100–106.

[38] V. V. Guerrero, Y. Yoo, M. C. McCarthy, H.-K. Jeong, *J. Mater. Chem.* **2010**, *20*, 3938–3943.

[39] E. Biemmi, A. Darga, N. Stock, T. Bein, *Microporous Mesoporous Mater.* **2008**, *114*, 380–386.

[40] R. Ameloot, L. Stappers, J. Fransaer, L. Alaerts, B. F. Sels, D. E. De Vos, *Chem. Mater.* **2009**, *21*, 2580–2582.

[41] S. Aguado, J. Canivet, D. Farrusseng, *Chem. Commun.* **2010**, *46*, 7999–8001.

[42] E. V. Ramos-Fernandez, M. Garcia-Domingos, J. Juan-Alcañiz, J. Gascon, F. Kapteijn, *Appl. Catal. A Gen.* **2011**, *391*, 261–267.

[43] S. L. James, *Chem. Soc. Rev.* **2003**, *32*, 276–288.

[44] O. K. Farha, J. T. Hupp, *Acc. Chem. Res.* **2010**, *43*, 1166–1175.

[45] S. T. Meek, J. A. Greathouse, M. D. Allendorf, *Adv. Mater.* **2011**, *23*, 249–267.

[46] N. Stock, S. Biswas, *Chem. Rev.* **2012**, *112*, 933–969.

[47] G. Férey, *Chem. Soc. Rev.* **2008**, *37*, 191–214.

[48] N. Stock, *Microporous Mesoporous Mater.* **2010**, *129*, 287–295.

[49] A. Rabenau, *Angew. Chem.* **1985**, *24*, 1026–1040.

[50] J. Klinowski, F. A. Almeida Paz, P. Silva, J. Rocha, *Dalt. Trans.* **2011**, *40*, 321–330.

[51] A. Pichon, A. Lazuen-Garay, S. L. James, *CrystEngComm* **2006**, *8*, 211–214.

[52] L.-G. Qiu, Z.-Q. Li, Y. Wu, W. Wang, T. Xu, X. Jiang, *Chem. Commun.* **2008**, 3642–3644.

[53] D. Zacher, O. Shekhah, C. Wöll, R. A. Fischer, *Chem. Soc. Rev.* **2009**, *38*, 1418.

[54] D. Käfer, G. Witte, P. Cyganik, A. Terfort, C. Wöll, *J. Am. Chem. Soc.* **2006**, *128*, 1723–1732.

[55] J. Su, M. Mrksich, *Langmuir* **2003**, *19*, 4867–4870.

[56] M. Kind, C. Wöll, *Prog. Surf. Sci.* **2009**, *84*, 230–278.

[57] D. Zacher, A. Baunemann, S. Hermes, R. A. Fischer, *J. Mater. Chem.* **2007**, *17*, 2785–2792.

[58] J. Gascon, S. Aguado, F. Kapteijn, *Microporous Mesoporous Mater.* **2008**, *113*, 132–138.

[59] E. Biemmi, C. Scherb, T. Bein, *J. Am. Chem. Soc.* **2007**, *129*, 8054–8055.

[60] H. Guo, G. Zhu, I. J. Hewitt, S. Qiu, *J. Am. Chem. Soc.* **2009**, *131*, 1646–1647.

[61] R. Ameloot, L. Pandey, M. Van der Auweraer, L. Alaerts, B. F. Sels, D. E. De Vos, *Chem. Commun.* **2010**, *46*, 3735–3737.

[62] O. Shekhah, H. Wang, S. Kowarik, F. Schreiber, M. Paulus, C. Sternemann, F. Evers, D. Zacher, R. A. Fischer, C. Wöll, *J. Am. Chem. Soc.* **2007**, *129*, 15118–15119.

[63] O. Shekhah, H. Wang, D. Zacher, R. A. Fischer, C. Wöll, *Angew. Chem. Int. Ed.* **2009**, *48*, 5038–5041.

[64] O. Zybaylo, O. Shekhah, H. Wang, M. Tafipolsky, R. Schmid, D. Johannsmann, C. Wöll, *Phys.*

Chem. Chem. Phys. **2010**, *12*, 8092–8097.

[65] M. D. Allendorf, R. J. T. Houk, L. Andruszkiewicz, A. A. Talin, J. Pikarsky, A. Choudhury, K. A. Gall, P. J. Hesketh, *J. Am. Chem. Soc.* **2008**, *130*, 14404–14405.

[66] L. E. Kreno, J. T. Hupp, R. P. Van Duyne, *Anal. Chem.* **2010**, *82*, 8042–8046.

[67] A. Schoedel, C. Scherb, T. Bein, *Angew. Chem.* **2010**, *49*, 7225–7228.

[68] P. Küsgens, S. Siegle, S. Kaskel, *Adv. Eng. Mater.* **2009**, *11*, 93–95.

[69] R. Ameloot, E. Gobechiya, H. Uji-i, J. A. Martens, J. Hofkens, L. Alaerts, B. F. Sels, D. E. De Vos, *Adv. Mater.* **2010**, *22*, 2685–2688.

[70] C. Carbonell, I. Imaz, D. Maspoch, *J. Am. Chem. Soc.* **2011**, *133*, 2144–2147.

[71] S. Kayaert, S. Bajpe, K. Masschaele, E. Breynaert, C. E. A. Kirschhock, J. A. Martens, *Thin Solid Films* **2011**, *519*, 5437–5440.

[72] J. Liu, F. Sun, F. Zhang, Z. Wang, R. Zhang, C. Wang, S. Qiu, *J. Mater. Chem.* **2011**, *21*, 3775–3778.

[73] M. Meilikhov, K. Yusenko, E. Schollmeyer, C. Mayer, H.-J. Buschmann, R. A. Fischer, *Dalt. Trans.* **2011**, *40*, 4838.

[74] J. Nan, X. Dong, W. Wang, W. Jin, N. Xu, *Langmuir* **2011**, *27*, 4309–4312.

[75] L. D. O'Neill, H. Zhang, D. Bradshaw, *J. Mater. Chem.* **2010**, *20*, 5720–5726.

[76] M. G. Schwab, I. Senkovska, M. Rose, M. Koch, J. Pahnke, G. Jonschker, S. Kaskel, *Adv. Eng. Mater.* **2008**, *10*, 1151–1155.

[77] J. L. Zhuang, D. Ceglarek, S. Pethuraj, A. Terfort, *Adv. Funct. Mater.* **2011**, *21*, 1442–1447.

[78] S. Bundschuh, O. Kraft, H. K. Arslan, H. Gliemann, P. G. Weidler, C. Wöll, *Appl. Phys. Lett.* **2012**, *101*, 101910–101914.

[79] H. C. Streit, M. Adlung, O. Shekhah, H. K. Arslan, O. Zybaylo, T. Ladnorg, H. Gliemann, M. Franzreb, C. Wöll, C. Wickleder, *ChemPhysChem* **2012**, *13*, 2699–2702.

[80] A. Ranft, S. B. Betzler, F. Haase, B. V Lotsch, *CrystEngComm* **2013**, *15*, 9296–9300.

[81] E. Redel, Z. Wang, S. Walheim, J. Liu, H. Gliemann, C. Wöll, *Appl. Phys. Lett.* **2013**, *103*, 91903-9190X.

[82] H. Yamagiwa, S. Sato, T. Fukawa, T. Ikehara, R. Maeda, T. Mihara, M. Kimura, *Sci. Rep.* **2015**, *4*, 6247.

[83] I. Hod, W. Bury, D. M. Karlin, P. Deria, B. Klahr, D. Jin, Y.-W. Chung, T. W. Odom, O. K. Farha, J. T. Hupp, *Adv. Mater.* **2014**, *26*, 6295–6300.

[84] D. Y. Lee, D. V Shinde, S. J. Yoon, K. N. Cho, W. Lee, N. K. Shrestha, S. Han, *J. Phys. Chem. C* **2013**, *118*, 16328–16334.

[85] P. Davydovskaya, A. Ranft, B. V Lotsch, R. Pohle, *Anal. Chem.* **2014**, *86*, 6948–6958.

[86] C. Lu, T. Ben, S. Xu, S. Qiu, *Angew. Chem. Int. Ed.* **2014**, *53*, 6454–6458.

[87] Y. Mao, J. Li, W. Cao, Y. Ying, L. Sun, X. Peng, *ACS Appl. Mater. Interfaces* **2014**, *6*, 4473–4479.

[88] A. A. Talin, A. Centrone, A. C. Ford, M. E. Foster, R. A. Kinney, V. Szalai, F. El Gabaly, H. P. Yoon, F. Léonard, M. D. Allendorf, *Science* **2014**, *343*, 66–69.

[89] Z.-G. Gu, Z. Chen, W.-Q. Fu, F. Wang, J. Zhang, *ACS Appl. Mater. Interfaces* **2015**, *7*, 28585–28590.

[90] L. Pan, Z. Ji, X. Yi, X. Zhu, X. Chen, J. Shang, G. Liu, R.-W. Li, *Adv. Funct. Mater.* **2015**, *25*, 2677–2685.

[91] J. Liu, E. Redel, S. Walheim, Z. Wang, A. Welle, M. Moosmann, T. Scherer, M. Bruns, H. Gliemann, C. Wöll, *Chem. Mater.* **2015**, *27*, 1991–1996.

[92] J. Zhao, B. Gong, W. T. Nunn, P. C. Lemaire, C. J. Oldham, H. J. Walls, S. D. Shepherd, G. W.

Peterson, M. D. Losego, G. N. Parsons, *J. Mater. Chem. A* **2015**, *3*, 1458–1464.

[93] L. Heinke, M. Tu, S. Wannapaiboon, R. A. Fischer, C. Wöll, *Microporous Mesoporous Mater.* **2015**, *216*, 200–215.

[94] W. Qin, M. E. Silvestre, F. Kirschhöfer, G. Brenner-Weiss, M. Franzreb, *J. Chromatogr. A* **2015**, *1411*, 77–83.

[95] X. Xu, *Nanoscale* **2016**, *8*, 16725–16732.

[96] W. Guo, M. Zha, Z. Wang, E. Redel, Z. Xu, C. Wöll, *ACS Appl. Mater. Interfaces* **2016**, *8*, 24699–24702.

[97] V. Chernikova, O. Shekhah, M. Eddaoudi, *ACS Appl. Mater. Interfaces* **2016**, *8*, 20459–20464.

[98] L. Wang, Y. Wu, R. Cao, L. Ren, M. Chen, X. Feng, J. Zhou, B. Wang, *ACS Appl. Mater. Interfaces* **2016**, *8*, 16736–16743.

[99] G. Xu, T. Yamada, K. Otsubo, S. Sakaida, H. Kitagawa, *J. Am. Chem. Soc.* **2012**, *134*, 16524–16527.

[100] R. Elzein, C.-M. Chang, I. Ponomareva, W.-Y. Gao, S. Ma, R. Schlaf, *ACS Appl. Mater. Interfaces* **2016**, *8*, 31403–31412.

[101] Z. Wang, H. Sezen, J. Liu, K. Peikert, M. Fröba, A. Mavrandonakis, B. Supronowicz, T. Heine, H. Gliemann, C. Wöll, *Microporous Mesoporous Mater.* **2015**, *207*, 53–60.

[102] S. Rana, R. Rajendra, B. Dhara, P. K. Jha, N. Ballav, *Adv. Mater. Interfaces* **2016**, *3*, 1500738.

[103] S. Hermes, F. Schröder, R. Chelmowski, C. Wöll, R. A. Fischer, *J. Am. Chem. Soc.* **2005**, *127*, 13744–13745.

[104] S. Hermes, D. Zacher, A. Baunemann, C. Wöll, R. A. Fischer, *Chem. Mater.* **2007**, *19*, 2168–2173.

[105] Y. Yoo, H.-K. Jeong, *Chem. Commun.* **2008**, 2441–2443.

[106] Y. Liu, Z. Ng, E. A. Khan, H.-K. Jeong, C. Ching, Z. Lai, *Microporous Mesoporous Mater.* **2009**, *118*, 296–301.

[107] P. Falcaro, A. J. Hill, K. M. Nairn, J. Jasieniak, A. Patelli, B. Marmiroli, H. Amenitsch, T. Colson, L. Villanova, D. Buso, *Nat. Commun.* **2011**, *2*, 237.

[108] D. Yan, G. O. Lloyd, A. Delori, W. Jones, X. Duan, *Chempluschem* **2012**, *77*, 1112–1118.

[109] S. Wannapaiboon, M. Tu, R. A. Fischer, *Adv. Funct. Mater.* **2014**, *24*, 2696–2705.

[110] H. Lan, D. Pan, Y. Sun, Y. Guo, Z. Wu, *Anal. Chim. Acta* **2016**, *937*, 53–60.

[111] Z. Wang, J. Liu, H. K. Arslan, S. Grosjean, T. Hagendorn, H. Gliemann, S. Bra, *Langmuir* **2013**, *29*, 15958–15964.

[112] G. Lu, J. T. Hupp, *J. Am. Chem. Soc.* **2010**, *132*, 7832–7833.

[113] A. Demessence, C. Boissière, D. Grosso, P. Horcajada, C. Serre, G. Férey, G. J. A. A. Soler-Illia, C. Sanchez, *J. Mater. Chem.* **2010**, *20*, 7676–7681.

[114] H. Bux, F. Liang, Y. Li, J. Cravillon, M. Wiebcke, *J. Am. Chem. Soc.* **2009**, *131*, 16000–16001.

[115] H. Bux, C. Chmelik, R. Krishna, J. Caro, *J. Memb. Sci.* **2011**, *369*, 284–289.

[116] H. Bux, A. Feldhoff, J. Cravillon, M. Wiebcke, Y.-S. Li, J. Caro, *Chem. Mater.* **2011**, *23*, 2262–2269.

[117] S. R. Venna, M. A. Carreon, *J. Am. Chem. Soc.* **2010**, *132*, 76–78.

[118] M. C. McCarthy, V. Varela-Guerrero, G. V Barnett, H.-K. Jeong, *Langmuir* **2010**, *26*, 14636–14641.

[119] J. Yao, D. Dong, D. Li, L. He, G. Xu, H. Wang, *Chem. Commun.* **2011**, *47*, 2559–2561.

[120] I. Stassen, N. Campagnol, J. Fransaer, P. Vereecken, D. De Vos, R. Ameloot, *CrystEngComm* **2013**, *15*, 9308–9311.

[121] K. Khaletskaya, S. Turner, M. Tu, S. Wannapaiboon, A. Schneemann, R. Meyer, A. Ludwig, G. Van Tendeloo, R. A. Fischer, *Adv. Funct. Mater.* **2014**, *24*, 4804–4811.

[122] L. Kong, X. Zhang, H. Liu, T. Wang, J. Qiu, *J. Phys. Chem. Solids* **2015**, *77*, 23–29.

[123] Y. Guo, X. Wang, P. Hu, X. Peng, *Appl. Mater. Today* **2016**, *5*, 103–110.

[124] E. P. Valadez Sánchez, H. Gliemann, K. Haas-Santo, C. Wöll, R. Dittmeyer, *Chemie Ing. Tech.* **2016**, *88*, 1798–1805.

[125] L. Li, X. Jiao, D. Chen, C. Li, *Cryst. Growth Des.* **2016**, *16*, 2700–2707.

[126] B. M. Weckhuysen, M. Filez, Z. Ozturk, *Chem. Eur. J.* **2017**, *23*, 10915-10924.

[127] W. Li, X. Jin, F. Huang, G. Z. Chen, *Angew. Chem. Int. Ed.* **2010**, *49*, 3203–3206.

[128] Y. S. Li, H. Bux, A. Feldhoff, G. N. Li, W. S. Yang, J. Caro, *Adv. Mater.* **2010**, *22*, 3322–3326.

[129] Y. Li, F. Liang, H. Bux, W. Yang, J. Caro, *J. Memb. Sci.* **2010**, *354*, 48–54.

[130] C. Dimitrakakis, C. D. Easton, B. W. Muir, B. P. Ladewig, M. R. Hill, *Cryst. Growth Des.* **2013**, *13*, 4411–4417.

[131] A. Huang, H. Bux, F. Steinbach, J. Caro, *Angew. Chem. Int. Ed.* **2010**, *49*, 4958–4961.

[132] Y. Liu, E. Hu, E. A. Khan, Z. Lai, *J. Memb. Sci.* **2010**, *353*, 36–40.

[133] A. Huang, W. Dou, J. Caro, *J. Am. Chem. Soc.* **2010**, *132*, 15562–15564.

[134] A. Huang, J. Caro, *Angew. Chem. Int. Ed.* **2011**, *50*, 4979–4982.

[135] M. Kubo, W. Chaikittisilp, T. Okubo, *Chem. Mater.* **2008**, *20*, 2887–2889.

[136] S. Aguado, C.-H. Nicolas, V. Moizan-Baslé, C. Nieto, H. Amrouche, N. Bats, N. Audebrand, D. Farrusseng, *New J. Chem.* **2011**, *35*, 41–44.

[137] R. Makiura, S. Motoyama, Y. Umemura, H. Yamanaka, O. Sakata, H. Kitagawa, *Nat. Mater.* **2010**, *9*, 565–571.

[138] M. Soichiro, R. Makiura, O. Sakata, H. Kitagawa, *J. Am. Chem. Soc.* **2011**, *133*, 5640–5643.

[139] O. Shekhah, H. Wang, M. Paradinas, C. Ocal, B. Schüpbach, A. Terfort, D. Zacher, R. A. Fischer, C. Wöll, *Nat. Mater.* **2009**, *8*, 481–484.

[140] K. Yusenko, M. Meilikhov, D. Zacher, F. Wieland, C. Sternemann, X. Stammer, T. Ladnorg, C. Wöll, R. A. Fischer, *CrystEngComm* **2010**, *12*, 2086–2090.

[141] A. Bétard, H. Bux, S. Henke, D. Zacher, J. Caro, R. A. Fischer, *Microporous Mesoporous Mater.* **2012**, *150*, 76–82.

[142] D. Zacher, K. Yusenko, A. Bétard, O. Shekhah, T. de los Arcos, M. Krasnopolski, J. Winter, A. Terfort, C. Wöll, R. A. Fischer, *Chem. Eur. J.* **2011**, *17*, 1448–1455.

[143] O. Shekhah, K. Hirai, H. Uehara, S. Diring, D. Zacher, R. A. Fischer, O. Sakata, S. Kitagawa, S. Furukawa, C. Wöll, *Dalt. Trans.* **2011**, *40*, 4954–4958.

[144] B. Liu, M. Ma, D. Zacher, A. Bétard, K. Yusenko, N. Metzler-Nolte, C. Wöll, R. A. Fischer, *J. Am. Chem. Soc.* **2011**, *133*, 1734–1737.

[145] A. Bétard, D. Zacher, R. A. Fischer, *CrystEngComm* **2010**, *12*, 3768–3772.

[146] A. Centrone, Y. Yang, S. Speakman, L. Bromberg, G. C. Rutledge, T. A. Hatton, *J. Am. Chem. Soc.* **2010**, *132*, 15687–15691.

[147] Y. Yoo, H. K. Jeong, *Cryst. Growth Des.* **2010**, *10*, 1283–1288.

[148] Y. Yoo, V. Varela-Guerrero, H. K. Jeong, *Langmuir* **2011**, *27*, 2652–2657.

[149] M. Arnold, P. Kortunov, D. J. Jones, Y. Nedellec, J. Karger, J. Caro, *Eur. J. Inorg. Chem.* **2007**, 60–64.

[150] Y. Hu, X. Dong, J. Nan, W. Jin, X. Ren, N. Xu, Y. M. Lee, *Chem. Commun.* **2011**, *47*, 737–739.

[151] A. Gölzhäuser, C. Wöll, *Phys. Chem. Chem. Phys.* **2010**, *12*, 4515–4520.

[152] R. Ranjan, M. Tsapatsis, *Chem. Mater.* **2009**, *21*, 4920–4924.

[153] X. Zou, G. Zhu, F. Zhang, M. Guo, S. Qiu, *CrystEngComm* **2010**, *12*, 352–354.

[154] C. Scherb, R. Koehn, T. Bein, *J. Mater. Chem.* **2010**, *20*, 3046–3051.

[155] C. Scherb, A. Schödel, T. Bein, *Angew. Chem. Int. Ed.* **2008**, *47*, 5777–5779.

[156] Z. Hu, C. Tao, H. Liu, X. Zou, H. Zhu, J. Wang, *J. Mater. Chem. A* **2014**, *2*, 14222–14227.

[157] K. Otsubo, T. Haraguchi, O. Sakata, A. Fujiwara, H. Kitagawa, *J. Am. Chem. Soc.* **2012**, *134*, 9605–9608.

[158] T. Haraguchi, K. Otsubo, O. Sakata, A. Fujiwara, H. Kitagawa, *Inorg. Chem.* **2015**, *54*, 11593–11595.

[159] T. Haraguchi, K. Otsubo, O. Sakata, A. Fujiwara, H. Kitagawa, *J. Am. Chem. Soc.* **2016**, *138*, 16787–16793.

[160] P. Horcajada, C. Serre, D. Grosso, C. Boissière, S. Perruchas, C. Sanchez, G. Férey, *Adv. Mater.* **2009**, *21*, 1931–1935.

[161] A. Demessence, P. Horcajada, C. Serre, C. Boissière, D. Grosso, C. Sanchez, G. Férey, *Chem. Commun.* **2009**, *101*, 7149–7151.

[162] X. Zou, G. Zhu, I. J. Hewitt, F. Sun, S. Qiu, *Dalt. Trans.* **2009**, 3009–3013.

[163] L. V. Meyer, J. Vogt, F. A. Brede, H. Schäfer, M. Steinhart, K. Müller-Buschbaum, *CrystEngComm* **2013**, *15*, 9382–9386.

[164] M. C. So, S. Jin, H. Son, G. P. Wiederrecht, O. K. Farha, J. T. Hupp, *J. Am. Chem. Soc.* **2013**, *135*, 15698–15701.

[165] S. Sorribas, P. Gorgojo, C. Téllez, J. Coronas, A. G. Livingston, *J. Am. Chem. Soc.* **2013**, *135*, 15201–15208.

[166] H. Liu, H. Wang, T. Chu, M. Yu, Y. Yang, *J. Mater. Chem. C* **2014**, *2*, 8683–8690.

[167] Y. Lu, B. Yan, *J. Mater. Chem. C* **2014**, *2*, 7411–7416.

[168] Y. Lu, B. Yan, *J. Mater. Chem. C* **2014**, *2*, 5526–5532.

[169] P.-C. Guo, T.-Y. Chen, X.-M. Ren, Z. Chu, W. Jin, *J. Mater. Chem. A* **2014**, *2*, 13698–13704.

[170] K. B. Lausund, O. Nilsen, *Nat. Commun.* **2016**, *7*, 13578.

[171] J. Zhao, D. T. Lee, R. W. Yaga, M. G. Hall, H. F. Barton, I. R. Woodward, C. J. Oldham, H. J. Walls, G. W. Peterson, G. N. Parsons, *Angew. Chem. Int. Ed.* **2016**, *55*, 13224–13228.

[172] Z. Wang, S. Grosjean, S. Bräse, L. Heinke, *ChemPhysChem* **2015**, *16*, 3779–3783.

[173] X. Yu, Z. Wang, M. Buchholz, N. Füllgrabe, S. Grosjean, F. Bebensee, S. Bräse, C. Wöll, L. Heinke, *Phys. Chem. Chem. Phys.* **2015**, *17*, 22721–22725.

[174] D. Y. Lee, E.-K. Kim, N. K. Shrestha, D. W. Boukhvalov, J. K. Lee, S.-H. Han, *ACS Appl. Mater. Interfaces* **2015**, *7*, 18501–18507.

[175] D. Y. Lee, I. Lim, C. Y. Shin, S. A. Patil, W. Lee, N. K. Shrestha, J. K. Lee, S.-H. Han, *J. Mater. Chem. A* **2015**, *3*, 22669–22676.

[176] Z.-G. Gu, S. Grosjean, S. Bräse, C. Wöll, L. Heinke, *Chem. Commun.* **2015**, *51*, 8998–9001.

[177] X. Shen, B. Yan, *Dalt. Trans.* **2015**, *44*, 1875–1881.

[178] S. Wannapaiboon, M. Tu, K. Sumida, K. Khaletskaya, S. Furukawa, S. Kitagawa, R. A. Fischer, *J. Mater. Chem. A* **2015**, *3*, 23385–23394.

[179] O. Yassine, O. Shekhah, A. H. Assen, Y. Belmabkhout, K. N. Salama, M. Eddaoudi, *Angew. Chem. Int. Ed.* **2016**, *55*, 15879–15883.

[180] O. Shekhah, J. Liu, R. A. Fischer, C. Wöll, *Chem. Soc. Rev.* **2011**, *40*, 1081–106.

[181] O. M. Yaghi, G. Li, H. Li, *Chem. Mater.* **1997**, *4756*, 1074–1076.

[182] M. A. Snyder, M. Tsapatsis, *Angew. Chem. Int. Ed.* **2007**, *46*, 7560–7573.

[183] M. Shah, M. C. McCarthy, S. Sachdeva, A. K. Lee, H.-K. Jeong, *Ind. Eng. Chem. Res.* **2012**, *51*, 2179–2199.

[184] S. Qiu, M. Xue, G. Zhu, *Chem. Soc. Rev.* **2014**, *43*, 6116–6140.

[185] U. Mueller, M. Schubert, F. Teich, H. Puetter, K. Schierle-Arndt, J. Pastré, *J. Mater. Chem.* **2006**, *16*, 626–636.

[186] S. S. Y. Chui, S. M. F. Lo, J. P. H. Charmant, A G. Orpen, I. D. Williams, *Science* **1999**, *283*, 1148–1150.

[187] G. Decher, *Science* **1997**, *277*, 1232–1237.

[188] D. Yoo, S. S. Shiratori, M. F. Rubner, *Macromolecules* **1998**, *31*, 4309–4318.

[189] S. S. Shiratori, M. F. Rubner, *Macromolecules* **2000**, *33*, 4213–4219.

[190] N. Fujii, K. Fujimoto, T. Michinobu, M. Akada, J. P. Hill, S. Shiratori, K. Ariga, K. Shigehara, *Macromolecules* **2010**, *43*, 3947–3955.

[191] Q. He, Y. Cui, J. Li, *Chem. Soc. Rev.* **2009**, *38*, 2292–303.

[192] Y. Lvov, K. Ariga, I. Ichinose, T. Kunitake, *J. Am. Chem. Soc.* **1995**, *117*, 6117–6123.

[193] Q. Ji, I. Honma, S.-M. Paek, M. Akada, J. P. Hill, A. Vinu, K. Ariga, *Angew. Chem. Int. Ed.* **2010**, *49*, 9737–9739.

[194] Q. Ji, S. B. Yoon, J. P. Hill, A. Vinu, J. S. Yu, K. Ariga, *J. Am. Chem. Soc.* **2009**, *131*, 4220–4221.

[195] K. Ariga, A. Vinu, Q. Ji, O. Ohmori, J. P. Hill, S. Acharya, J. Koike, S. Shiratori, *Angew. Chem. Int. Ed.* **2008**, *47*, 7257–7257.

[196] K. Katagiri, R. Hamasaki, K. Ariga, J. Kikuchi, *J. Am. Chem. Soc.* **2002**, *124*, 7892–7893.

[197] Q. He, L. Duan, W. Qi, K. W. Wang, Y. Cui, X. H. Yan, J. B. Li, *Adv. Mater.* **2008**, *20*, 2933–2937.

[198] A. Ulman, *Chem. Rev.* **1996**, *96*, 1533–1554.

[199] J. C. Love, L. A. Estroff, J. K. Kriebel, R. G. Nuzzo, G. M. Whitesides, *Chem. Rev.* **2005**, *105*, 1103–1169.

[200] R. Schreiber, *Prog. Surf. Sci.* **2000**, *65*, 151–256.

[201] K. Tollner, R. Popovitz-Biro, M. Lahav, D. Milstein, *Science* **1997**, *278*, 2100–2102.

[202] D. Y. Takamoto, E. Aydil, J. A. Zasadzinski, A. T. Ivanova, D. K. Schwartz, T. Yang, P. S. Cremer, *Science* **2001**, *293*, 1292–1295.

[203] D. J. Qian, C. Nakamura, J. Miyake, *Langmuir* **2000**, *16*, 9615–9619.

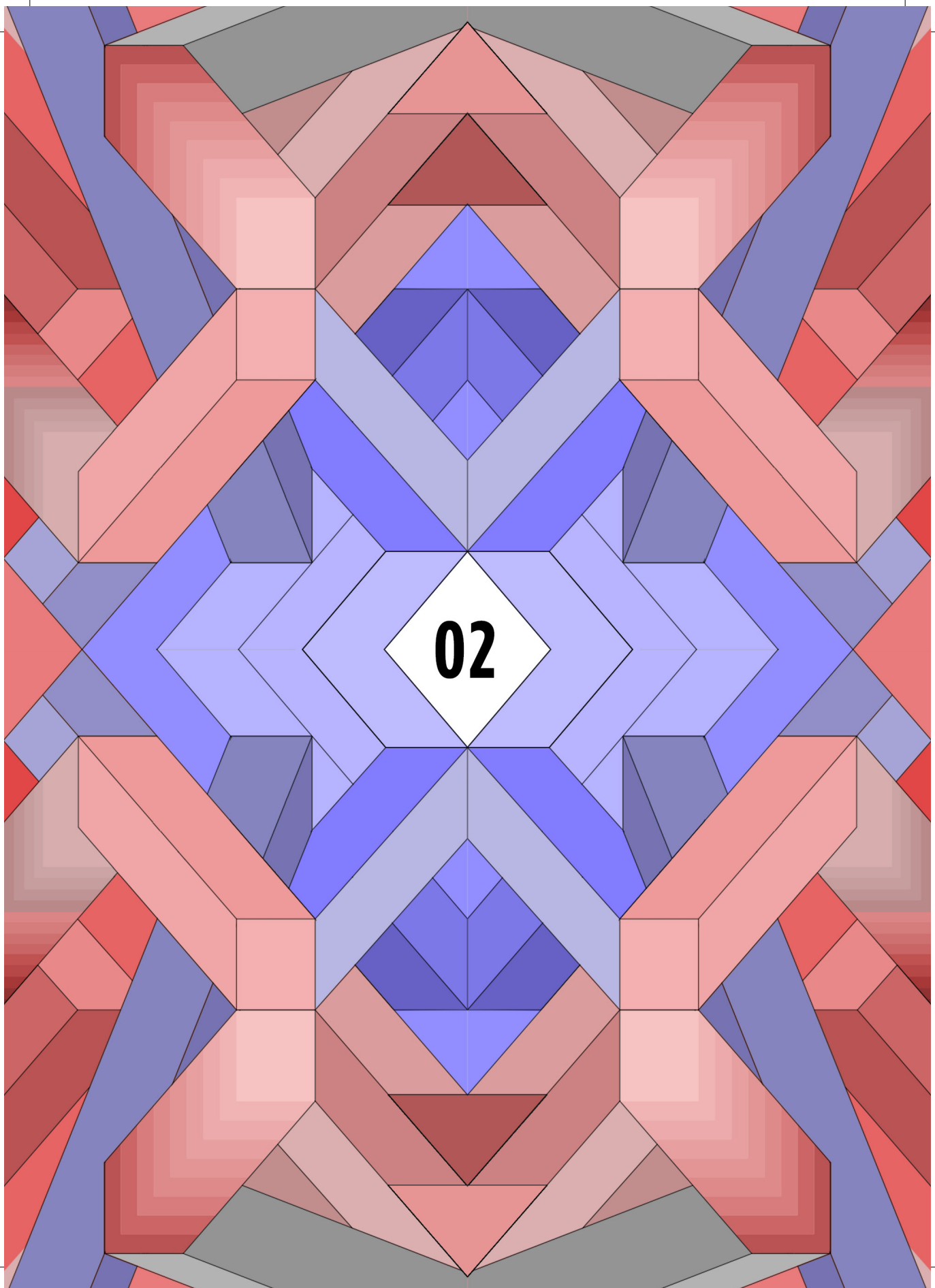
02

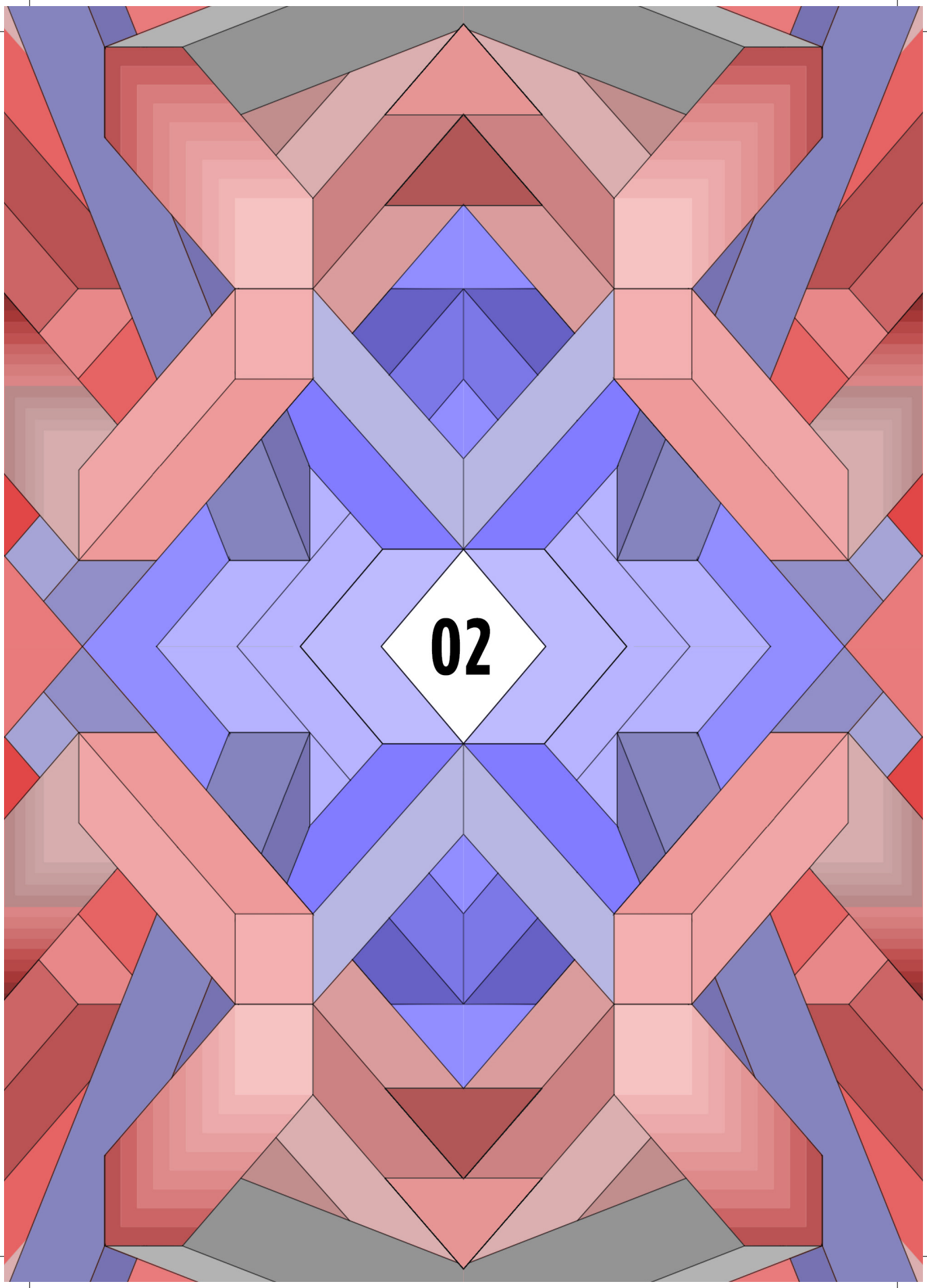
02

02

Controlled Synthesis of Phase-Pure Zeolitic Imidazolate Framework Co-ZIF-9

Abstract

Synthesis of phase-pure metal-organic frameworks with desired properties is crucial for their potential applications. In this Chapter, we show that the synthesis of a phase-pure Co-ZIF-9, an important cobalt-based zeolitic imidazolate framework, could be achieved by modification of the reported synthesis procedure through pH value adjustment of the starting synthesis mixture. The phase-pure Co-ZIF-9 material obtained has been characterized by a combination of UV-Vis, FT-IR and Raman spectroscopy as well as by TGA and XRD, and possesses a lower overall crystallinity. This can be explained by the base addition for the pH adjustment method. Based on these findings, a synthesis pathway for the formation of the secondary phase, cobalt formate, was proposed along with its relationship to the flexibility of the coordination environment of cobalt ions. The crystal structures of both phases have been determined by single crystal X-ray crystallography and the resolved structures also reflected the coordination flexibility of framework cobalt ions.

This Chapter is based on the following publication: Z. Öztürk, J.P. Hofmann, M. Lutz, M. Mazaj, N. Zabukovec Logar, B. M. Weckhuysen, *Eur. J. Inorg. Chem.* **2015**, 9, 1625-1630.

2.1. Introduction

During the last two decades Metal-Organic Frameworks (MOFs) have emerged as an important and promising class of hybrid crystalline porous materials for e.g. gas storage and separation, and catalysis.[1–8] A great deal of attention for these porous materials can be attributed to the intriguing hybrid framework structures, composed of organic and inorganic building blocks. The ability to incorporate and modify the organic linkers within these framework structures renders many possibilities for the design of new crystalline porous structures with specific physicochemical functionalities.[9–11]

Zeolitic Imidazolate Frameworks (ZIFs) are a sub-class of MOF materials and have a similar coordination geometry compared to microporous crystalline aluminosilicates, better known as zeolites.[12,13] ZIFs are composed of transition metal ions tetrahedrally coordinated by bridging imidazolate linkers with a primary unit of $[M(Im)_4]$, where M is the transition metal Co^{2+}, Zn^{2+}, Cu^{2+} or Fe^{2+} and Im represents the imidazolate or a derivative.[14,15] The benzimidazolate-based ZIFs, namely ZIF-7 (sod), ZIF-9 (sod), ZIF-11 (rho) and ZIF-12 (rho), were previously reported by Park et al.[16] Among these ZIF materials, ZIF-7 and ZIF-11 are Zn^{2+}- (Zn-ZIF-7 & Zn-ZIF-11) based, while ZIF-9 and ZIF-12 are Co^{2+}- (Co-ZIF-9 and Co-ZIF-12) based. The differences in the topologies of the as-synthesized materials arise from the use of different solvents, synthesis time, and temperature.[16] The microporous structure and the potential to get unsaturated metal coordination sites make them promising candidates as materials for heterogeneous catalysis.[14]

In this Chapter, we show that the use of the reported cobalt-ZIF-9 (Co-ZIF-9) synthesis procedure by Park et al.[16] yields two different crystalline materials, namely Co-ZIF-9 and an additional, undesired phase, cobalt formate. This observation is also in line with the recent studies on Co-ZIF-9 catalysis as evidenced from the reported X-ray diffraction (XRD) patterns.[14,17–19] In our study, the structures of Co-ZIF-9 and cobalt formate were resolved by making use of single crystal X-ray crystallography. Based on this knowledge, a phase-pure Co-ZIF-9 material could be prepared by a modification of the method reported by Park et al..[16] More specifically, the pH of the synthesis mixture has been adjusted, resulting in a phase-pure Co-ZIF-9. This material has, however, a lower crystallinity, which can be attributed to the base addition required for pH adjustment. Furthermore, a synthesis pathway for the formation of cobalt formate has been proposed and is related to the coordinative flexibility of Co^{2+} ions. A detailed characterization study has been provided making use of a combination of UV-Vis, FT-IR and Raman spectroscopy as well as XRD and thermogravimetric analysis (TGA).

2.2. Experimental

2.2.1. Synthesis of Mixtures of Co-ZIF-9 & Cobalt Formate, & Related Crystal Separation

The synthesis procedure of Co-ZIF-9 has been described by Park et al.[16] In a typical synthesis, 0.210 g of $Co(NO_3)_2 \cdot 6H_2O$ (Sigma-Aldrich, 99%) and 0.060 g of benzimidazole (Sigma-Aldrich, 98%) were mixed in a 20 mL glass vial and dissolved by the addition of 18 mL of N,N-dimethylformamide, DMF (Acros, 98%). After the glass vial was capped, it was placed into a programmable oven and heated up to 130°C at a heating rate of 5°C.min^{-1}. The vial was cooled to room temperature at a rate of 0.4°C.min^{-1}, after being held at 130°C for 48 h. After the separation of the mother liquor, 10 mL of chloroform (Acros, 98 %) was added to the glass vial and blue/purple crystals were collected from the upper layer of the chloroform, while red crystals stayed in the small amount of the mother liquor at the bottom of the vial. In order to collect the red crystals, chloroform was removed from the glass vial and 5 mL of DMF was added and red crystals were easily collected. Both types of crystals were washed with 3 mL of DMF and allowed to dry in air. Then, the following two days, washing with DMF was continued and after two days washing was proceeded with 3 mL of dichloromethane, DCM (Acros, 99%) for 3 days. The crystals were filtered and let to dry at room temperature for two days. In order to check reproducibility, the same procedure was repeated and the reproducibility was confirmed.

2.2.2. Synthesis of Phase-pure Co-ZIF-9 via the pH Adjustment Synthesis Method

The same amounts of starting materials provided in the synthesis of Co-ZIF-9 and cobalt formate mixtures were used for the synthesis of phase-pure Co-ZIF-9. The measured initial pH was ≈ 4-4.5. The pH of the solution was increased to pH ≈ 8 by the addition of an appropriate amount of solid potassium hydroxide (KOH, Merck, 85 %). The solution was transferred into a 20 mL glass vial. The glass vial was capped, put into a programmable oven, and heated up to 130°C with a heating rate of 5°C. min^{-1}. The cooling rate to the room temperature of the oven was set to 0.4°C.min^{-1}, after the reaction at 130°C for 48 h. The purple crystals were separated from the mother liquor, washed three times with 3 mL of DMF (Acros, 98%), and allowed to dry in air for two days. The synthesis was also carried out by using sodium hydroxide (NaOH, Merck, 99 %) for the pH adjustment method and the formation of phase-pure Co-ZIF-9 was also achieved.

2.2.3. Characterization of Co-ZIF-9 & Cobalt formate

The powder X-ray diffraction (XRD) patterns of as-synthesized materials were performed using CoKα radiation on a Bruker AXS D2 Phaser diffractometer. A Pyris TGA thermogravimetrical analyzer from Perkin Elmer with the sample held in a ceramic pan in a continuous flow nitrogen atmosphere (Linde, 99.999 %, 10 $mL.min^{-1}$) was used for thermogravimetrical analysis (TGA). The samples were heated at a constant rate of 10°$C.min^{-1}$. An Olympus BX41M upright research microscope provided with a 10 x 0.3 NA objective lens was used for UV-Vis micro-spectroscopy studies. Illumination of the sample was performed using a 75 W Tungsten lamp. Scanning electron microscopy (SEM) analyses were performed on a FEI XL30SFEG scanning electron microscope operated at 15 kV. Fourier Transform Infrared spectroscopy (FT-IR) measurements were carried out at room temperature on a Bruker Tensor-27 instrument equipped with Pike MIRacle ATR accessory. Raman spectroscopy measurements were performed with a Renishaw InVia micro-spectrometer making use of a 785 nm laser. The spectra were recorded in the region of 100-3200 cm^{-1}.

2.2.4. X-ray Single Crystal Structure Determinations

X-ray reflections were measured on a Bruker Kappa ApexII diffractometer with sealed tube and a Triumph monochromator (λ = 0.71073Å). The intensities were integrated using the SAINT software.[20] Absorption correction was performed with TWINABS.[21] The initial coordinates for Co-ZIF-9 were those reported previously.[16] The structure of cobalt formate was solved with Direct Methods using SHELXS-97.[22] Least-squares refinement was performed with SHELXL-97[22] against F2 of all reflections. Non-hydrogen atoms were refined freely with anisotropic displacement parameters. Hydrogen atoms were introduced in calculated positions (Co-ZIF-9) or were located in difference-Fourier maps (cobalt formate). All hydrogen atoms were refined with a riding model. Structure calculations and checking for higher symmetry were performed with PLATON.[23] Details of the crystal structures are given in Table 2.1.

The single crystal structures determined in this Chapter (Co-ZIF-9 and Co formate) have been submitted as CCDC files 1031565 (Co-ZIF-9) and 1031566 (cobalt formate) and contain the supplementary crystallographic data. These data can be obtained free of charge from The Cambridge Crystallographic Data Centre via www.ccdc.cam.ac.uk/data_request/cif.[24]

Co-ZIF-9: The measured crystal consisted of several crystalline fragments. The orientation matrices of the two major fragments were used for the intensity integration. The crystal structure contains large solvent accessible voids (1874 Å3 /

unit cell) filled with severely disordered DMF solvent molecules. After de-twinning the data based on F2calc, the contribution of the solvent molecules was treated by back-Fourier transformation with the SQUEEZE routine in PLATON.[23] This procedure resulted in 532 electrons / unit cell.

Cobalt formate: The crystal was non-merohedrally twinned with a twofold rotation about hkl=(-1,0,1) as twin operation. Two orientation matrices were used for the intensity integration. The twin fraction refined to BASF=0.5818(6).

2.3. Results and Discussion

Single crystal X-ray crystallography was employed to determine the structures of the as-synthesized Co-ZIF-9 and cobalt formate materials. Our Co-ZIF-9 material corresponds to the structure reported by Park et al.[16] (Figure 2.1a). The as-synthesized Co-ZIF-9 material was a conglomerate of many crystalline particles and the major two components were used for integrating the X-ray intensities.[24] The co-crystallized solvent molecules (dimethylformamide, DMF) were treated as diffuse electron density. The second framework formed along with Co-ZIF-9 ($CoC_{14}H_{10}N_4$) turned out to be cobalt formate ($Co(HCOO)_2 \times DMF$) with the presence of co-crystallized (non-coordinated) DMF molecules.[24] This crystal structure is known from literature[25–27] (Figure 2.1b). The crystal structure details are provided in Table 2.1.

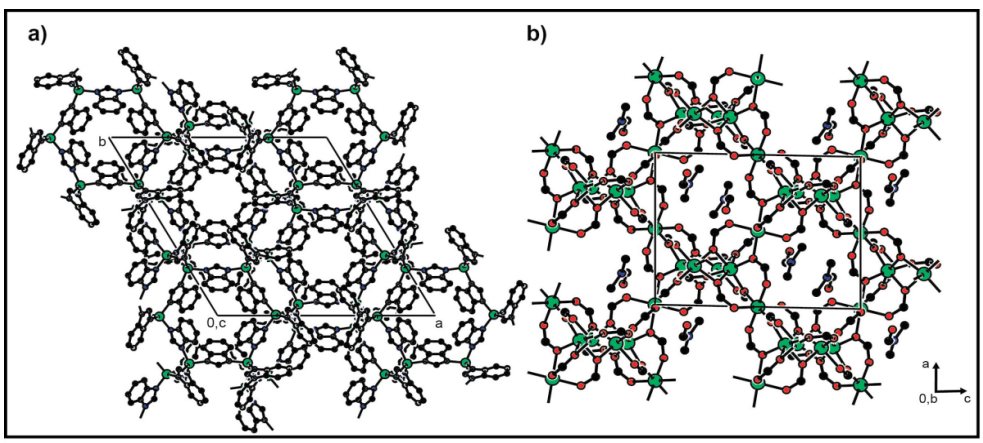

Figure 2.1. Crystal packing structures of **a)** Co-ZIF-9 (Hydrogen atoms and disordered DMF solvent molecules are omitted for clarity) and **b)** cobalt formate (green: cobalt, hydrogen atoms are omitted for clarity).

Tetrahedral and octahedral coordination of Co^{2+} ions were revealed by single crystal

X-ray crystallography for Co-ZIF-9 and cobalt formate, respectively. This finding was also supported by diffuse reflectance UV-Vis spectroscopy measurements. In the diffuse reflectance UV-Vis spectra, the Co-ZIF-9 material gave rise to absorption bands in the regions of 500 and 650 nm with an absorption maximum at 640 nm, which can be assigned to tetrahedral coordination of Co^{2+} ions (Figure 2.2).[28–31] On the other hand, for cobalt formate, the absorption bands appeared in the region of 450 and 550 nm with a distinct shoulder at 450 nm and a maximum at 540 nm, which can be assigned to octahedral coordination of Co^{2+} ions (Figure 2.2).[29–31]

Table 2.1. Crystal and structure refinement data for Co-ZIF-9 and cobalt formate.

	Co-ZIF-9	**Cobalt formate**
Formula	C_{14} H_{10} Co N_4 + disordered solvent	C_6 H_6 Co_3 O_{12}, C_3 H_7 NO
Formula weight	293.19 [*]	519.99
Crystal colour	Purple-blue	Purple
Crystal size [mmm]	0.18 x 0.23 x 0.31	0.26 x 0.28 x 0.33
Temperature [K]	150 (2)	150 (2)
Crystal system	Trigonal	Monoclinic
Space group	R-3 {No. 148}	P21/n {No. 14}
a [angstrom]	22.8401	11.3729 (4)
b [angstrom]	-	9.9463 (4)
c [angstrom]	15.8514(15)	14.5118 (6)
beta [deg]	-	91.2783 (15)
Volume [angstrom^3]	7161.3 (9)	1641.14 (11)
Z	18	4
Density calculated [g/cm^3]	1.224 [*]	2.105
(sin θ/λ)max [Å^{-1}]	0.65	0.65
μ [mm^{-1}]	1.070 [*]	3.07
abs. corr.	multi-scan	multi-scan
abs. corr. range	0.62-0.75	0.55-0.75
refl. measured / unique	20986 / 3602	37668 /3744
parameters / restraints	172 / 0	241 / 0
R1 / wR2 [I > 2.0 sigma (I)]	0.0701 / 0.2007	0.0190 / 0.0528
R1 / wR2 [all refl.]	0.1038 / 0.2147	0.0194 / 0.0530
S	1.149	1.07
p(min/max) [eÅ^{-3}]	-0.51 / 0.76	

[*] derived values do not contain the contribution of the disordered solvent.

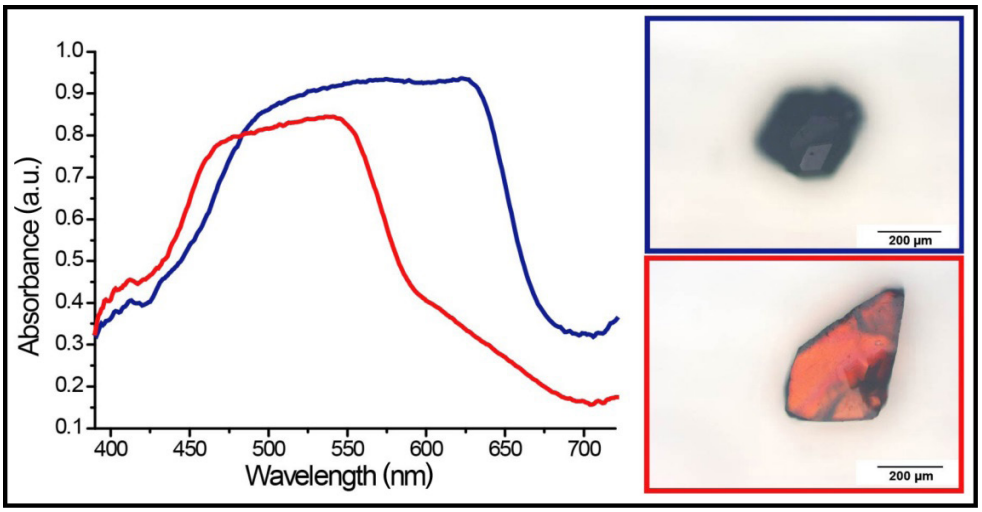

Figure 2.2. Diffuse reflectance UV-Vis spectra and corresponding optical images of individual as-synthesized Co-ZIF-9 (blue) and cobalt formate (red) crystals, obtained according to the literature synthesis procedure.

The ability of Co^{2+} ions to accommodate both tetrahedral and octahedral coordination results in the formation of two distinct materials under the synthesis conditions applied by Park et al.[16] Optical images of the obtained mixture before the separation of the crystals are shown in Figure 2.3.

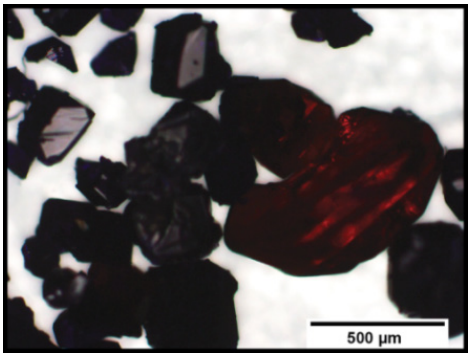

Figure 2.3. Optical image of a typical Co-ZIF-9 and cobalt formate mixture resulting from the synthesis procedure in the reported paper.[16]

Furthermore, scanning electron microscopy (SEM) was employed in order to obtain a better understanding of the morphology and the particle size of the as-synthesized Co-ZIF-9 and cobalt formate materials separated from the mixture, as shown in Figure 2.4. Figure 2.4 also gives the SEM micrograph of the Co-ZIF-9/cobalt formate mixture, which resulted from the synthesis procedure reported by Park et al.[16] The

average particle sizes were found to be around 150-200 µm and 150 µm for Co-ZIF-9 and cobalt formate, respectively.

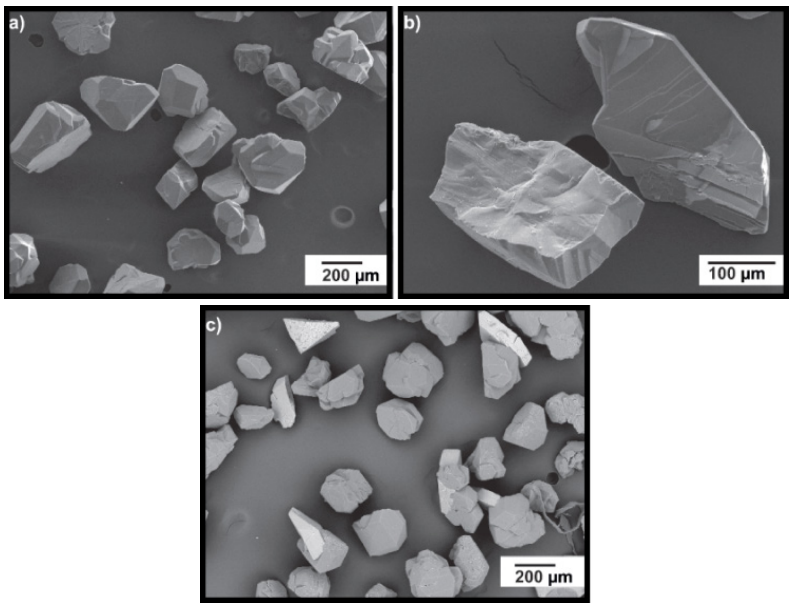

Figure 2.4. SEM micrographs of **a)** Co-ZIF-9 separated from mixture, **b)** cobalt formate separated from mixture, and **c)** Co-ZIF-9 and cobalt formate mixture.

The unexpected formation of a cobalt formate coordination polymer was also reported under hydro(solvo)thermal conditions[25] and can be explained by the generation of formate species by hydrolysis of N,N-dimethylformamide under slightly acidic conditions (initial pH ≈ 4 - 4.5). Within this context, it is important to mention that the pKA value of benzimidazole is 12.78 at 25 °C.[32] A reaction mechanism for the formation of formate has been reported previously and takes place through four subsequent steps: proton addition, hydroxylation, nitrogen deprotonation and cleavage of the C-N bond (Scheme 2.1).[33]

In a second series of experiments, the synthesis of Zn-ZIF-7 (isostructural to Co-ZIF-9) was carried out to investigate whether the formation of a secondary framework is also taking place for this material. Quite in contrast to Co-ZIF-9, the synthesis of Zn-ZIF-7 yields exclusively phase-pure ZIF material as shown in Figure 2.5. Although the hydrolysis of DMF is even likely to occur under the synthesis conditions, presumably Zn^{2+} is not able to coordinate formate ions in an octahedral geometry. Thus, the formation of the formate by-product is suppressed by the strong preference of Zn^{2+} for tetrahedral coordination.[34]

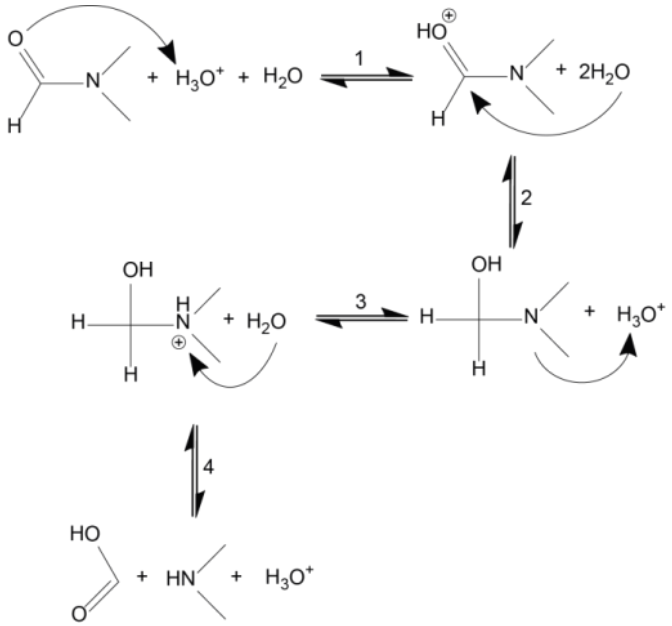

Scheme 2.1. Generation of formate species via hydrolysis of solvent N,N-dimethylformamide (DMF) during synthesis of Co-ZIF-9.[33] The mechanism proposed involves four steps; 1. proton addition, 2. hydroxylation, 3. nitrogen deprotonation and 4. cleavage of the C-N bond.

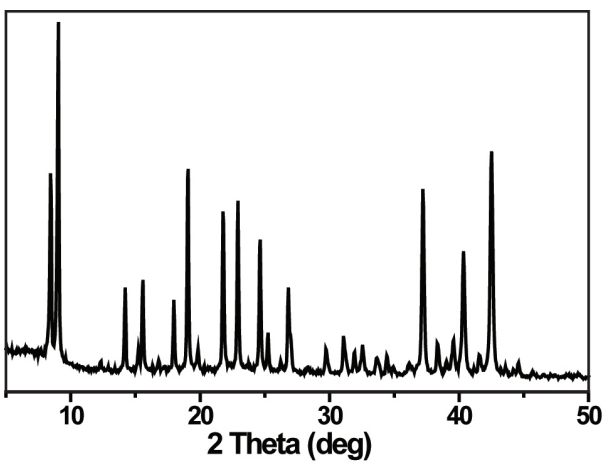

Figure 2.5. Powder X-ray diffractogram of as-synthesized Zn-ZIF-7.

However, as mentioned before, the tendency of cobalt ions to be able to occupy tetrahedral and an octahedral sites leads to the occurrence of a second cobalt formate phase. Powder X-ray diffraction (XRD) measurements were employed in order to confirm the crystallinity of the obtained Co-ZIF-9 materials when the synthesis procedure by Park et al. was applied. The powder XRD patterns, shown

in Figure 2.6, revealed the contribution of cobalt formate to the overall diffraction pattern.

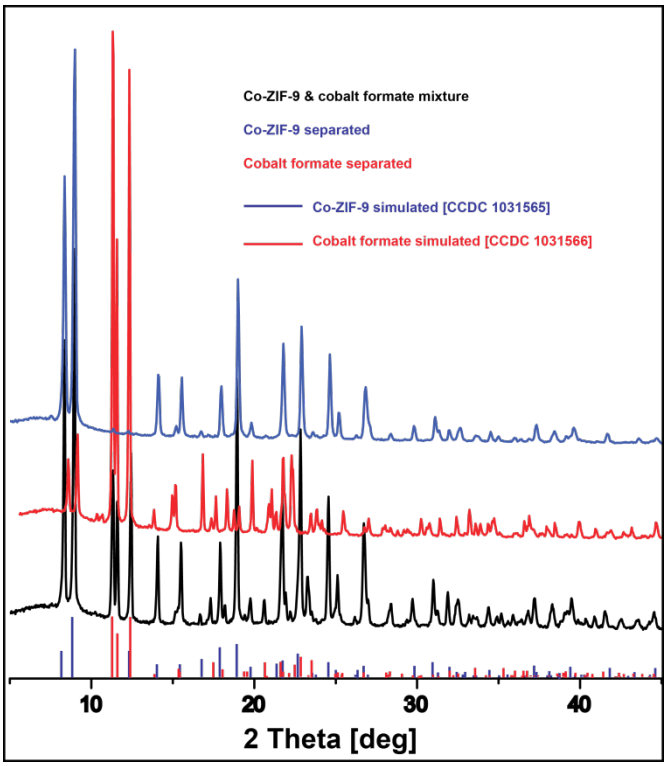

Figure 2.6. Powder X-ray diffractogram of the Co-ZIF-9 and cobalt formate mixture (black), Co-ZIF-9 (blue) and cobalt formate (red) along with the simulated XRD patterns of Co-ZIF-9 and cobalt formate. Simulation of the powder patterns has been based on the single crystal X-ray structures of the compounds.[24]

An effort to avoid the acid hydrolysis of DMF to produce phase-pure Co-ZIF-9 was accomplished by changing the pH of the solution to slightly alkaline (pH ≈ 8) by addition of solid KOH. Based on our observation, the change in the acidity of the environment suppressed the hydrolysis of DMF and hence, resulted in the formation of the desired phase-pure Co-ZIF-9. For the as-synthesized phase-pure Co-ZIF-9 material, powder XRD revealed a lower crystallinity, which can be attributed to the addition of base for pH adjustment method (Figure 2.7). In addition to these factors, which may result in a lower crystallinity, a smaller crystal size is another factor contributing to the decrease of the intensities of the diffraction peaks.

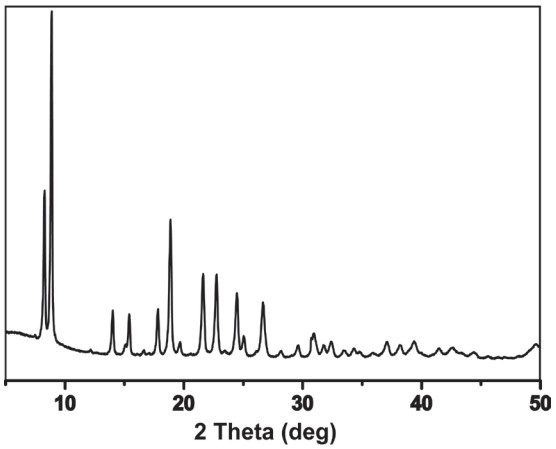

Figure 2.7. Powder X-ray diffractogram of phase-pure Co-ZIF-9 material synthesized by pH adjustment method.

The diffuse reflectance UV-Vis spectrum of phase-pure Co-ZIF-9, synthesized by the pH adjustment method along with optical images, is provided in Figure 2.8. The diffuse reflectance UV-Vis spectroscopy results are in good agreement with the formation of tetrahedrally coordinated Co^{2+} ions. The crystal sizes are found to be around 5-7 µm thus, comparatively smaller than the Co-ZIF-9 in the mixed phase. Scanning Electron Microscopy (SEM) was also employed for assessing the morphology of the as-synthesized phase-pure Co-ZIF-9 material (Figure 2.9). It was found that the particle size of the as-synthesized phase-pure Co-ZIF-9 material is around 5-7 µm.

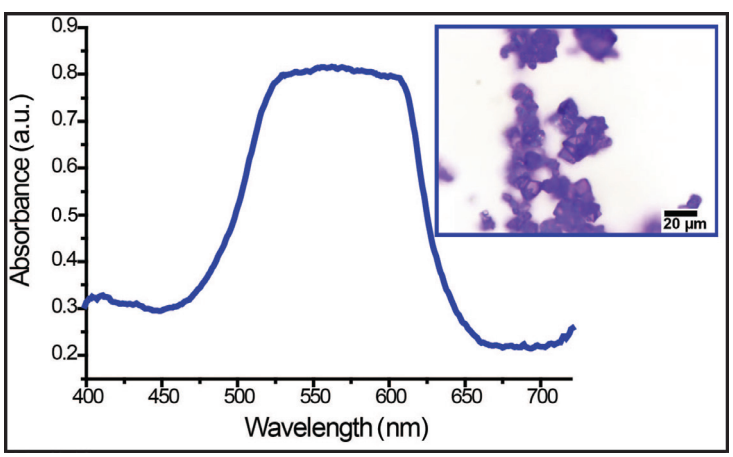

Figure 2.8. Diffuse reflectance UV-Vis spectrum and corresponding optical image of as-synthesized phase-pure Co-ZIF-9 via pH adjustment method.

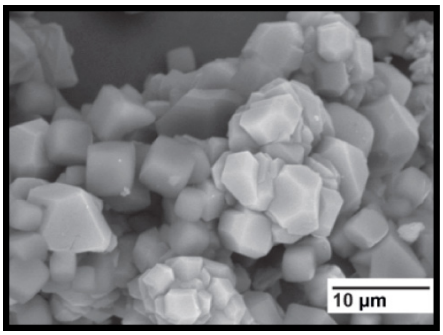

Figure 2.9. SEM micrograph of phase-pure Co-ZIF-9 synthesized via pH adjustment method.

FT-IR spectra of the as-synthesized phase-pure Co-ZIF-9 were recorded and compared with the spectrum of the pure linker benzimidazole, as shown in Figure 2.10. The major difference in the spectra of the Co-ZIF-9 is due to the disappearance of the broad N-H stretching band in the benzimidazole linker at around 2250-3500 cm^{-1}. Furthermore, disappearance of benzimidazole N-H bending bands at 628 and 1588 cm^{-1} was also observed.[35–37] These significant changes in the FT-IR spectra indicate the deprotonation of N-H groups of benzimidazole during the synthesis of Co-ZIF-9. In addition to these, full IR peak assignments of the components are provided in Table 2.2.[35–37] The appearance of new bands in the FT-IR spectrum of Co-ZIF-9 is due to the trapped/coordinated solvent DMF, which is dominantly appearing in the spectra.

The major contribution is due to the C=O bond stretching at 1672 cm^{-1} (Figure 2.10). The further peak assignments of DMF are summarized in Table 2.3.[38] The FT-IR spectrum of cobalt formate was also recorded and is given in Figure 2.10. The main characteristic O-C-O stretching bands concerning the formate species appeared at 1319 and 1581 cm^{-1}, while the O-C-O bending band was observed at 788 cm^{-1}.[39] Furthermore, FT-IR features of DMF can be observed here as well.

Table 2.2. FT-IR absorption band positions and related band intensities of phase-pure Co-ZIF-9 synthesized according to the pH adjustment method. Some band positions are due to presence of the solvent N,N-dimethylformamide (DMF).[35–37]

Wavenumbers (cm^{-1})	Intensity[a]	Assignment
652	m	C-C-C bending
663		(O=C–N) bending of DMF
739	vs	C-H bending
775	m	C-H bending
848	vw	C-C ring breathing mode

888	w	C-H bending
904	m	C-H bending
1006	m	C-C-C trigonal bending
1092		(NCH) bending of DMF
1117	m	C-H bending
1148	w	C-H bending
1178	m	C-H bending
1236	s	C-C stretching
1277	m	C-H bending
1297	m	C-N stretching
1348	w	C-N stretching
1365	w	C-N stretching
1385		C-N stretching of DMF
1459	s	C=C stretching
1608	w	C=C stretching
1672	m	(C=O) stretching of DMF

[a] w: weak, m: medium, s: strong, vw: very weak and vs: very strong.

Table 2.3. FT-IR absorption band positions and related band intensities of N,N-Dimethylformamide.[38]

Wavenumbers (cm^{-1})	**Intensity[a]**	**Assignment**
657	m	(O=C–N) bending of DMF
865	vw	(N–CH_3) stretching
1063	m	C_m–H bending
1089	s	(NCH) bending
1256	m	(N–CH_3) stretching
1385	s	(C–N) stretching
1438	m	(N–CH_3) bending
1504	m	(C–N) stretching
1664	vs	(C=O) stretching
2857-2926	m	(C–H) and (CH_3) stretching

[a] w: weak, m: medium, s: strong, vw: very weak and vs: very strong.

Furthermore, FT-IR spectra were taken for the as-synthesized phase-pure Co-ZIF-9 via the pH adjustment method and the Co-ZIF-9 separated from the mixture and are provided in Figure 2.11. The comparison of the FT-IR spectra of the phase-pure Co-ZIF-9 via pH adjustment method is in good agreement with the Co-ZIF-9, which has been separated from the mixture.

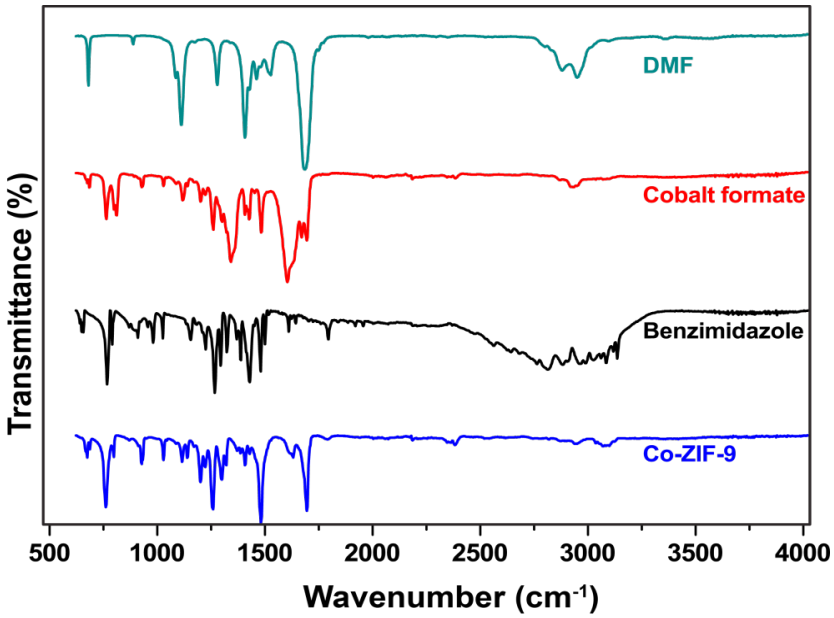

Figure 2.10. FT-IR spectra of phase-pure Co-ZIF-9, cobalt formate, benzimidazole and DMF.

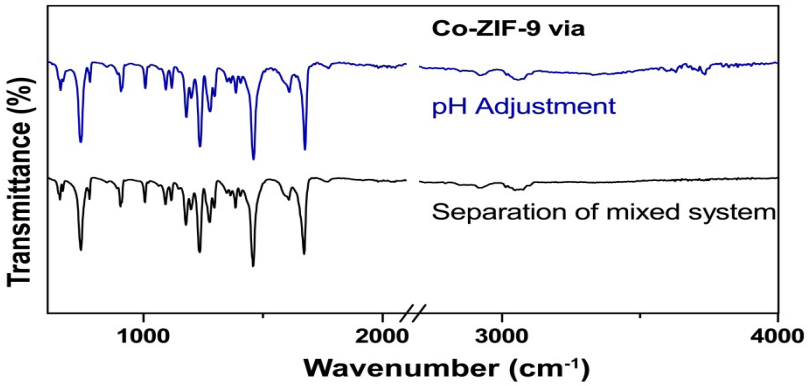

Figure 2.11. FT-IR spectra of Co-ZIF-9 via separation of mixed system and pH adjustment method.

As a complementary technique to FT-IR spectroscopy, Raman spectroscopy measurements were carried out and a comparison of the collected Raman spectra was provided in Figure 2.12. The band assignments for the phase-pure Co-ZIF-9 via pH adjustment method, Co-ZIF-9 separated from the mixture and organic linker, benzimidazole, are provided in Tables 2.4, 2.5, and 2.6, respectively. Characteristic changes in the Raman spectra of the Co-ZIF-9 materials when compared to

benzimidazole linker are due to the disappearance of the N-H stretching (625 cm^{-1}) and bending (1496 cm^{-1}) bands indicating the deprotonation of N-H groups of the benzimidazole linker during the synthesis.[35] On the other hand, the characteristic Raman bands for the cobalt formate appeared in the spectrum at 787 and 1384 cm^{-1} for bending and stretching modes, respectively.[38]

Table 2.4. Raman band assignments for the as-synthesized phase-pure Co-ZIF-9 via the pH adjustment method.[35]

Wavenumbers (cm^{-1})	Intensity[a]	Assignment
134	vs	Lattice
156	m	Lattice
199	w	
236	m	(C-C-C) out-of-plane bending
297	m	(C-C-C) out-of-plane bending
311	m	
430	vw	
468	vw	
551	w	(C-C-C) in-plane bending
652	s	(C-C-C) out-of-plane bending
774	vs	(C-H) out-of-plane bending
871	vw	(C-H) out-of-plane bending
910	w	(C-H) out-of-plane bending
1005	m	(C-C-C) trigonal bending
1020	s	(C-C-C) trigonal bending
1116	w	(C-H) in-plane bending
1146	vw	(C-H) in-plane bending
1274	s	((C-H) in-plane bending
1294	m	(C-H) out-of-plane bending
1346	m	(C-N) stretching
1364	s	(C-N) stretching
1454	w	(C=C) stretching
1464	w	(C=C) stretching
1588	w	(C=C) stretching

[a] w: weak, m: medium, s: strong, vw: very weak and vs: very strong.

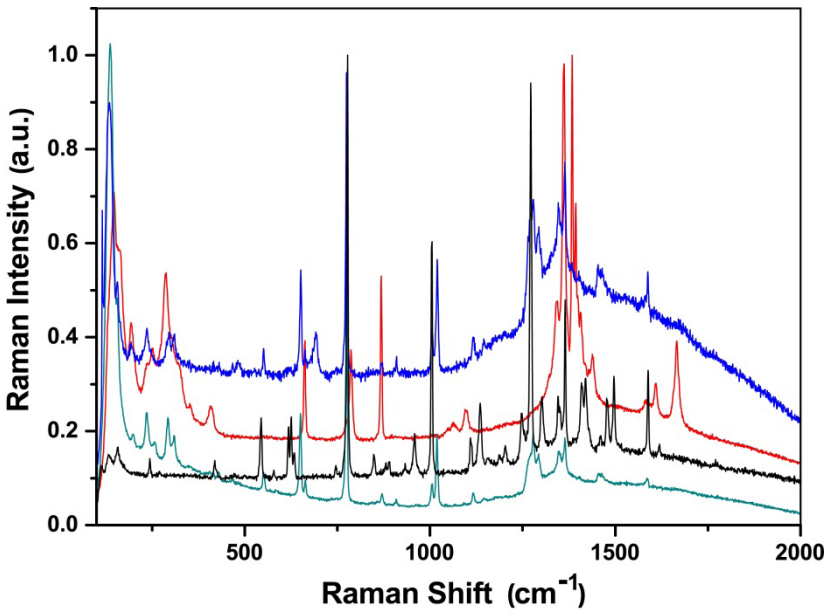

Figure 2.12. Raman spectra of Co-ZIF-9 separated (green), benzimidazole (black), cobalt formate (red), and phase-pure Co-ZIF-9 via pH adjustment method (blue).

Table 2.5. Raman band assignments for the as-synthesized Co-ZIF-9 separated from the mixture. [35]

Wavenumbers (cm^{-1})	Intensity[a]	Assignment
137	vs	Lattice
156	sh	Lattice
199	w	
236	m	(C-C-C) out-of-plane bending
293	w	(C-C-C) out-of-plane bending
310	w	
430	vw	
468	vw	
551	w	(C-C-C) in-plane bending
650	s	(C-C-C) out-of-plane bending
775	vs	(C-H) out-of-plane bending
871	vw	(C-H) out-of-plane bending
909	w	(C-H) out-of-plane bending
1005	w	(C-C-C) trigonal bending
1019	s	(C-C-C) trigonal bending
1117	vw	(C-H) in-plane bending

1146	vw	(C-H) in-plane bending
1279	m	((C-H) in-plane bending
1292	w	(C-H) out-of-plane bending
1347	vw	(C-N) stretching
1364	w	(C-N) stretching
1459	vw	(C=C) stretching
1587	vw	(C=C) stretching

[a] w: weak, m: medium, s: strong, vw: very weak and vs: very strong.

Table 2.6. Raman band assignments for the organic linker benzimidazole.[35]

Wavenumbers (cm^{-1})	Intensity[a]	Assignment
133	vw	Lattice
155	vw	Lattice
244	w	(C-C-C) out-of-plane bending
270	vw	(C-C-C) out-of-plane bending
419	w	(C-C-C) in-plane bending
544	m	(C-C-C) in-plane bending
578	vw	(C-C-C) out-of-plane bending
625	m	(N-H) out-of-plane bending
634	w	(C-C-C) in-plane bending
746	vw	(C-H) out-of-plane bending
777	vs	(C-H) out-of-plane bending
848	w	(C-C) ring breathing mode
890	vw	(C-H) out-of-plane bending
933	vw	(C-H) out-of-plane bending
958	m	(C-H) out-of-plane bending
1005	s	(C-C-C) trigonal bending
1109	w	(C-H) in-plane bending
1136	m	(C-H) in-plane bending
1186	vw	(C-H) in-plane bending
1203	vw	(C-H) in-plane bending
1248	w	(C-C) stretching
1272	vs	(C-H) in-plane bending
1302	m	(C-N) stretching
1345	m	(C-N) stretching
1365	s	(C-N) stretching
1420	m	(C=C) stretching
1477	m	(C=C) stretching

1496	m	(N-H) in-plane bending
1588	m	(C=C) stretching
1619	vw	(C=C) stretching
2873	vw	(C=C) stretching+(C-N) stretching
3065	w	(C-H) stretching
3111	vw	(N-H) stretching

[a] w: weak, m: medium, s: strong, vw: very weak and vs: very strong.

Figure 2.13 shows a comparison of a thermo-gravimetrical analysis (TGA) of i) cobalt formate separated, ii) phase-pure Co-ZIF-9 obtained by pH adjustment method, iii) the mixture of Co-ZIF-9 and cobalt formate, and iv) Co-ZIF-9 separated. Co-ZIF-9 separated exhibited the highest thermal stability, while cobalt formate exhibited the lowest. Phase-pure Co-ZIF-9 showed a relatively lower thermal stability than the Co-ZIF-9 separated material, which can be attributed to the smaller particle size.

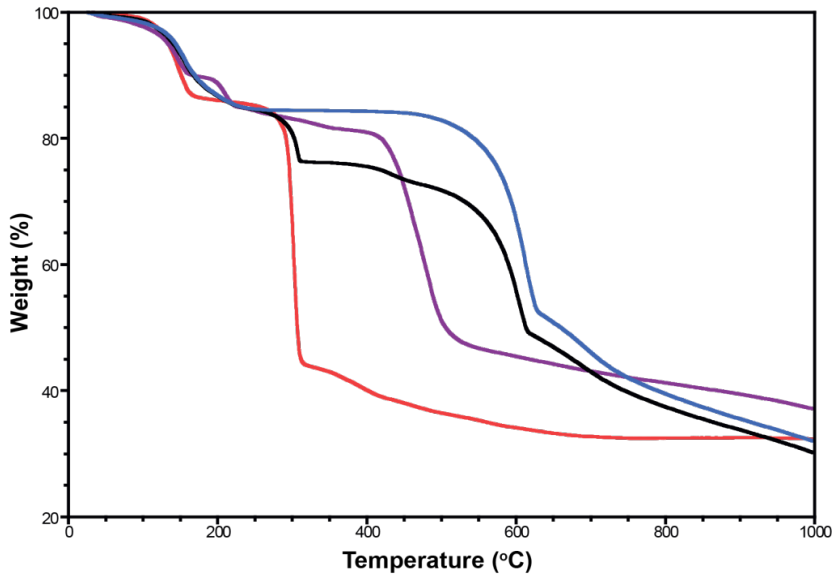

Figure 2.13. TGA curves of Co-ZIF-9 separated (blue), Co-ZIF-9 and cobalt formate mixture (black), phase-pure Co-ZIF-9 via pH adjustment method (purple) and cobalt formate (red).

Furthermore, weight losses for all systems were found to be around 15 % at 223 °C. The interesting observation for the phase-pure Co-ZIF-9 material obtained through pH adjustment method is the sharp 5 % weight loss between 157 °C and 223 °C, which can be ascribed to the more strongly physisorbed DMF molecules when compared to the TGA curves of other systems which can also account for the lower thermal stability. Efforts to remove guest DMF molecules from the pores

(activation) of Co-ZIF-9 systems were not successful due to the strongly adsorbed DMF molecules in the pores. The methods used for the activation were namely, conventional heating and vacuum, solvent exchange, and heating under inert atmosphere. The presence and the dominance of the DMF was also highlighted and demonstrated in the FT-IR spectra as illustrated in Figure 2.10. N_2 physisorption analysis revealed BET surface areas of SBET = 4 and 29 m^2/g for Co-ZIF-9-separated and Co-ZIF-9 by pH adjustment, respectively, which corresponds to outer surface area and non-accessible, hence DMF-filled pores.

2.4. Conclusions

It has been shown that the synthesis method of Park et al.[16] , commonly used for the preparation of Co-ZIF-9, yields two distinct materials, namely Co-ZIF-9 and cobalt formate. We have demonstrated a successful synthesis pathway for the preparation of phase-pure Co-ZIF-9 by eliminating the formation of the by-product cobalt formate. This could be achieved by the adjustment of the pH value of the starting synthesis mixture. The obtained phase-pure Co-ZIF-9 material was found to have a lower crystallinity, which is related to the addition of the base for the pH adjustment. Furthermore, the formation of Co formate in the synthesis reported by Park et al.[16] could be reasoned by the formation of formate ions due to acid hydrolysis of solvent DMF. The occurrence of cobalt formate can be linked to the coordination flexibility of Co^{2+} ions, which accommodate tetrahedral coordination for Co-ZIF-9 and octahedral coordination for cobalt formate. The single crystal structures of both compounds have been determined and the findings on coordination geometry, structural integrity and stability have been supported by UV-Vis, FT-IR and Raman spectroscopy, as well as by SEM, TGA and XRD.

2.5. Acknowledgements

Marjan Versluijs-Helder (UU) is thanked for the SEM measurements.

2.6. References

[1] M. Shöâeè, J. R. Agger, M. W. Anderson, M. P. Attfield, *CrystEngComm* **2008**, *10*, 646 –648.

[2] J. L. C. Rowsell, O. M. Yaghi, *Microporous Mesoporous Mater.* **2004**, *73*, 3 –14.

[3] M. J. Rosseinsky, *Microporous Mesoporous Mater.* **2004**, *73*, 15 –30.

[4] S. Kitagawa, R. Kitaura, S. Noro, *Angew. Chem. Int. Ed.* **2004**, *43*, 2334 –2375.

[5] O. M. Yaghi, M. O'Keeffe, N. W. Ockwig, H. K. Chae, M. Eddaoudi, J. Kim, *Nature* **2003**, *423*, 705-714.

[6] S. L. James, *Chem. Soc. Rev.* **2003**, *32*, 276 –288 .

[7] C. Janiak, J. Chem. Soc., *Dalton Trans.* **2003**, 2781 –2804.

[8] B. Moulton, M. Zaworotko , *Chem. Rev.* **2001**, *101*, 1629 –1658.

[9] L. Alaerts, E. Séguin, H. Poelman, F. Thibault-Starzyk, P. A. Jacobs, D. E. De Vos, *Chem. Eur.*

J. **2006**, *12*, 7353 –7363.

[10] H. K. Chae, D. Y. Siberlo-Perez, J. Kim, Y. Go , M. Eddaoudi, A. J. Matzger, M. O'Keeffe, O. M. Yaghi, *Nature* **2004***, 427*, 523–527.

[11] G. Férey, *Chem. Soc. Rev.* **2008**, *37*, 191 –214.

[12] A. Phan, C. J. Doonan, F. J. Uribe-romo, C. B. Knobler, M. O'Keeffe, O. M. Yaghi, *Acc. Chem. Res.* **2010**, *43*, 58 –67.

[13] S. R. Venna, M. A. Carreon, *J. Am. Chem. Soc.* **2010** , *132* ,76 –78.

[14] J. Zakzeski, A. Dębczak, P. C. A. Bruijnincx, B. M. Weckhuysen, *Appl. Catal. A* **2011**, *394*, 79 –85.

[15] J. Kahr, J. P. S. Mowat, A. M. Z. Slawin, R. E. Morris, D. Fairen-Jimenez, P. A. Wright, *Chem. Commun.* **2012**, *48*, 6690 –6692.

[16] K. S. Park, Z. Ni, A. P. Côté, J. Y. Choi, R. Huang, F. J. Uribe-Romo, H. K. Chae, M. O'Keeffe, O. M. Yaghi, *Proc. Natl. Acad. Sci. USA* **2006**, *103*, 10186 –10191.

[17] Q. Li, H. Kim, *Fuel Process. Technol.* **2012**, *100*, 43 –48.

[18] S. Wang, J. Lin, X. Wang, *Phys. Chem. Chem. Phys.* **2014**, *16*, 14656 –14660.

[19] C. Zhang, Y. Xiao, D. Liu, Q. Yang , C. Zhong, *Chem. Commun.* **2013**, *49*, 600 –602.

[20] *SAINT-PLUS*, Bruker AXS Inc., Madison, Wisconsin, USA, **2001**.

[21] G. M. Sheldrick, *TWINABS*, *Area-Detector Absorption Correction*, University of Göttingen, Germany, **1999**.

[22] G. M. Sheldrick, *Acta Cryst. Sect. A* **2008**, *64*, 112 –122.

[23] A. L. Spek, *Acta Crystallogr., Sect. D* **2009**, *65*, 148 –155.

[24] CCDC-1031565 (for Co-ZIF-9) and CCDC-1031566 (for cobalt formate) contain the Supplementary Crystallographic Data for this paper. These data can be obtained free of charge from The Cambridge Crystallographic Data Centre viawww.ccdc.cam.ac.uk/data_request/cif.

[25] H. S. Huh, S. W. Lee, *Bull. Korean Chem. Soc.* **2008**, *29*, 2383 –2389.

[26] K. Li, D. H. Olson, J. Y. Lee, W. Bi, K. Wu, T. Yuen, Q. Xu, J. Li, *Adv. Funct. Mater.* **2008**, *18*, 2205 –2214.

[27] Y.-L. Fu, M. Ji, X.-L. Shen, S. W. Ng, *Acta Crystallogr., Sect. E Struct. Rep. Online* **2005**, *61*, m688–m690.

[28] M. Tonigold, Y. Lu, B. Bredenkötter, B. Rieger, S. Bahnmüller, J. Hitzbleck, G. Langstein, D. Volkmer, *Angew. Chem. Int. Ed.***2009**, *48*, 7546 –7550.

[29] L. Poul, N. Jouini, F. Fie, *Chem. Mater.* **2000**, *12*, 3123 –3132.

[30] B. M. Weckhuysen, R. R. Rao, J. A. Martens, R. A. Schoonheydt, *Eur. J. Inorg. Chem.* **1999**, 565 –577.

[31] A. A. Verberckmoes, B. M. Weckhuysen, R. A. Schoonheydt, *Microporous Mesoporous Mater.* **1998**, *22*, 165–178.

[32] H. Walba, R. W. Isensee , *J. Org. Chem.* **1961** , *26* , 2789 –2791.

[33] T. Cottineau, M. Richard-Plouet, J. Mevellec, L. Brohan, *J. Phys. Chem. C* **2011**, *115*, 12269 –12274.

[34] T. Dudev, C. Lim, *J. Am. Chem. Soc.* **2000**, *122*, 11146-11153.

[35] S. Mohan, N. Sundaraganesan, *Sprectrochimica Acta* **1991**, *47A*, 1111 –1115.

[36] K. Nakamoto, *Infrared and Raman Spectra of Inorganic and Coordination Compounds, Part B*, Applications in Coordination, Organometallic, and Bioinorganic Chemistry, 6th ed., Wiley, Hoboken, **2009**.

[37] K. Nakamoto, *Infrared and Raman Spectra of Inorganic and Coordination Compounds, Part A*, Theory and Applications in Inorganic Chemistry, 6th ed., Wiley, Hoboken, **2009**.

[38] A. Sharma, S. Kaur, C. G. Mahajan, S. K. Tripathi, G. S. S. Saini, *Mol. Phys.* **2007**, *105*, 117 –123.

[39] A. M. Heyns, *J. Mol. Struct.* **1985**, *127*, 9 –20.

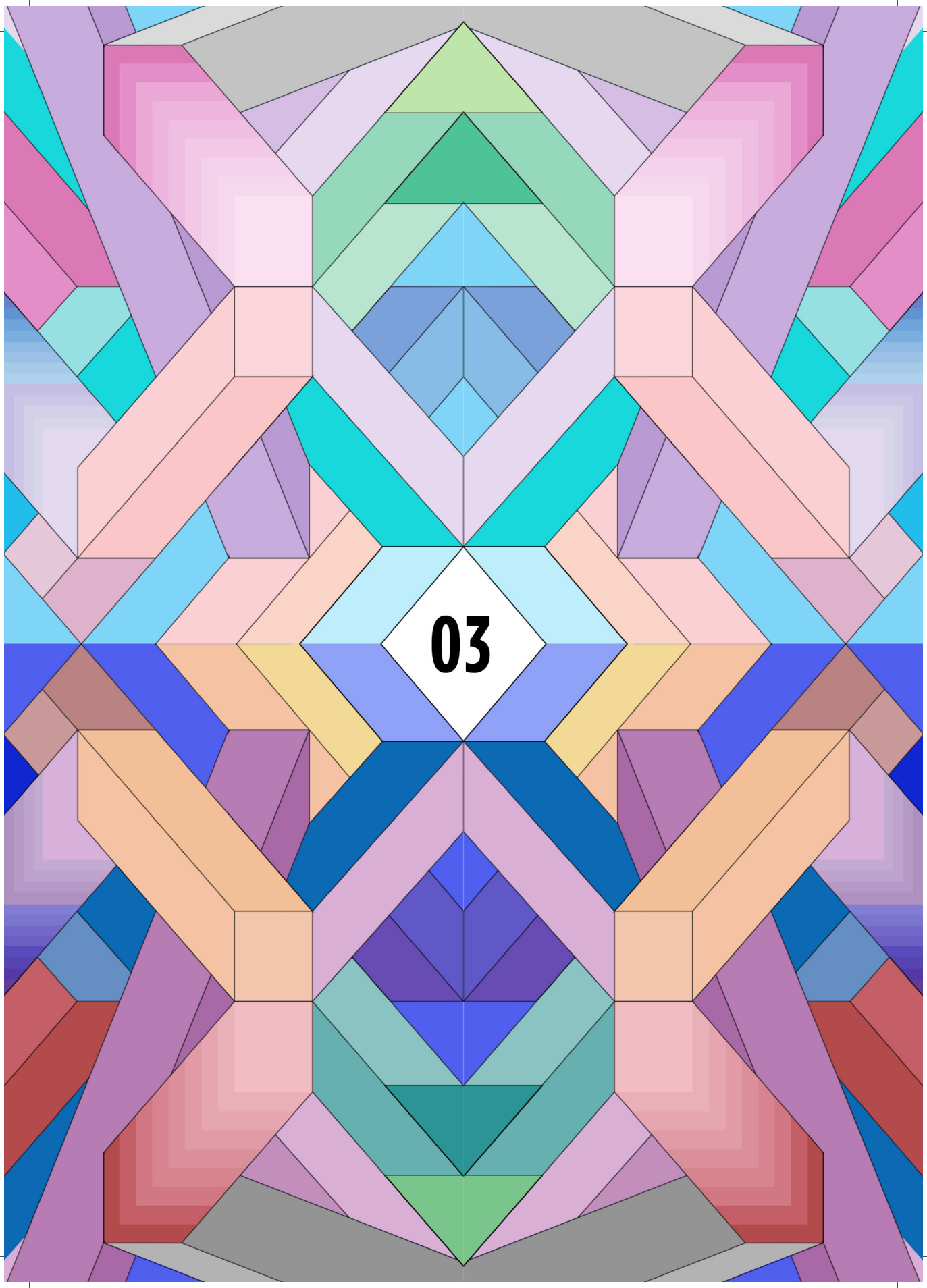
03

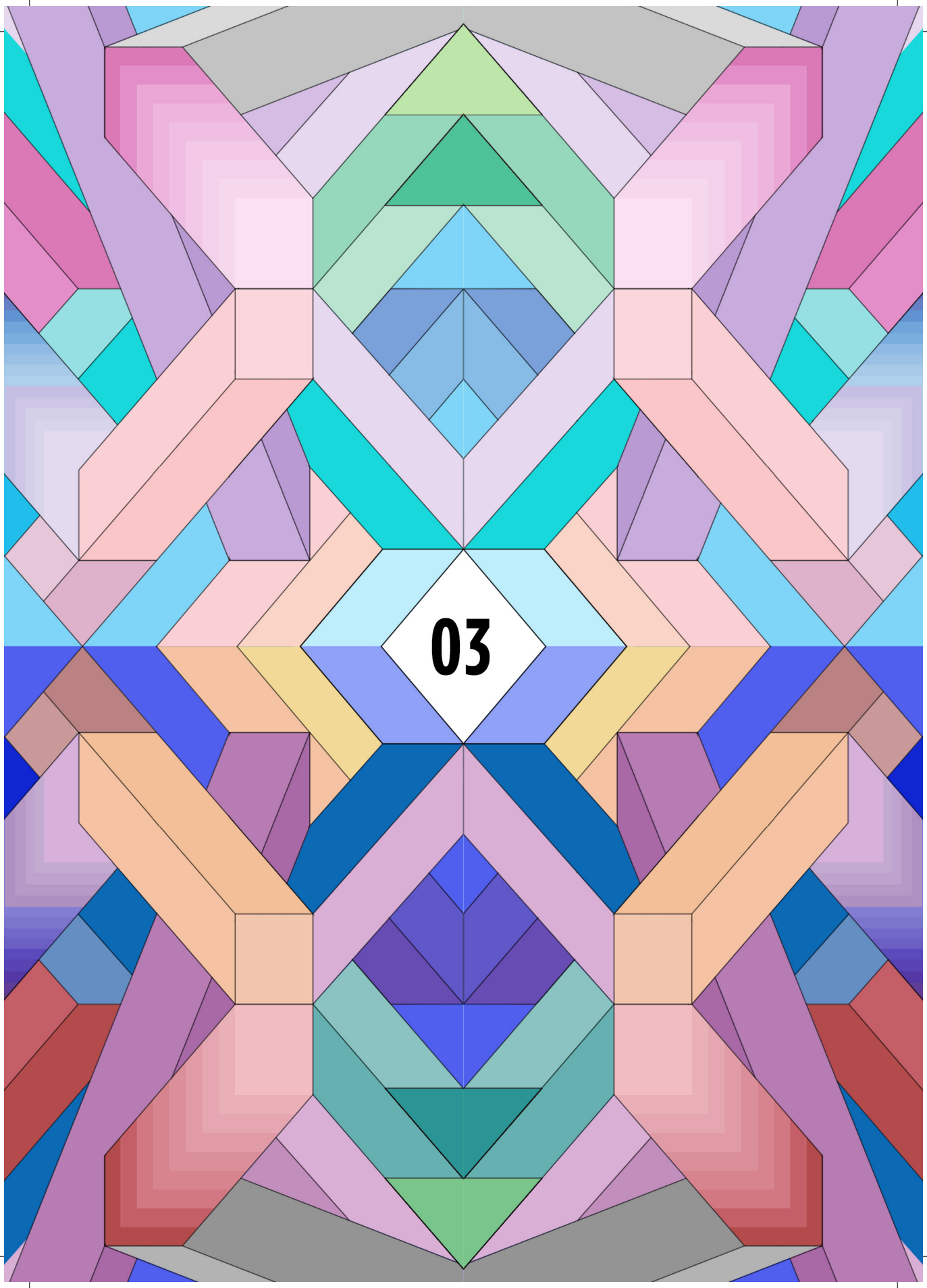
03

03

Vibrational Fingerprinting of Defects Sites in SURZIF-8 Thin-films

Abstract

Surface-mounted metal-organic frameworks (SURMOFs) are crystalline films of MOFs and have garnered a great deal of attention in the past years. So far, thin-film MOF research has been mainly focused on the synthesis and the exploration of potential applications of these materials, while a detailed understanding of their growth is still lacking. This Chapter provides experimental evidence of the inter-grown nature of surface-mounted thin-film of Zn-ZIF-8 (SURZIF-8). Two distinct SURZIF-8 thin-films have been prepared through the layer-by-layer (LBL) growth method after applying respectively 20 and 50 LBL cycles with 2-methylimidazole as linker. The materials have been characterized with a combination of Atomic Force Microscopy (AFM) and Raman spectroscopy. A detailed analysis of the mapping data with Principal Component Analysis (PCA) revealed the existence of phase boundaries within the 20 cycle thin-film, while the 50-cycle thin-film is at first sight more chemical homogeneous. To further analyse these chemical heterogeneities we have performed Density Functional Theory (DFT) calculations of three theoretical models, consisting of 2 Zn^{2+} and one linker, 1 Zn^{2+} and one linker, and only the linker. This resulted in spectroscopic fingerprints of the molecular vibrations associated with the Zn-ZIF-8 thin-film materials. By making use of these assignments, featured in four distinct spectral regions, we have been able to identify several spectroscopic markers, indicative for the presence of defects sites (i.e., the free linker as well as a linker coordinated to only one Zn^{2+} ion). More specifically, it was found that the relative intensities of the ~ 1135, 1180 and 1498 cm^{-1} Raman bands, are diagnostic for the presence of structural defects and can be used for spectral zoning and Raman mapping.

This Chapter is based on: Z. Öztürk, R. P. Brand, J. Boereboom, F. Meirer and B. M. Weckhuysen, Vibrational Fingerprinting of Defects Sites in SURZIF-8 Thin-films, in preparation.

3.1. Introduction

The recent decades have witnessed the discovery, characterization and performance testing of a wide variety of Metal-Organic Frameworks (MOFs) and related porous structures.[1–4] The fact that MOFs consist of both inorganic and organic building blocks provides ample opportunities to design MOFs with tunable functional properties, leading to various applications in the fields of catalysis,[5–7] drug delivery,[8,9] sensing,[10,11] biomedical imaging,[8] and gas adsorption.[12–14] An emerging class of MOFs is Zeolitic Imidazolate Frameworks (ZIFs).[15] The word ''*zeolitic*'' is derived from their zeolite-like framework topologies, while the term ''*imidazolate*'' relates to the presence of imidazolate linkers or their derivatives. ZIF frameworks are formed through tetrahedral coordination of transition metal ions (e.g., Co^{2+}, Zn^{2+}, Cu^{2+} or Fe^{2+}) with imidazolates or its derivatives acting in the same way as silicon and aluminum atoms are covalently joined by the bridging oxygen atoms in zeolites.[16,17] Since the metal ion-imidazolate-metal ion angle is similar to the 145° Si^{4+}-O-Si^{4+} angle in zeolites, ZIFs have zeolite-like topologies. One of the prototype materials of the ZIF family is Zn-ZIF-8, one of the most widely studied ZIFs.[18–21] Zn-ZIF-8 is composed of Zn^{2+} ions tetrahedrally coordinated to bridging 2-methylimidazolates, and has the sodalite topology with 1.16 nm wide cavities formed by 4-ring and 6-ring Zn-N_4 clusters leading to 0.34 nm wide windows, as illustrated in Figure 3.1a.[20–25]

There has been substantial attention towards the growing of MOFs in the form of a thin layer anchored to a surface, which are known as surface-mounted metal organic frameworks (SURMOFs).[15,26–28] The thin-film morphology of MOFs is required in certain applications for their proper functioning, which is unfortunately not available for MOF powders with a few μm of particle size.[29] MOF thin-films have potential use in the fields of luminescence,[30] QCM-based sensors,[31,32] catalysis,[33,34] as well as gas separation.[35–37] There have been so far three main strategies for the preparation of SURMOFs reported in the literature, which are direct growth from a mother liquor, assembly of preformed MOF crystals and the step-wise layer-by-layer (LBL) growth onto a substrate.[27,28] In the LBL growth of SURMOFs functionalized substrates are vital for directing the nucleation, orientation and the structure of the MOF growth.[38] Similarly, ZIF thin-films can be prepared by direct synthesis, seeded growth, electrochemical methods and assembly of preformed crystals.[27,29]

In this Chapter, we present the systematic synthesis of thin-films of ZIF-8 (SURZIF-8) by using the stepwise layer-by-layer method. Two distinct SURZIF-8 samples were prepared through a layer-by-layer method after applying 20 and 50 LBL cycles. The detailed chemical imaging of these two materials was provided by Raman

microscopy, while for the height information and the surface morphology Atomic Force Microscopy (AFM) was used. Density Functional Theory (DFT) calculations were conducted in order to calculate the molecular vibrations, helping to identify the observed experimental vibrations. Furthermore, Principle Component Analysis (PCA) was used in order to determine correlations between the spectroscopic and morphological spatial information of the two SURZIF-8 materials. PCA analysis shows the presence of a phase boundary in the 20 LBL cycle sample, whereas its 50 LBL cycle analogue exhibits a more homogeneous nature. Detailed analysis of the individual Raman spectra of the clusters revealed the presence of defects sites and the identification of diagnostic Raman bands, which undergo intensity changes and/or band splitting/shifts, indicative for structural defects. DFT calculations on model clusters were executed for the spectroscopic identification of these fingerprint vibrations, providing detailed insight in the structural heterogeneities present within the two Zn-ZIF-8 thin-films under investigation.

3.2. Experimental

3.2.1. Layer-by-layer Synthesis of Zn-ZIF-8 Thin-Films

The synthesis of Zn-ZIF-8 thin-films was carried out through a layer-by-layer (LBL) method, which was adapted from a study by Eddaoudi et al..[19] The synthesis was performed through an automated peristaltic pump system in a home-built glass set up, as illustrated by a picture in Figure 3.1.b and as schematically outlined in Figure 3.1.c. Figure 3.1.a shows the crystal packing of the Zn-ZIF-8. 10 mM of a 11-mercapto-1-undecanol (MUD) (Sigma-Aldrich, 97%) ethanolic solution (Acros, extra dry) was used for the modification of gold-coated silicon wafers. 10x10 mm of 60 nm Au coated Si wafers with Ge adhesion layer were purchased from Amolf (FOM institute, the Netherlands). Au-coated substrates were first cleaned in a UV-ozone cleaner for 15 min and then placed into vials containing 2mL of 10 mM MUD ethanolic solution for 4 h. After 4 h of self-assembly, Au-coated substrates were dried under gentle N_2 stream and were placed into a glass set up. 100 mM and 50 mM of $Zn(NO_3)_2 \cdot 6H_2O$ (Sigma-Aldrich, 99%) and 2-methylimidazole (Sigma-Aldrich, 99%) methanolic (Acros, extra dry) solutions were prepared, respectively. 2 and 3 min deposition times were applied for 1.5 mL of Zn^{2+} and 2-methylimidazolate methanolic solutions, respectively at room temperature. The Au-coated substrates were rinsed with fresh methanol between each step in order to remove unreacted species. This deposition process composed of four subsequent steps corresponds to ‘one cycle’ of deposition (Figure 3.1b). In this work, two SURZIF-8 samples have been prepared with 20 and 50 LBL cycles.

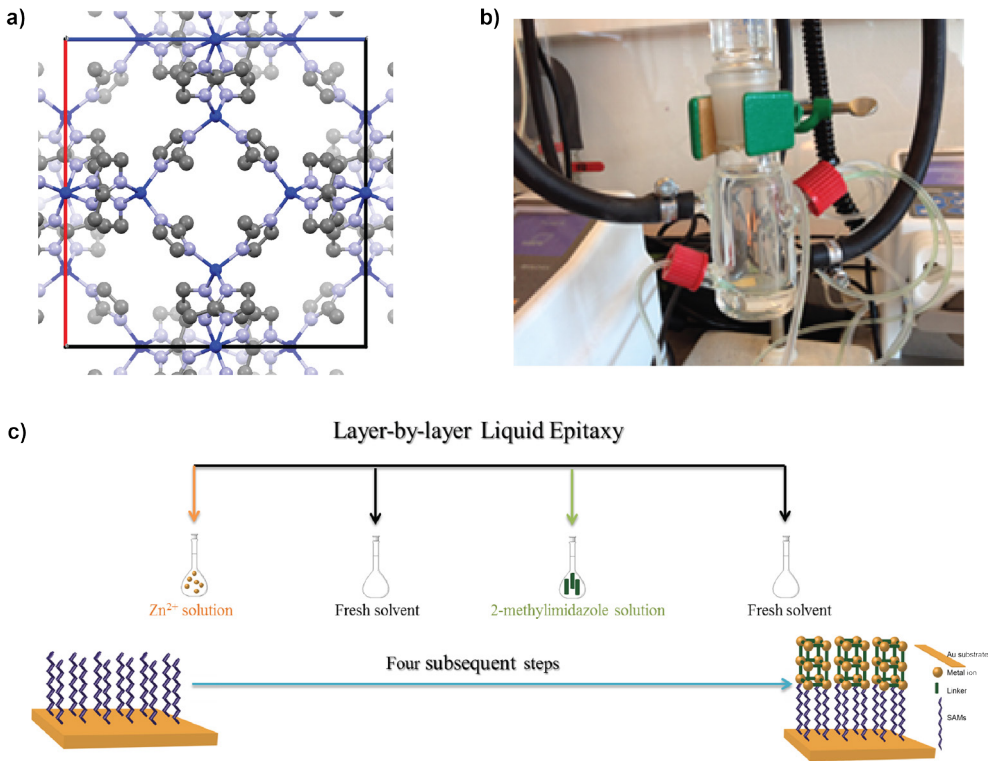

Figure 3.1.a. The coordination sphere of the Zn-ZIF-8 material (hydrogen atoms are omitted for clarity, grey: carbon, light blue: nitrogen, dark blue: zinc). **b)** Glass set-up designed for the layer-by-layer (LBL) growth of SURZIF-8 where tubings are used for the liquid flow, which is controlled by an automated peristaltic pump. **c)** Schematic representation of 'one cycle' growth on a Au-coated substrate with self-assembled monolayers (SAMs) in the LBL method where four subsequent steps are involved.

3.2.2. Characterization of Bulk Zn-ZIF-8 and Zn-SURZIF-8 Thin-film

Raman spectroscopy measurements were performed with a Renishaw InVia micro-spectrometer making use of a 785 nm laser and the spectra were recorded in the region of 100-3200 cm^{-1}. For all measurements a 785 nm laser was used with a 600 lines per millimeter grating. The spectra during the Raman measurements were recorded in a region of 100x100 μm^2 with the grating at a static position with the spectral centers at 520 and 1180 cm^{-1}. Atom Force Microscopy (AFM) measurements of 100x100 μm^2 scans were executed for the samples with high resolution (1024x1024 pt^2) in order to obtain topographical information. The AFM scans were conducted on a NT-MDT NTEGRA Spectra upright AFM unit and Olympus AC 160TS tips were used for all AFM measurements.

3.2.3. Data Processing and Analysis

Principal Component Analysis (PCA)[39] was performed for the analysis of the raw micro-spectroscopy data, data with the spectral background subtracted and for the normalized background subtracted data. A spectral map consisted of m x m pixels (M) with a spectrum consisting of W measured wavenumbers at every pixel. The value m was 101 for the Raman spectral maps. For this reason we used PCA to reduce the size of the dataset from a dataset of size M x W to a dataset of size M x N, where N is significantly smaller than W, effectively reducing the data set without losing relevant information by preserving most of the variance in the data. [40,41] PCA produces principal components (PCs) that are linear combinations of the W independent variables. The PCs form an orthonormal basis set that is aligned to best express the data with respect to its variance. Every PC covers a fraction of the data's variance, which in turn is used to assess the importance of each PC to describe the data set ('variance explained' of each PC). The PCs were determined by singular value decomposition (SVD) of the M x W matrix resulting in a new matrix M × PC1...W, where the PCs (columns) are eigenimages, while the rows represent eigenspectra. In this representation there are still W PCs, but this number can now be reduced to N PCs, by keeping only the PCs that describe most of the variance (information) in the data. In this study, the first 4 PCs (N=4) were retained based on an inspection of the cumulative variance explained (CVE) by all PCs. In this reduced data set every pixel M is now characterized by 4 parameters (the 'scores' of the 4 PCs) that are a linear combination of the original W parameters (wavelengths). By plotting the M pixels in this 4 dimensional space defined by the orthonormal basis set formed by the PCs (score plot), one can learn about the similarity of two spectra by looking at their (Euclidean) distance within this plot. The closer two points are in this space the more similar are their spectra and thus their chemical identity. We therefore used k-means clustering[42,43] of the data points in the 4-dimensional PC space to pool pixels with most similar spectral fingerprints. K-means clustering requires defining the number of clusters a priori; in this work we therefore followed to approach to first intentionally over-cluster the data set by choosing the number of clusters to be twice the number of principal components used. Then in a second, refining step we performed a density based clustering (Expectation Maximization (EM) for Gaussian Mixture Models (GMM)) using the result of the k-means clustering as an initial guess. Finally, upon inspection and comparison of the average spectra of each of the clusters resulting from k-means and EM-GMM, clusters that showed insignificantly different spectra have been merged.

3.2.4. Theoretical Calculations

Density Functional Theory (DFT) calculations have been performed to obtain the vibrational frequencies of model systems of SURZIF-8 systems and their building blocks. Geometry optimization of these systems and the related constituents were performed with the ADF program package[44] using the PBE functional[45] and a TZP basis set.[46] For the frequency analysis of the FT-IR spectra the analytical gradients were used.[47–49] The Raman spectroscopy theoretical calculations[50,51] use a laser frequency of 1.58 eV corresponding to the experimental laser used of 785 nm. In order to compare better with experimental spectra, the theoretically calculated frequencies of the Raman spectra are broadened by a Gaussian with a half width of 10 cm^{-1}.

3.3. Results and Discussion

3.3.1. Combined AFM-Raman mapping of SURZIF-8 materials

Atom Force Microscopy (AFM) measurements were performed in a region of 100x100 μm^2 in order to obtain spatial information on the morphology and height of the two thin-film samples under study. Figure 3.2 shows the AFM scans of the Zn-ZIF-8 thin-films obtained after 20 and 50 LBL cycle. It is important to remark here that the defect observed as a blue area in the center of the AFM micrograph of the 20 LBL cycle Zn-ZIF-8 thin-film sample originates from the Raman laser exposure during the Raman micro-spectroscopy measurements executed before performing the AFM scans. This illustrates that the Zn-ZIF-8 thin-films prepared are rather sensitive to laser Raman irradiation. Regarding the thickness of the samples under study, no direct information could be obtained because of the high degree of surface coverage, although local internal height differences throughout the 100x100 μm^2 region were successfully acquired. The maximum height difference between the 20 and 50 LBL cycle Zn-ZIF-8 samples was found to be higher in the 50 LBL cycle Zn-ZIF-8 sample than in the 20 LBL cycle Zn-ZIF-8 sample (~ 3 µm versus ~ 1.3 µm). This large height difference stems from the two highest grains observed in the 50 LBL cycle Zn-ZIF-8 thin-film, clearly visible in Figure 3.2b. Furthermore, the number of grains is higher in the case of the 20 LBL cycle Zn-ZIF-8 sample indicating that after 30 more extra cycle a more homogeneous and inter-connected film structure is formed due to a decreasing distance between the different Zn-ZIF-8 grains formed.

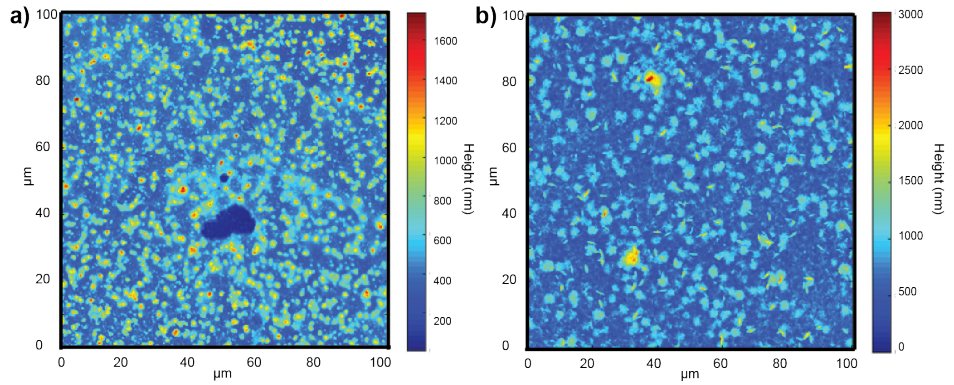

Figure 3.2. Atom Force Microscopy (AFM) micrographs of the two Zn-ZIF-8 thin-films under study as made by the layer-by-layer (LBL) synthesis method: **a)** 20 LBL cycle Zn-ZIF-8 sample and **b)** 50 LBL cycle Zn-ZIF-8 sample.

In addition to the morphological information acquired from the AFM data, we have performed Raman micro-spectroscopy measurements on both samples in order to provide chemical information regarding the formation of Zn-ZIF-8 thin-film material. The Raman spectra obtained through single point measurements are displayed in Figure 3.3.a and 3.3.b for the 20 and 50 cycle Zn-ZIF-8 thin-films, respectively. The Raman spectra of the thin-films confirm that the chemical bond structure corresponds to that previously reported literature results for Zn-ZIF-8. [13,52] The Raman spectra of Zn-ZIF-8 exhibited characteristic bands, namely, Zn-N stretching (~ 139 cm^{-1}), imidazole ring puckering (~ 686 cm^{-1}), C=C stretching (~ 1505 cm^{-1}), CH_3 (~ 2926 cm^{-1}) and C-H aromatic (~ 3130 cm^{-1}) stretching modes.[13,53] The comparison of the large dataset of Raman spectra of the 20 and 50 LBL cycle thin-films clearly reveal spectral differences arising from 1) intensity changes and 2) band aspect ratio variations along with band broadening/splitting and also spectral shifts. These spectral differences and variations require further analysis as they may provide a basis to determine spectroscopic fingerprints for defect sites in SURZIF-8 thin-films, and MOF and ZIF materials in more general.

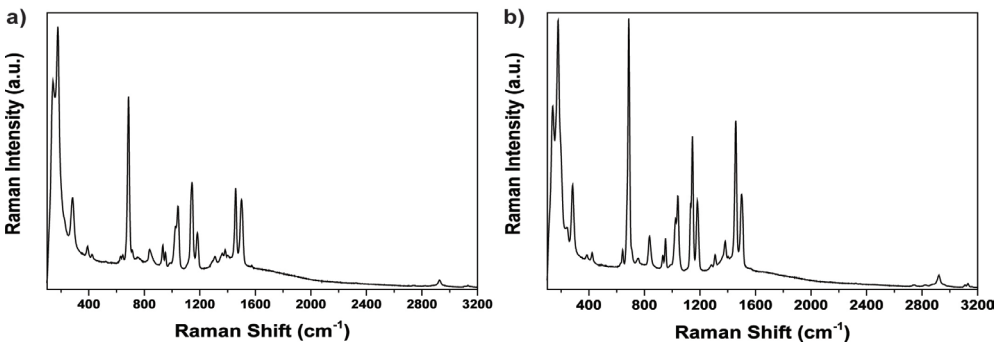

Figure 3.3. Characteristic Raman spectra of the two Zn-ZIF-8 thin-films under study as made by the layer-by-layer (LBL) synthesis method: **a)** 20 LBL cycle Zn-ZIF-8 sample b**)** and 50 LBL

cycle Zn-ZIF-8 sample.

To do this, we have first performed combined AFM and Raman mapping measurements as one may expect that the topology differences in the AFM maps for both samples may harbor these spectral changes. As a result, both mapping experiments have been done for the same 100x100 μm^2 region of the two thin-film samples with the goal of correlating the topographical information with the spectral information. The Raman micro-spectroscopy mapping measurements were carried out for two sub-spectral regions, namely we have measured 1) a set of Raman spectra, which centers at 520 cm^{-1} and 2) a set of Raman spectra, which centers at 1180 cm^{-1}, thereby covering respectively the two spectral regions from 100 to 950 cm^{-1} and from 800 to 1550 cm^{-1}.

Principal component analysis (PCA) was then applied on both sets of Raman spectra and for the two samples in order to get better information throughout the mapped 100x100 μm^2 region. All measured Raman spectra were pre-processed, by subtracting the background and normalizing every individual spectrum to its own minimum and maximum values. Afterwards, three versions of the data; namely, raw, background corrected, and the one that was also subsequently normalized were analyzed. This analysis consisted of a PCA step followed by k-means clustering with subsequent EM for GMM refinement.

For the first spectral region of interest (100-950 cm^{-1}), the results of the fully pre-processed data for both 20 and 50 LBL cycle samples are provided in Figure 3.4.a and 3.4.b, respectively. Pixels with the same color within an individual image correspond to the same cluster and thus indicating a mutual spectral similarity, as can be evaluated from the averaged cluster Raman spectra, given in Figure 3.4.c and 3.4.d. The same color codes were utilized for these spectra in line with their clustering analogues for clarity. Very interestingly, Figure 3.4.a shows a clear phase boundary in the cluster maps of the 20 LBL cycle sample between the upper and lower half of the Raman map in the 100-900 cm^{-1} spectral region. Figure 3.4.c gives insights to the differences observed in the Raman maps of 20 LBL cycle sample as the comparison of the spectra of each clusters show intensity and band ratio differences as well as a band broadening and spectral shifts. In Figure 3.4.a, Raman spectra of the clusters; red, orange, brown and grey share similar spectral features (mainly located in the upper part of the Raman map), whereas the other three clusters, namely blue, yellow and magenta (mainly located in the lower part of the Raman map) share a lot of spectral similarities. In other words, the differences in these two groups of colour clusters are reflected by the phase boundary. It should also be mentioned that the clusters with the colours of orange and magenta have dominance throughout the Raman map. Furthermore, in the Raman map of the 20

LBL cycle sample, the contribution arising from blue cluster is populated in the lower region of the map and also acts as an intermediate between observed these two phases. It is important to stress here that such phase boundary is completely absent in the corresponding AFM micrograph of the 20 LBL sample (Figure 3.2.a). This also explains that AFM is not sensitive to the detection of chemical heterogeneities. In other words, the observed observations in height and grain size are not sufficient to explain the chemical differences observed in the Raman spectra. From the Raman spectra in Figure 3.4 c it should also be clear that spectra in the lower part are clearly distinct from those found in the Raman map of the 50 LBL sample (Figure 3.4 b). This Raman map reveals a more homogeneous nature of the Zn-ZIF-8 sample. The red and yellow clusters are indeed abundant throughout the Raman map, while the Raman spectra corresponding to each of the other clusters (Figure 3.4. d) are very alike and there is not much spectral variance in the data.

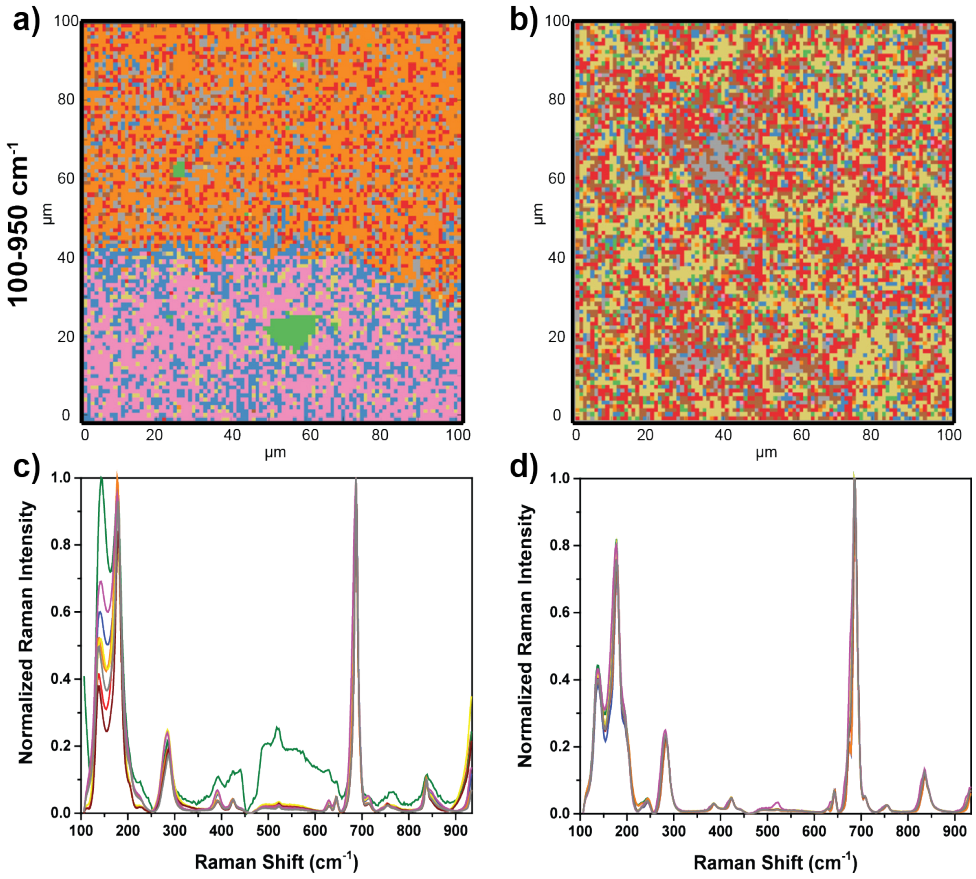

Figure 3.4. Result of the Principal Component Analysis (PCA) clustering analysis of the Raman microscopy maps for the 100-950 cm^{-1} spectral region based on Expectation Maximization (EM) for Gaussian Mixture Models (GMM), both for the 20 LBL cycle Zn-ZIF-8 sample (**a)** and

the 50 LBL cycle Zn-ZIF-8 sample (**b**). The Raman spectra belonging to the different clusters, with each there typical colour code, as obtained from the EM for GMM PCA analysis of the Raman microscopy maps, both for the 20 LBL cycle Zn-ZIF-8 sample (**c**) and 50 LBL cycle Zn-ZIF-8 sample (**d**).

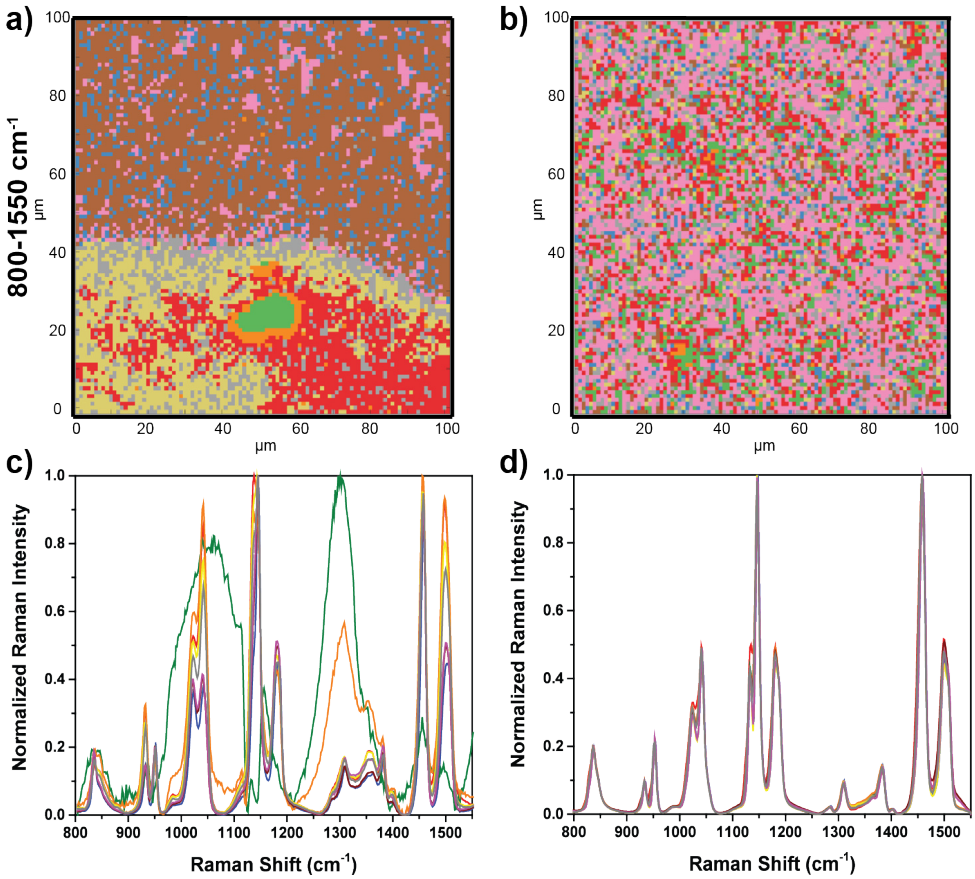

Figure 3.5. Result of the Principal Component Analysis (PCA) clustering analysis of the Raman microscopy maps for the 800-1550 cm^{-1} spectral region based on Expectation Maximization (EM) for Gaussian Mixture Models (GMM), both for the 20 LBL cycle Zn-ZIF-8 sample (**a)** and the 50 LBL cycle Zn-ZIF-8 sample (**b**). The Raman spectra belonging to the different clusters, with each there typical colour code, as obtained from the EM for GMM PCA analysis of the Raman microscopy maps, both for the 20 LBL cycle Zn-ZIF-8 sample (**c**) and 50 LBL cycle Zn-ZIF-8 sample (**d**).

For the second spectral region of interest (800-1550 cm^{-1}), the results of the fully pre-processed data for both 20 and 50 LBL cycle samples are provided in Figure 3.5.a and 3.5.b, respectively. Here again, pixels with the same color within an individual image correspond to the same cluster and thus indicating a mutual spectral similarity, as can be evaluated from the averaged cluster Raman spectra given in Figure 3.5.c and 3.5.d. The same color codes were again used for these spectra in line with their

clustering analogues for clarity. Similar as for the 100-950 cm^{-1} region, the 20 LBL cycle sample also exhibits in the 900-1550 cm^{-1} region strong spectral differences in terms of intensity, band ratios and as well as spectral shift and band broadening (Figure 3.5.c). The clusters with similar spectral intensity and band ratios can be divided into two groups again as clusters blue, brown, magenta and red, yellow, orange, grey and these differences result in the phase boundary, as observed in Figure 3.5.a. The phase boundary is also located at the same place as in Figure 3.4.a, providing a consistent spectroscopic picture of this sample. The cluster designated with green colour is the region damaged by Raman laser exposure as highlighted before. The grey cluster is present mostly in the lower phase and predominantly located across the phase boundary acting as an intermediate. Furthermore, in Figure 3.5.a in the lower part of the Raman map, there is a sharp transition between yellow and red cluster regions and this difference is arising not only from an intensity related difference, but also band broadening and spectral shift of the bands located at ~ 1144, ~ 1180, ~ 1456 and ~ 1498 cm^{-1}. This can be inferred from Figure 3.5.c. These bands can be assigned as coupling of ring deformation and C-H bending. The main spectral differences in these two distinct groups of clusters in the upper and lower region can be attributed to the same vibrational bands located at ~ 1144, ~ 1180, ~ 1456 and ~ 1498 cm^{-1}.

In stark contrast, the Raman map of the 50 LBL cycle sample, as shown in Figure 3.5.b, displays the well inter-grown nature of this thin-film, although still chemical heterogeneities can be noted from the distinct Raman spectra observed for e.g. the Raman spectra corresponding to the red, grey and yellow regions. Nevertheless, the spectral differences are relatively minor for the 50 LBL cycle sample (3.5.d) and the spectra are much more alike those found in the upper part of the Raman map of the 20 LBL cycle sample.

3.3.2. Theoretical Calculations on SURZIF-8 Model Systems

From comparison between the AFM and Raman maps for both Zn-ZIF-8 thin-films it becomes clear that we are now in the procession of a unique set of samples, which may provide further insights in the presence of chemical heterogeneities within these thin-films. By providing a more detailed interpretation of the Raman spectra it might become possible to obtain spectroscopic fingerprints of defects sites present in these framework structures. In order to do so we have performed a theoretical investigation. More specifically, we have aimed to calculate with Density Functional Theory (DFT) three models system: Linker (2-methylimidazole) coordinated with two Zn^{2+}-ions, Protonated linker coordinated to one Zn^{2+}, and the isolated protonated linker (with no Zn^{2+}-ions coordinating). These three model structures

are visualized and named in Table 3.1. For these three models the corresponding IR and Raman spectra are calculated. We expect that the 2 Zn + linker models reflects the structure of the Zn-ZIF-8 thin-films. If there is a defect (missing cation), one of the zinc molecules will be missing, and subsequently the linker gets protonated (1 Zn + linker model). The only linker model can be used to see if there are any floating linkers.

Table 3.1. The naming and structure of the three different model clusters used to investigate and characterize the possible defects in Zn-ZIF-8 thin-films with DFT.

Name	2 Zn + linker	1 Zn + linker	Only linker
Structures	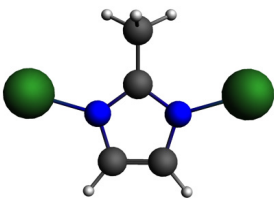	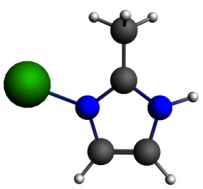	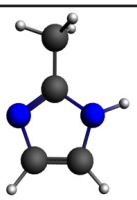

In a first stage of our theoretical investigation we have a look at the Raman spectra of the 2Zn + linker, 1Zn + linker, and only linker models that can be found in Figure 3.6. The first thing to note is that the Raman intensity of the normal modes up to 1500 cm^{-1} is quite different for the different models. The zinc atoms seem to enhance the Raman intensity in this spectral region; this also means that the Raman intensity above 2800 cm^{-1} is similar for all three models, as the zinc atoms do not take part in the normal modes in that region.

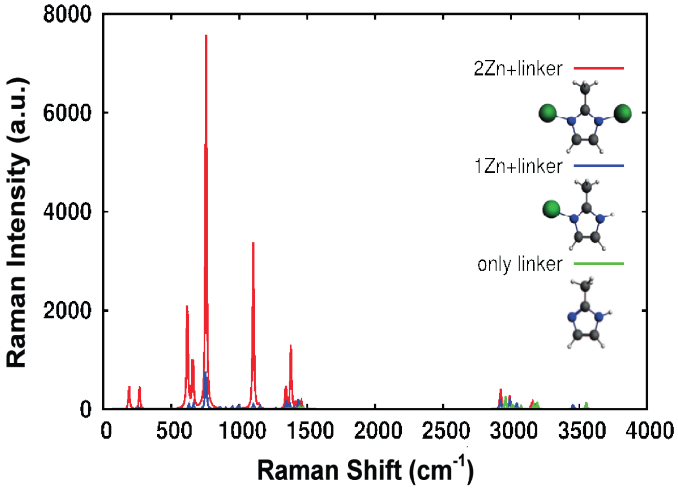

Figure 3.6. The Raman spectra of the 2 Zn + linker, 1 Zn + linker and only linker models. The spectra are broadened by a Gaussian profile with half width of 10 cm^{-1} in order to reflect experimental Raman spectra. Note that these spectra are not normalized.

We will now focus on the Raman spectra up to 1600 cm^{-1}, where we will normalize the Raman spectra so that we can compare the three cluster models more easily. In Figure 3.7 the normalized Raman spectra of the 2 Zn + linker, 1 Zn + linker and only linker models can be seen. For the 2 Zn + linker and 1 Zn + linker models we use the normal mode at 754 and 753 cm^{-1}, respectively, to normalize the Raman spectra. These normal modes can be seen in Table 3.2.

Table 3.2. Sideview and topview of the normal modes used to normalize the Raman spectra of the 2 Zn^{2+} + linker and 1 Zn^{2+} + linker theoretical models.

Normal mode	Sideview	Topview
2 Zn + linker 754 cm^{-1}	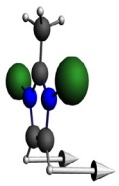	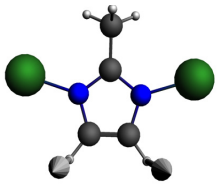
1 Zn + linker 753 cm^{-1}	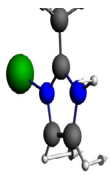	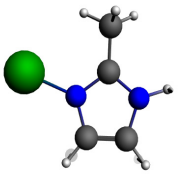

If we have a look at the first inset (**spectral region A**, from 230 to 290 cm^{-1}) of Figure 3.7, we can see that the 2 Zn + linker model has one normal mode at 266 cm^{-1}, and the 1 Zn + linker model has two normal modes at 256 and 264 cm^{-1} that overlap to form one peak. The normal mode of 256 cm^{-1} is about 50 to 60 % more intense than the peak at 264 cm^{-1} leading to a small, but significant, shift compared to the 2 Zn + linker model. The only linker model has one normal mode at 242 cm^{-1} of very low intensity and is not expected to aid much in the characterization of the Zn-ZIF-8 defects in the growing thin-films, as observed for our 20 LBL and 50 LBL samples. It is important to note here that the interpretation of normal modes under 400 cm^{-1} are subject to caution, as these normal modes are very sensitive to the environment, and we expect that our theoretical model in this range is least accurate as the force constant of shallow parts of a potential energy surface can significantly shift.

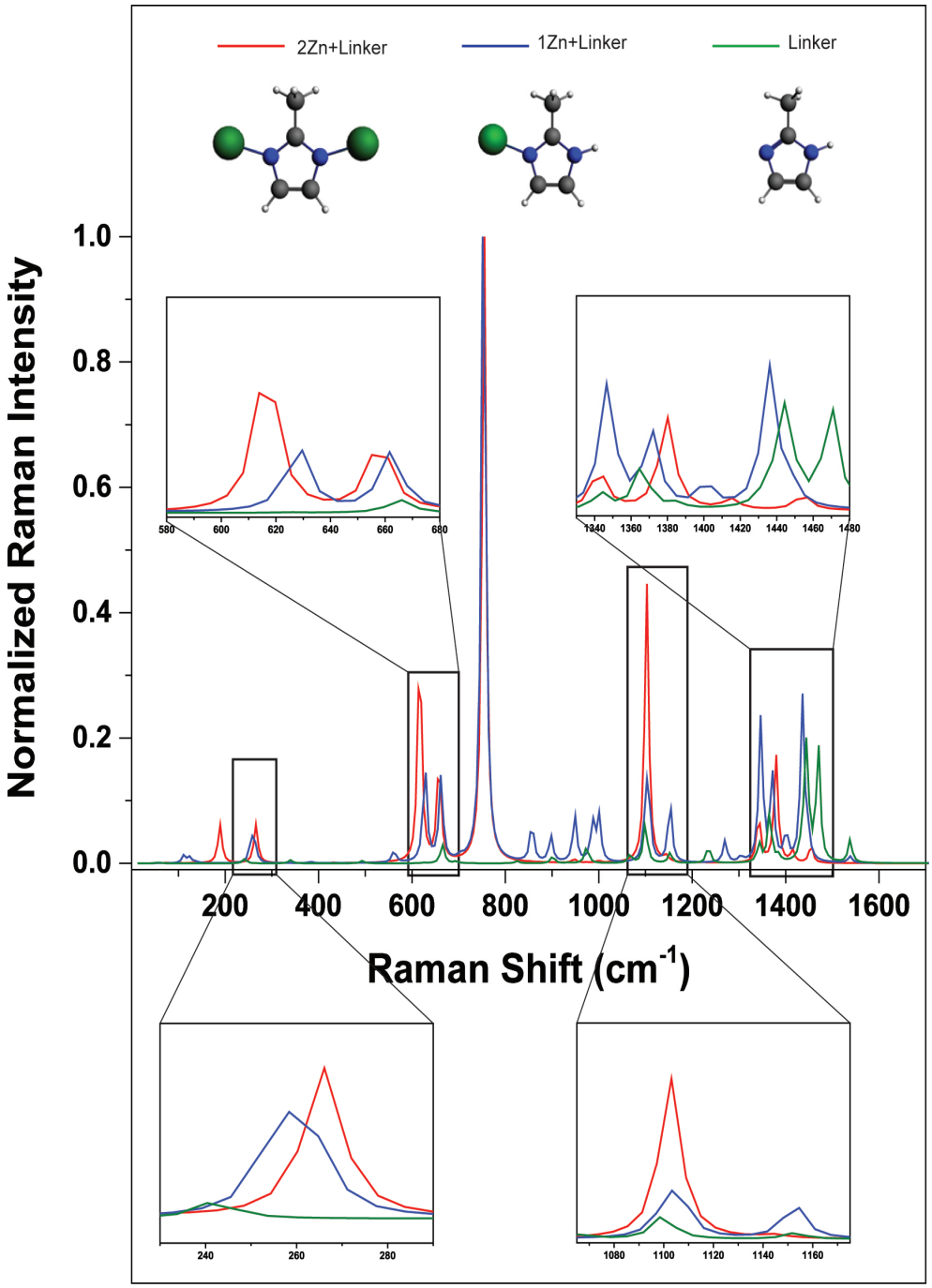

Figure 3.7. The normalized Raman spectra of the 2 Zn^{2+} + linker, 1 Zn^{2+} + linker, and only linker theoretical models as calculated with DFT. The important spectral regions between 230–290 cm^{-1}, 580–680 cm^{-1}, 1050–1180 cm^{-1}, and 1320–1480 cm^{-1} are also visualized in the insets, as they contain diagnostic fingerprints for defects sites. The spectra are broadened by a

Gaussian profile with half width of 10 cm^{-1} in order to reflect experimental Raman spectra.

Tble 3.3. Sideview of the normal modes of the inset between 580–680 cm^{-1} of the spectra of the 2 Zn + linker and 1 Zn + linker models.

Normal mode	Sideview	Normal mode	Sideview
2 Zn + linker 616 cm^{-1}	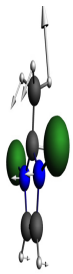	1 Zn + linker 628 cm^{-1}	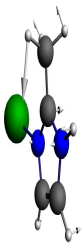
2 Zn + linker 658 cm^{-1}	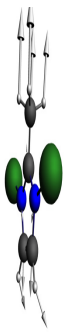	1 Zn + linker 662 cm^{-1}	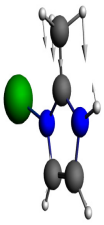

If we now take a look at the second inset (**spectral region B**, from 580–680 cm^{-1}) of Figure 3.7, we can see that there are two normal modes for the 2 Zn + linker and 1 Zn + linker models. The sideview and topview of these normal modes can be found in Table 3.3. It is worth noting that we can compare the normal modes in this spectral region between the models as they essentially describe the same vibrations. One can see that the normal mode of 658 cm^{-1} (2 Zn + linker) hardly shifts (blue shift: 4 cm^{-1}) if there is a metal cation missing. The reason for this is that this normal mode describes the elongation of the linker molecule perpendicular of the zinc atoms. These atoms, therefore, hardly contribute to the force constant of this vibration. Apparently, the extra N–H bend in the Zn + 1 linker model also does not change the energy of this vibration significantly. The other normal mode in this inset region, however, does shift significantly from 616 cm^{-1} for the 2 Zn + linker model to 628 cm^{-1} for the 1 Zn + linker model (blue shift: 12 cm^{-1}). This normal mode describes the out of plane (A" symmetry) bend of the imidazole linker. We attribute this large blue shift due to the loss of symmetry of the normal mode with just one zinc atom. The character of this normal mode becomes more asymmetric

and hence shifts towards higher energy. We therefore argue that especially the out of plane bending modes of the linker can be used to identify missing metal cations.

The third inset of Figure 3.7 shows a magnification of the 1050– 1180 cm^{-1} region (**spectral region C**). We can identify three normal modes in this region for all of the models, but the location and the nature of the normal modes are not identical. In Table 3.4 the topview of these normal modes are visualized. Two out of three normal modes are the same for the different models, but they are shifted in energy/ order. The normal mode that describes the C–H symmetric in-plane bending of the imidazole linker does not shift significantly in position (1103 cm^{-1} for 2 Zn + linker, 1106 cm^{-1} for the 1 Zn + linker, and 1100 cm^{-1} for the only linker model). On the other hand, the in-plane C–H bending mode (1141 cm^{-1} for the 2 Zn + linker model) does shift significantly for other two models, where the imidazole linker is protonated. This is largely caused by the contribution of the N–H bend to the normal mode in these models. Unfortunately, at this time, we cannot explain the large difference of this normal modes between the 1 Zn + linker model (1098 cm^{-1}) and only linker model (1067 cm^{-1}). Due to the significant shift of these normal modes with the absence of 1 (or more) zinc atoms, this normal mode seems ideal to identify defects in the Zn-ZIF-8 thin-films, but as can be seen in the inset in Figure 3.7 the Raman intensity of this normal mode is not very intense. Moreover, because of the (partial) overlap with the more intense other C–H bending mode, we do not expect large differences in the overall Raman spectra caused by this normal mode. The last normal mode in this region might be able to identify a missing metal cation. The nature of this last normal mode is different for the 2 Zn + linker model compared to the other models. Although, the position is only shifted slightly (1145 vs. 1153 cm^{-1}), due to the different nature of the normal mode, the resulting difference in intensity could maybe be used to identify structural defects.

The fourth inset of Figure 3.7 shows a magnification of the 1320–1480 cm^{-1} region (**spectral region D**). If we have a closer look at this region, we can see that they are quite complex. This region can most definitely be used to characterize defects in growing Zn-ZIF-8 thin-films, but the exact elucidation of the shifts in the normal modes is quite difficult. The 2 Zn + linker and only linker model systems have both 6 normal modes in this region, whereas the 1 Zn + linker model system have 5 normal modes in this region. The top view of these normal modes can be found in Table 3.5. The first thing to note from the normal modes in Table 3.5 is that all normal modes have a contribution of the methyl group of the imidazole linker. Moreover, the coupling between the contribution of the methyl group and the contribution of the other C–H bends of the linker is quite complex, and therefore, direct comparison between the normal modes of the different model systems is not

(always) possible. If there is a missing linker we expect on the basis of our calculated Raman spectra that there is a shift in intensity of the normal mode of 1346 cm^{-1} (for the 1 Zn + linker). This normal mode becomes more intense than the normal mode of 1371 cm^{-1}, whereas for the 2 Zn + linker system the normal mode at 1380 cm^{-1} remains more intense than the combination of the normal modes of 1342 cm^{-1} and 1353 cm^{-1}. Also the normal mode at 1436 cm^{-1} is really intense for the 1 Zn + linker model system, whereas the 2 Zn + linker model system has no intense normal modes between 1400 and 1480 cm^{-1}. Finally the only linker model system has two intense normal modes at 1445 and 1470 cm^{-1}. Especially the peak arising at 1470 cm^{-1} can be used to determine if there are floating linkers in the Zn-ZIF-8 thin-film.

Table 3.4. Topview of the normal modes of the inset between 1050–1180 cm^{-1} (spectral region C) of the vibrational spectra of the 2 Zn^{2+} + linker, 1 Zn^{2+} + linker, and only linker theoretical models.

Normal mode	Topview	Normal mode	Topview	Normal mode	Topview
2 Zn + linker 1103 cm^{-1}	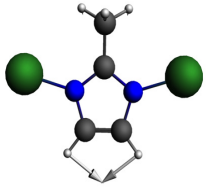	1 Zn + linker 1098 cm^{-1}	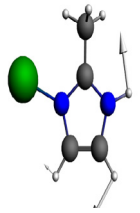	Only linker 1067 cm^{-1}	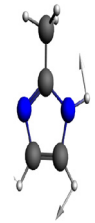
2 Zn + linker 1141 cm^{-1}	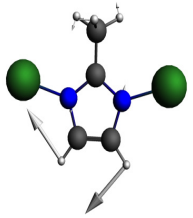	1 Zn + linker 1106 cm^{-1}	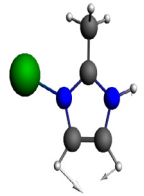	Only linker 1100 cm^{-1}	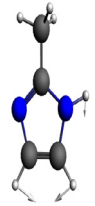
2 Zn + linker 1145 cm^{-1}	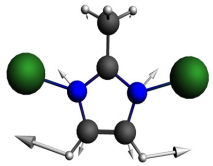	1 Zn + linker 1153 cm^{-1}	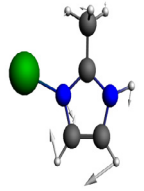	Only linker 1153 cm^{-1}	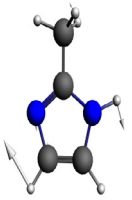

Table 3.5. Topview of the normal modes of the inset between 1320–1480 cm^{-1} (spectral region D) of the vibrational spectra of the 2 Zn^{2+} + linker, 1 Zn^{2+} + linker, and only linker theoretical models.

Normal mode	Topview	Normal mode	Topview	Normal mode	Topview
2 Zn + linker 1342 cm^{-1}	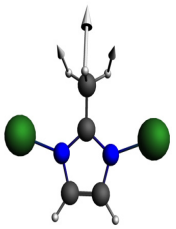	1 Zn + linker 1346 cm^{-1}	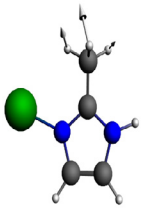	Only linker 1343 cm^{-1}	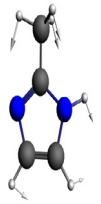
2 Zn + linker 1353 cm^{-1}	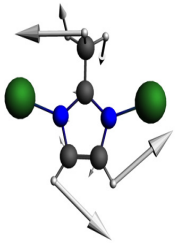	1 Zn + linker 1371 cm^{-1}	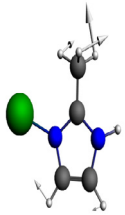	Only linker 1366 cm^{-1}	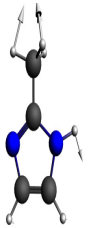
2 Zn + linker 1380 cm^{-1}	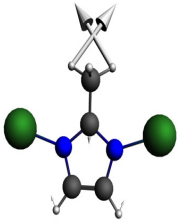	1 Zn + linker 1401 cm^{-1}	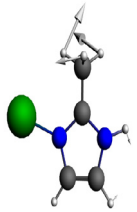	Only linker 1385 cm^{-1}	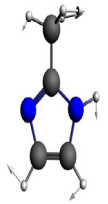

2 Zn + linker 1410 cm^{-1}		1 Zn + linker 1436 cm^{-1}		Only linker 1436 cm^{-1}	
2 Zn + linker 1415 cm^{-1}		1 Zn + linker 1448 cm^{-1}		Only linker 1445 cm^{-1}	
2 Zn + linker 1454 cm^{-1}				Only linker 1470 cm^{-1}	

3.3.3. Spectroscopic Fingerprinting of Chemical Heterogeneities in SURZIF-8

Having now a more in-depth insight in the vibrational fingerprints of the different Zn^{2+} and 2-methylimidazole coordination environment combinations we are in the position to turn back to the experimentally measured Raman spectra, as reported in Figures 3.4 c & d and 3.5 c & d, for the spectral regions 100-950 cm^{-1} and 800-1550 cm^{-1} and 20 and 50 LBL cycle samples, respectively.

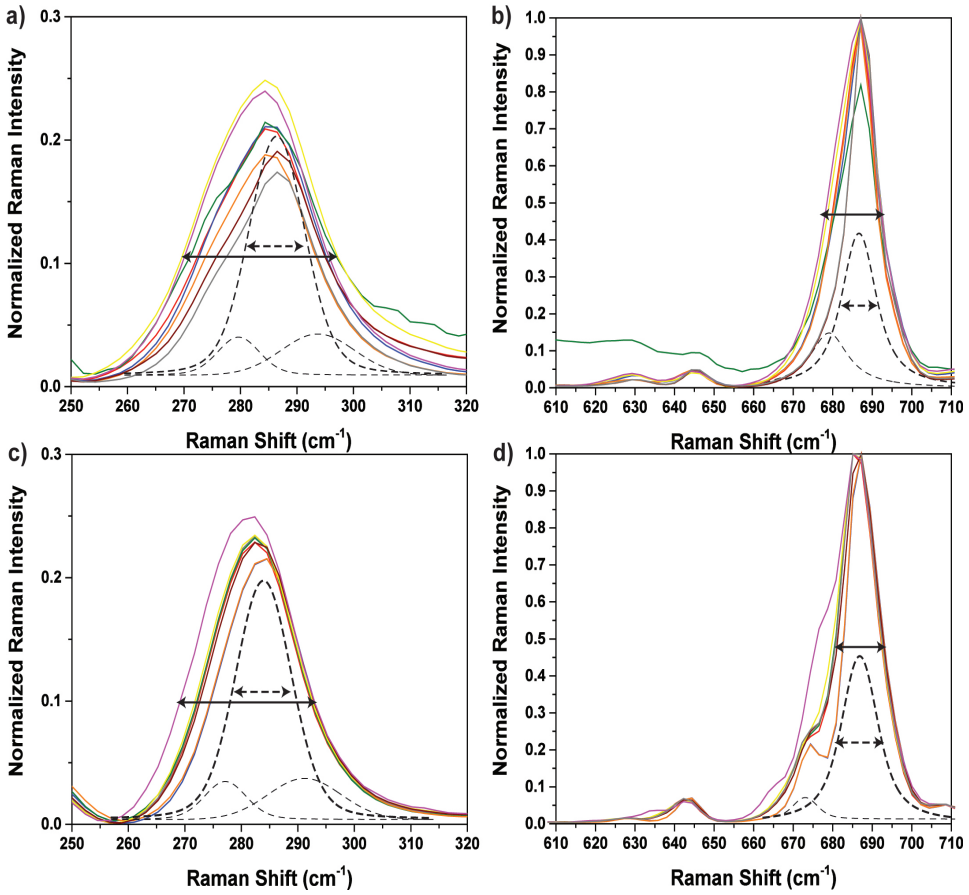

Figure 3.8. Comparison of the zoomed-in Raman bands (Figure 3.4.c&d) belonging to the resulting clusters from the EM for GMM PCA clustering analysis for 20 **(a&b)** and 50 **(c&d)** LBL cycle thin-film located at ~ 284 and ~ 686 cm^{-1}. Voigt function fitting of the Raman bands is provided with dashed lines.

The detailed investigation and comparison of the first spectral region of 250-320 cm^{-1} for the 20 and 50 LBL cycle samples are provided in Figure 3.8.a and 3.8.c,

respectively, and allows now to use the insights gathered from the discussions of **spectral region A** of Figure 3.7. The vibrational band located at ~ 284 cm^{-1} was assigned as ring deformation in accordance with the DFT calculations. Individual inspection of the spectra of each clusters in the 20 LBL cycle sample indicate that spectra of yellow, magenta and olive clusters undergo a higher red shift and band broadening than the other clusters and these clusters form the lower part of the Raman map, whereas the other clusters gray, brown, orange and red form the upper part of the phase boundary. Another observation is the presence of blue clusters in both upper and lower regions and it is also populated around the phase boundary acting as an intermediate in the Raman map. Figure 3.8.c shows a presence of a red shift and a band broadening as well however, these variations are minor and result in a more homogeneous inter-grown nature of the sample as shown in Figure 3.4.b. A higher band broadening, spectral shift and as well as an appearance of a weak shoulder is visible in particular in the spectra of 20 LBL cycle sample when compared to its 50 LBL cycle analogue ZIF-8 thin-film. The spectral red shift was found in the order of ~ 5 cm^{-1} and the band broadening was calculated in terms of FWHM and it is found as in the range of ~ 11-17 cm^{-1} for 20 LBL cycle sample. In the case of 50 LBL cycle sample, the red shift is calculated as ~ 2 cm^{-1} and the FWHM values vary in the order of ~ 6-10 cm^{-1}. Furthermore, the band maxima for the clusters belonging to the 50 LBL cycle sample are more red-shifted. These spectral observations are all in line for a more ordered Zn-ZIF-8 structure, as well as the presence of less defect sites in comparison with the 20 LBL cycle sample.

Comparison of this spectral fitting with the spectral data obtained through computational simulation indicates that the vibrational modes arising from a missing linker together with one Zn^{2+} undergo a huge band broadening with an appearance of a shoulder as well as a spectral red shift compared to the vibrational mode containing one linker and two Zn^{2+} ions. These results suggest that the clusters forming the lower region of the Raman map shown in Figure 3.4.a have the defects arising from the absence of one linker resulting in a loss of symmetry of the normal mode and hence, resulting in a band broadening. On the other hand, the clusters forming the upper layer of the phase boundary in Figure 3.4.a shows a relatively lower band broadening compared to the lower part of the Raman map as mentioned previously and have similarities with the clusters forming the 50 LBL cycle sample when the individual Raman intensity band areas were calculated and plotted, indicating a higher degree of symmetry, that is, the vibrational mode is arising from the presence of two zinc cations are bonded to linker.

The detailed investigation and comparison of the spectral region of 610-710 cm^{-1} for the 20 and 50 LBL cycle samples are provided in Figure 3.8.b and 3.8.d, respectively,

and allows now to use the insights gathered from the discussions of **spectral region B** of Figure 3.7. The vibrational band located at ~ 686 cm^{-1} was assigned as C-H bending-ring deformation in accordance with the DFT calculations as provided in Table 3.3. The individual analysis of the spectra of the clusters regarding the band located at ~ 686 cm^{-1} for 20 LBL cycle sample demonstrates similarities with the band located at ~ 284 cm^{-1} in terms of the distribution of the clusters throughout the upper and lower parts of the phase boundary observed in Figure 3.4. To illustrate, the spectra of magenta, yellow and green clusters are exposed to the highest red shift and band broadening and these regions form the lower part of the observed phase boundary. On the other hand, the striking observation is that the appearance of a shoulder in the case of 50 LBL cycle sample at a lower wavenumber with a maxima at ~ 675 cm^{-1} for the band located at ~ 686 cm^{-1}. Spectra of magenta and orange differs most with the spectra of the rest of the clusters as the spectra of magenta has a less defined however, higher in intensity shoulder, whereas the spectra of the orange cluster undergoes a least band broadening and possesses a well-defined shoulder.

The comparison of the spectra of individual clusters of 20 and 50 LBL cycle samples reveals a similar order of band broadening as well as a spectral red shift. The calculated FWHM values regarding the band located at ~ 686 cm^{-1} varies in the range of ~ 6-10 cm^{-1} for both samples and the spectral red shift was found in the order of ~ 2 and ~ 1 cm^{-1} for 20 and 50 LBL cycle samples, respectively. The band maxima of the ~ 686 cm^{-1} band was found to be very similar for both samples. Comparison of the experimental results with the spectra obtained through DFT calculations indicate that the vibrational mode arising from a missing zinc cation lack the presence of a shoulder and the band maxima is located at higher wavenumber than the vibrational mode of the two zinc cations and linker. These results suggest that the presence of a shoulder at ~ 675 cm^{-1} in the spectra of the clusters of 50 LBL cycle sample can be explained by the presence of two zinc cations and linker, whereas the absence of this shoulder in the spectra of 20 LBL cycle implies that there is at least a fraction of the sample which is missing a missing zinc cation hence a loss of symmetry in the overall thin-film structure.

The detailed investigation and comparison of the spectral region of 1075-1225 cm^{-1} for the 20 and 50 LBL cycle samples are provided in Figure 3.9.a and 3.9.c, respectively, and allows now to use the insights gathered from the discussions of **spectral region C** of Figure 3.7. The vibrational bands located at ~ 1144 and ~ 1180 cm^{-1} were assigned as C-H bending and ring deformation in accordance with the DFT calculations, as provided in Table 3.4. Detailed investigation of the individual spectra of each clusters for the 20 LBL cycle sample shows that the Raman band

located at ~ 1144 cm^{-1} undergoes a change in terms of band broadening and an appearance of a new shoulder-like band located at ~ 1135 cm^{-1}, as given in Figure 3.9.a. The spectra of the red, yellow, orange and grey clusters have the highest band broadening and the appearance of a new Raman band is clearly visible at higher intensities. These clusters differ most with the rest of the clusters and form the lower part of the phase boundary where grey cluster acts as an intermediate having a population throughout the phase boundary as given in Figure 3.5.a. The analysis of the Raman band located at ~ 1144 cm^{-1} was also performed for 50 LBL cycle sample. The appearance of the shoulder becomes clearly visible at ~ 1135 cm^{-1} at relatively lower intensities. The spectra of red, magenta and yellow exhibit differences with the spectra of the rest of the clusters as the shoulder belonging to the red cluster has the highest Raman band intensities, whereas the intensity of the well-defined shoulder appearing in the spectra of magenta and yellow have lower intensities when compared to the spectra of red.

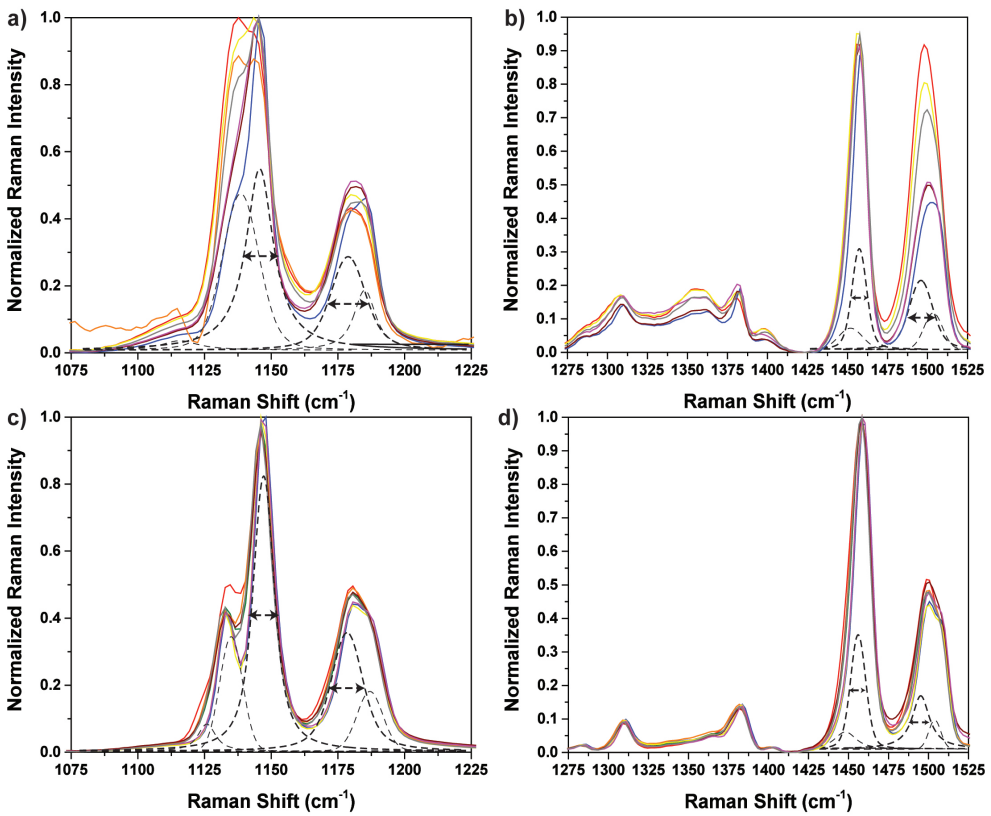

Figure 3.9. Comparison of the zoomed-in Raman bands (Figure 3.5.c&d) belonging to the resulting clusters from the EM for GMM PCA clustering analysis for 20 **(a&b)** and 50 **(c&d)** LBL cycle thin-film located at ~ 1144, ~ 1180, ~1456 and ~ 1498 cm^{-1}. Voigt function fitting

of Raman bands is provided with dashed lines.

The comparison of the 20 and 50 LBL cycle sample concerning the aforementioned band indicates that the band broadening for ~ 1144 cm^{-1} vibrational band is found to be almost two folds higher for 20 LBL cycle sample (~ 8-21.5 cm^{-1}) when compared to the 50 LBL cycle sample (~ 8.6-10 cm^{-1}). The average spectral Raman red shift was calculated to be in the order of ~ 1.5 cm^{-1} for both samples, while the Raman band maxima are very similar for both samples. In order to explain these differences observed, the DFT calculations can provide further insights. The vibrational mode arising from the missing zinc cation possessing low degree of symmetry exhibits a shoulder at higher intensities in contrast to the vibrational mode simulated in the case of two zin cations and a linker. The appearance of a shoulder at higher intensities is the observation that we have in the case of 20 LBL cycle sample in particular in the spectra of the clusters (red, yellow, orange and grey) forming the lower part of the Raman map (Figure 3.5.a). Furthermore, in the theoretical spectra, this band is broader (higher FWHM) and this is the case also in the 20 LBL cycle sample. However, this shoulder is also visible in the 50 LBL cycle sample, but the intensity of the shoulder is drastically reduced and indicating a relatively higher degree of symmetry. On the other hand, the Raman band maxima regarding the band located at ~ 1146 cm^{-1} in the theoretical Raman spectra is located at higher wavenumber in the case of a missing zinc cation.

Furthermore, the second Raman band located at ~ 1180 cm^{-1} in **spectral region C** of the Raman spectra was also investigated in detail. Figure 3.9.a and 3.9.b illustrate the individual spectra of each cluster for the aforementioned band for 20 and 50 LBL cycle thin-films, respectively. The comparison of the spectra of individual clusters in 20 LBL cycle sample shows differences in terms of band broadening, spectral shift and an appearance of a shoulder in particular visible in the blue cluster. The spectra of the yellow, red, orange and grey clusters have relatively lower intensity when compared with the other clusters. In contrast, for the 50 LBL cycle thin-film this band is very similar, and overall the 1180 cm^{-1} does not provide much discriminative power to identify defects sites in the different regions of interest and between the two samples.

The last and fourth spectral Raman region of interest covering the region between 1275 and 1525 cm^{-1} was also investigated in detail, as shown in Figure 3.9.c and 3.9.d for 20 and 50 LBL cycle thin films, respectively. This region can now be discussed together with the theoretical insights provided by DFT and as discussed for **spectral region D** of Figure 3.7. The vibrational bands located at ~ 1458 and ~ 1498 cm^{-1} are assigned as C-H bending and ring deformation (Table 3.5). The individual spectra

of each of the identified clusters were also analysed in detail and compared for the aforementioned Raman bands for both 20 and 50 LBL cycle thin-films. In the 20 LBL cycle sample, the Raman band located at ~ 1458 cm^{-1} exhibits differences throughout the spectra of clusters in terms of band broadening and spectral shift in particularly and the bands that are broadened most belong to the spectra of red, yellow, and grey clusters. This is the common observation for the other bands analysed as well, as these clusters form the lower part of the Raman map provided in Figure 3.7.c. On the other hand, band broadening is also observed in the case of 50 LBL cycle sample for the ~ 1458 cm^{-1} band. However, the resulting Raman map of all clusters as illustrated in Figure 3.7.d shows the inter-grown nature of the film under study. The comparison of the band broadening and spectral shift regarding the ~ 1458 cm^{-1} vibrational band between 20 and 50 LBL cycle samples demonstrates that the average calculated FWHM is found to be higher in 50 LBL cycle (~ 12-14 cm^{-1}) sample than 20 LBL cycle (~ 9-12 cm^{-1}) sample, while the Raman band maxima are very similar for both samples. Furthermore, the average spectral shift was found to be in the order of ~ 2 cm^{-1} for both samples.

The second vibrational band of interest in the spectral region of 1275 - 1525 cm^{-1} is the band located at ~1498 cm^{-1} and a detailed data analysis was also executed. In the Raman spectra of 20 LBL cycle, the comparison of the individual spectra of each clusters show big differences in terms of band broadening, spectral shift, and as well as intensity differences. The striking observation is the decrease in the band intensity as going from red, yellow and grey clusters to the rest of the spectra of the clusters. These clusters, which possess a higher intensity are again responsible for the appearance of the observed phase-boundary, which form the lower part of the phase-boundary, as shown in Figure 3.5.c. Analysis of the same band for 50 LBL cycle displays also differences in terms of band broadening and spectral shifts, but clearly this band is much less intense as in the case of the 50 LBL cycle sample. An appearance of a shoulder at ~ 1508 cm^{-1} is also observed. The calculated FWHM for the band located at ~ 1498 cm^{-1} varies in the range of ~ 17-21 cm^{-1} and ~ 14-19 cm^{-1} and the calculated spectral shift is found to be in the order of ~ 3 and ~ 2.5 cm^{-1} for 20 and 50 LBL cycle samples, respectively. The Raman band maxima are located at very similar in the case of the 20 and 50 LBL cycle samples.

3.4 Conclusions

Two distinct Zn-ZIF-8 thin-films, obtained after respectively 20 and 50 layer-by-layer (LBL) cycles, have been prepared and subsequently characterized by Raman microscopy as well as by Atom Force Microscopy (AFM). A region of 100x100 μm^2 was defined and a detailed spectral and topographic mapping was performed in order to search for chemical heterogeneities in these two thin-film materials. Principal component analysis (PCA) of the Raman data acquired demonstrated the existence of a clear phase boundary for the 20 LBL cycle Zn-ZIF-8 material, whereas the 50 LBL cycle Zn-ZIF-8 material is chemically much more homogeneous in nature, although still full of chemical heterogeneities. The spectral differences observed between the different phases present were revealed through a detailed analysis of the Raman spectroscopy data. In order to assist the search for vibrational fingerprints of defects sites we have performed DFT calculations on three model systems, namely linker (i.e., 2-methylimidazole) coordinated with two Zn^{2+}-ions, a protonated linker coordinated to one Zn^{2+}, and an isolated protonated linker (with no Zn^{2+}-ions coordinating to the linker). This theoretical approach enabled the calculation of the molecular vibrations of the fingerprint spectral features of Zn-ZIF-8 thin-films, undergoing intensity changes and/or band splitting/shifts.

Based on this detailed comparison of both the experimental and theoretical Raman spectra in four distinct spectral regions (A-D) for the two Zn-ZIF-8 thin-films under study it was found that:

- Spectral region A (230-290 cm^{-1}) provides information on the overall structural quality of the thin-film *via* the 284 cm^{-1} Raman band. When this band becomes broad and red-shifted the region becomes more defect-rich.

- Spectral region B (580-680 cm^{-1}) provides information on the overall structural quality of the thin-film *via* the relative intensity ratio of the 675 to 686 cm^{-1} Raman bands. A relative intense 675 cm^{-1} Raman band is indicative of a defect-poor structure.

- Spectral region C (1065-1175 cm^{-1}) provides information on the overall structural quality of the thin-film *via* the 1180 cm^{-1} band, as this band is characteristic for the presence of a linker with only one Zn^{2+} ion. As this band is also present in a well-formed thin-film it indicates that even for such material there are some Zn^{2+} ions missing in the ZIF-8 structure.

- Spectral region C (1065-1175 cm^{-1}) provides additional information on the overall structural quality of the thin-film *via* the relative intensity ratio of

the 1135 to 1144 cm^{-1} Raman bands. A relative intense 1135 cm^{-1} Raman band is indicative of a defect-rich structure.

- Spectral region D (1320-1480 cm^{-1}) provides direct information on the presence of free linkers via the presence of the 1498 cm^{-1} Raman band. Clearly, sample regions, which are defect-rich have a high intensity of this Raman band, although our data also suggest that even for more defect-free regions there are still some free linkers present. The relative ratio of the 1458 to 1498 cm^{-1} Raman bands turns out to be a quality indicator for the structural integrity of the Zn-ZIF-8 thin-film. A relative intense 1458 cm^{-1} Raman band is indicative of a defect-poor structure.

Summarizing, this work provides Raman spectroscopy fingerprints for evaluating the overall quality and presence of different defect sites within SURZIF-8 thin-films, although the procedure developed should be more generally applicable to other ZIF and MOF materials. The comparison between the AFM and Raman maps also indicates that AFM does not allow to make any judgement on the chemical uniformity of the thin-film samples, and also turned out not to be sensitive enough to detect the phase-boundary observed in one of our SURZIF-8 thin-film under study.

3.5. References

[1] P. St. Petkov, G. N. Vayssilov, J. Liu, O. Shekhah, Y. Wang, C. Wöll, T. Heine, *ChemPhysChem* **2012**, *13*, 2025–2029.

[2] H. B. Tanh Jeazet, C. Staudt, C. Janiak, *Dalt. Trans.* **2012**, *41*, 14003–14027.

[3] G. Férey, *Chem. Soc. Rev.* **2008**, *37*, 191–214.

[4] Z. Öztürk, J. P. Hofmann, M. Lutz, M. Mazaj, N. Z. Logar, B. M. Weckhuysen, *Eur. J. Inorg. Chem.* **2015**, *2015*, 1625–1630.

[5] S. Horike, M. Dincă, K. Tamaki, J. R. Long, *J. Am. Chem. Soc.* **2008**, *130*, 5854–5855.

[6] L. T. L. Nguyen, K. K. A. Le, H. X. Truong, N. T. S. Phan, *Catal. Sci. Technol.* **2012**, *2*, 521–528.

[7] M. Ranocchiari, J. A. van Bokhoven, *Phys. Chem. Chem. Phys.* **2011**, *13*, 6388–6396.

[8] S. Keskin, K. Seda, *Ind. Eng. Chem. Res.* **2011**, *50*, 1799–1812.

[9] K. M. L. Taylor-Pashow, J. Della Rocca, Z. Xie, S. Tran, W. Lin, *J. Am. Chem. Soc.* **2009**, *131*, 14261–14263.

[10] L. Zhang, Y. Jian, J. Wang, C. He, X. Li, T. Liu, C. Duan, *Dalt. Trans.* **2012**, *41*, 10153–10155.

[11] L. He, Y. Liu, J. Liu, Y. Xiong, J. Zheng, Y. Liu, Z. Tang, *Angew. Chem.* **2013**, *52*, 3741–3745.

[12] J. A. Botas, G. Calleja, M. Sánchez-Sánchez, M. G. Orcajo, *Langmuir* **2010**, *26*, 5300–5303.

[13] G. Kumari, K. Jayaramulu, T. K. Maji, C. Narayana, *J. Phys. Chem. A* **2013**, *117*, 11006–11012.

[14] S. Couck, E. Gobechiya, P. Serra-Crespo, A. Martinez Joaristi, E. Stavitski, J. Gascon, F. Kapteijn, G. V Baron, J. F. M. Denayer, *ChemSusChem* **2012**, *5*, 740–750.

[15] J. Yao, H. Wang, *Chem. Soc. Rev.* **2014**, *43*, 4470–4493.

[16] K. S. Park, Z. Ni, A. P. Cote, J. Y. Choi, R. Huang, F. J. Uribe-Romo, H. K. Chae, M. O'Keeffe, O. M. Yaghi, *Proc. Natl. Acad. Sci.* **2006**, *103*, 10186–10191.

[17] A. Phan, C. J. Doonan, F. J. Uribe-Romo, C. B. Knobler, M. O'Keeffe, O. M. Yaghi, *Acc. Chem. Res.* **2010**, *43*, 58–67.

[18] E. L. Bustamante, J. L. Fernández, J. M. Zamaro, *J. Colloid Interface Sci.* **2014**, *424*, 37–43.

[19] O. Shekhah, R. Swaidan, Y. Belmabkhout, M. du Plessis, T. Jacobs, L. J. Barbour, I. Pinnau, M. Eddaoudi, *Chem. Commun.* **2014**, *50*, 2089.

[20] Y. Hu, H. Kazemian, S. Rohani, Y. Huang, Y. Song, *Chem. Commun.* **2011**, *47*, 12694–12696.

[21] A. Huang, Q. Liu, N. Wang, J. Caro, *J. Mater. Chem. A* **2014**, *2*, 8246.

[22] J. Cookney, W. Ogieglo, P. Hrabanek, I. Vankelecom, V. Fila, N. Benes, *Chem. Commun.* **2014**, *50*, 11698–11700.

[23] Y. Hu, H. Kazemian, S. Rohani, Y. Huang, Y. Song, *Chem. Commun.* **2011**, *47*, 12694–12696.

[24] S. R. Venna, J. B. Jasinski, M. A. Carreon, *J. Am. Chem. Soc.* **2010**, *132*, 18030–18033.

[25] P. Y. Moh, P. Cubillas, M. W. Anderson, M. P. Attfield, *J. Am. Chem. Soc.* **2011**, *133*, 13304–13307.

[26] O. Shekhah, J. Liu, R. A. Fischer, C. Wöll, *Chem. Soc. Rev.* **2011**, *40*, 1081–1106.

[27] A. B?tard, R. A. Fischer, *Chem. Rev.* **2012**, *112*, 1055–1083.

[28] D. Zacher, O. Shekhah, C. Wöll, R. A. Fischer, *Chem. Soc. Rev.* **2009**, *38*, 1418–1429.

[29] O. Shekhah, J. Liu, R. A. Fischer, C. W?ll, *Chem. Soc. Rev.* **2011**, *40*, 1081–1106.

[30] H. Guo, Y. Zhu, S. Qiu, J. A. Lercher, H. Zhang, *Adv. Mater.* **2010**, *22*, 4190–4192.

[31] E. Biemmi, A. Darga, N. Stock, T. Bein, *Microporous Mesoporous Mater.* **2008**, *114*, 380–386.

[32] R. Ameloot, L. Stappers, J. Fransaer, L. Alaerts, B. F. Sels, D. E. De Vos, *Chem. Mater.* **2009**, *21*, 2580–2582.

[33] S. Aguado, J. Canivet, D. Farrusseng, *Chem. Commun.* **2010**, *46*, 7999–8001.

[34] E. V. Ramos-Fernandez, M. Garcia-Domingos, J. Juan-Alcañiz, J. Gascon, F. Kapteijn, *Appl. Catal. A Gen.* **2011**, *391*, 261–267.

[35] Y. Yoo, Z. Lai, H.-K. Jeong, *Microporous Mesoporous Mater.* **2009**, *123*, 100–106.

[36] V. V. Guerrero, Y. Yoo, M. C. McCarthy, H.-K. Jeong, *J. Mater. Chem.* **2010**, *20*, 3938–3943.

[37] A. Bétard, H. Bux, S. Henke, D. Zacher, J. Caro, R. A. Fischer, *Microporous Mesoporous Mater.* **2012**, *150*, 76–82.

[38] D. Zacher, K. Yusenko, A. Bétard, O. Shekhah, T. de los Arcos, M. Krasnopolski, J. Winter, A. Terfort, C. Wöll, R. A. Fischer, *Chem. - A Eur. J.* **2011**, *17*, 1448–1455.

[39] R. Bro, A. K. Smilde, *Anal. Methods* **2014**, *6*, 2812–2831.

[40] J. E. Jackson, *A User's Guide to Principal Components*, Wiley-Interscience, Hoboken, NJ, **2003**.

[41] I. T. Joliffe, *Principal Component Analysis*, Springer, New York, **2002**.

[42] J. B. MacQueen, *In 5th Berkeley Symposium on Mathematical Statistics and Probability*, University Of California Press, Berkeley, CA, **1967**.

[43] R. A. Johnson, D. W. Wichern, *Applied Multivariate Statistical Analysis*, Pearson, Upper Saddle River, NJ, **2002**.

[44] G. te Velde, F. M. Bickelhaupt, E. J. Baerends, C. Fonseca Guerra, S. J. a. van Gisbergen, J. G. Snijders, T. Ziegler, *J. Comput. Chem.* **2001**, *22*, 931–967.

[45] B. K. Perdew J. P, M. Ernzerhof, *Phys. Rev. Lett.* **1996**, *77*, 3865–3868.

[46] E. Van Lenthe, E. J. Baerends, *J. Comput. Chem.* **2003**, *24*, 1142–1156.

[47] A. Bérces, R. M. Dickson, L. Fan, H. Jacobsen, D. Swerhone, T. Ziegler, *Comput. Phys. Commun.*

1997, *100*, 247–262.

[48] H. Jacobsen, A. Bérces, D. P. Swerhone, T. Ziegler, *Comput. Phys. Commun.* **1997**, *100*, 263–276.

[49] S. K. Wolff, *Int. J. Quantum Chem.* **2005**, *104*, 645–659.

[50] S. J. A. van Gisbergen, J. G. Snijders, E. J. Baerends, *Chem. Phys. Lett.* **1996**, *259*, 599–604.

[51] S. J. A. van Gisbergen, J. G. Snijders, E. J. Baerends, *Comput. Phys. Commun.* **1999**, *118*, 119–138.

[52] D.-Y. Kim, B. N. Joshi, J.-G. Lee, J.-H. Lee, J. S. Lee, Y. K. Hwang, J.-S. Chang, S. Al-Deyab, J.-C. Tan, S. S. Yoon, *Chem. Eng. J.* **2016**, *295*, 49–56.

[53] S. Tanaka, K. Fujita, Y. Miyake, M. Miyamoto, Y. Hasegawa, T. Makino, S. Van der Perre, T. Van Assche, G. V. Baron, J. F. M. Denayer, *J. Phys. Chem. C* **2015**, *119*, 28430–28439.

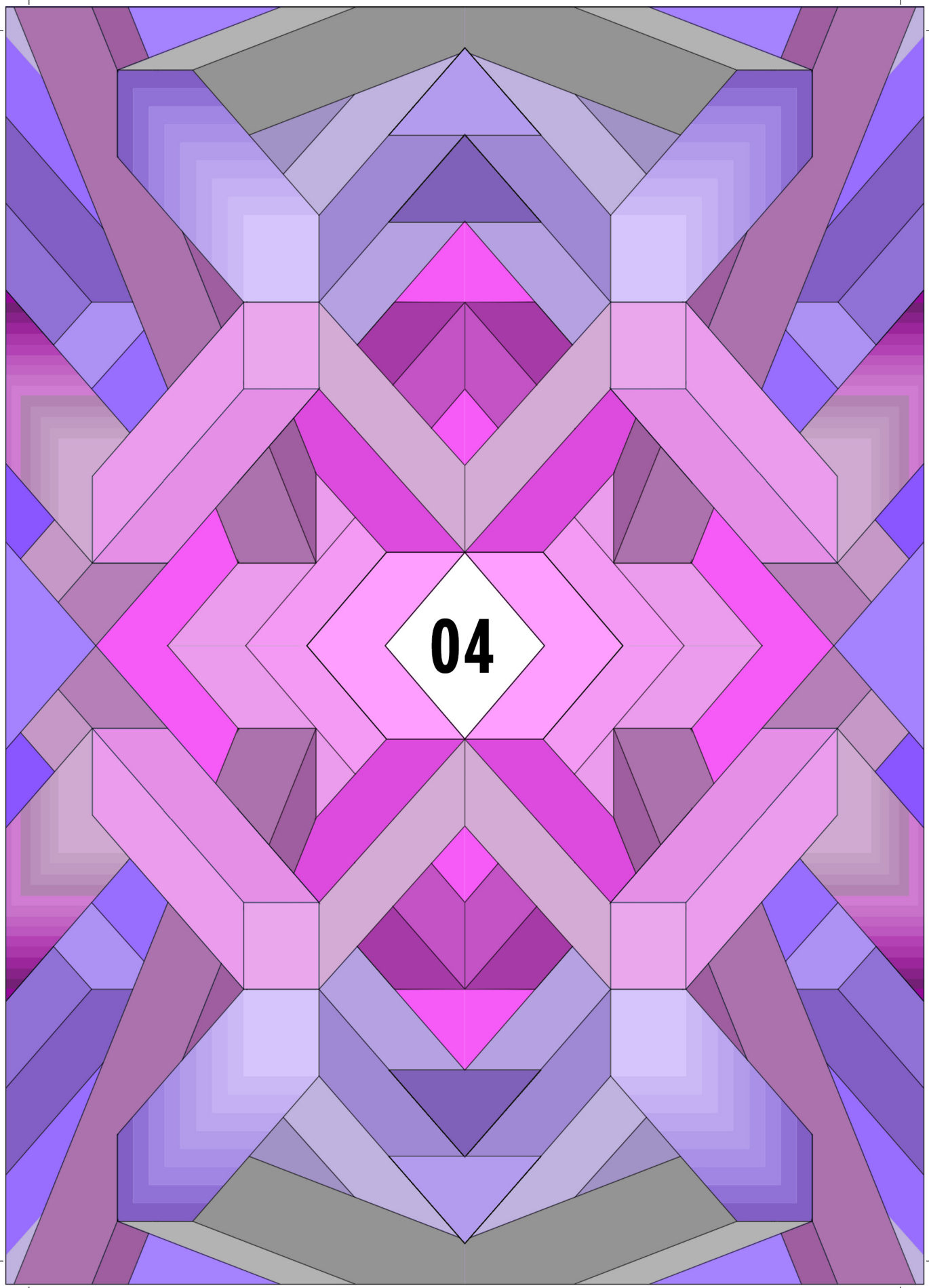
04

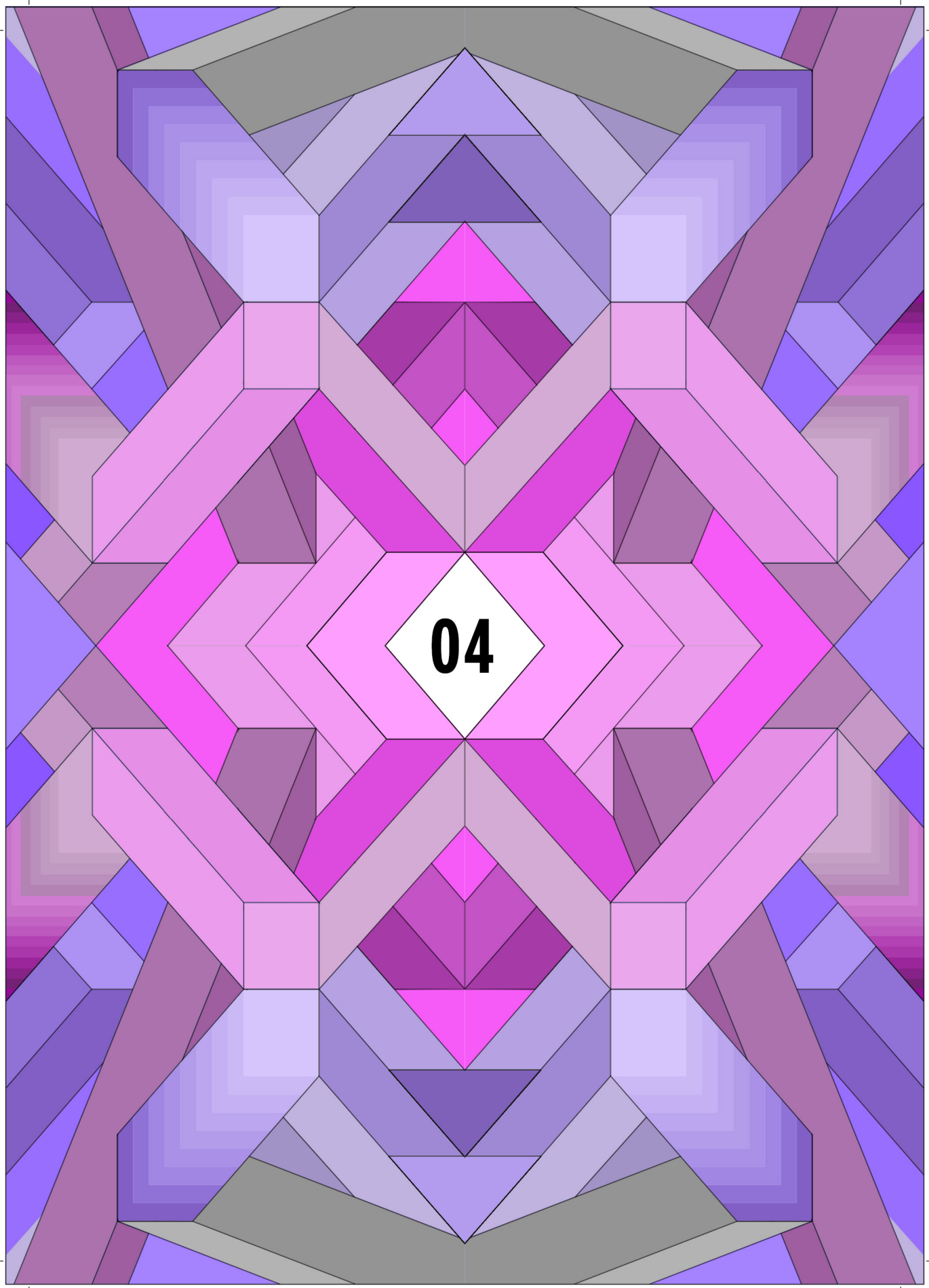
04

04

Decoding Nucleation and Growth of Zeolitic Imidazolate Framework Thin-Films with Atomic Force Microscopy and Vibrational Spectroscopy

Abstract

The synthesis of metal-organic framework (MOF) thin-films has garnered significant attention during the past decade. By better understanding the parameters governing the nucleation and growth of such thin-films, their properties can be rationally tuned, empowering their application as (reactive) membranes. Here, a combined AFM-vibrational spectroscopy research strategy is employed to detail the chemistries governing the nucleation and growth of zeolitic imidazolate framework (ZIF) thin-films, in particular isostructural Co-ZIF-67 and Zn-ZIF-8. First, a single step direct synthesis approach is used to interrogate the influence of different synthesis parameters –metal/linker ratio, temperature and metal type– on the thin-film nucleation and growth behaviour. While the metal/linker ratio has a pronounced effect on the thin-film nucleation rate, the temperature mainly influences the growth kinetics of nuclei forming the thin-film. In addition, the nucleation and growth of ZIF thin-films is shown to be highly dependent on the electronegativity of the metal type. Thin-film thickness control can be achieved by using a multistep synthesis strategy, implying repetitive application of single step deposition under identical synthesis conditions, for which a growth mechanism is proposed. This study provides insight into the influence of synthesis parameters on the ZIF thin-film properties, reaching tools at hand to rationally tune MOF thin-film properties.

This Chapter is based on the following publication: Z. Öztürk, M. Filez and B. M. Weckhuysen, Decoding Nucleation and Growth of Zeolitic Imidazolate Framework Thin-Films with Atomic Force Microscopy and Vibrational Spectroscopy, *Chem. Eur. J.* **2017**, *23*, 10915-10924.

4.1. Introduction

Metal-organic frameworks (MOFs) are microporous crystalline materials built-up from metal oxide clusters interconnected by organic linkers.[1–8] By varying the metal and linker type, the MOF functionalities and pore space can be rationally tuned towards their desired properties.[5,9–12] This compositional flexibility makes MOFs extremely versatile functional materials, allowing their application in various fields,[13–15] including gas sensing,[10] separation,[6,10,16–18] storage,[19,20] and (photo-) catalysis.[18,21–25] Zeolitic imidazolate frameworks (ZIFs) are a sub-class of MOFs in which divalent metal cations (e.g., Co^{2+}, Zn^{2+}, Cu^{2+} or Fe^{2+}) are tetrahedrally coordinated by a bridging imidazolate-type linkers.[26–31] In ZIFs, the resulting framework has a similar coordination geometry to those of microporous crystalline aluminosilicates, namely zeolites.[26,32–34] Owing to their resemblance to both zeolites and traditional MOFs, ZIFs combine the structural flexibility of MOFs with the thermal and chemical stability of zeolites[26,29], as recently demonstrated in the fields of gas storage,[35–37] sensing[38] and catalysis.[23,39,40] Amongst them, Zn-ZIF-8 is a quintessential model system of the ZIF family, being constructed through Zn^{2+} ions tetrahedrally coordinated by bridging 2-methylimidazolate linkers.[26,28,30,41–43] By using Co^{2+} instead of Zn^{2+} cations, isostructural Co-ZIF-67 is obtained, exposing an identical structure to Zn-ZIF-8, but with Co^{2+} in the Zn^{2+} lattice positions.[44–47]

Several studies report on the crystallization mechanisms of bulk ZIFs by using *in-situ* static light scattering (SLS),[29] transmission electron microscopy (TEM),[32,48] scanning electron microscopy (SEM),[28,49] X-ray diffraction (XRD),[28,32] small angle and wide angle X-ray scattering (SAXS/WAXS),[31] electrospray ionization mass spectrometry (ESI-MS),[50] and atomic force microscopy (AFM)[51,52]. However, for (reactive) membrane and gas sensors applications, conformal ZIF thin-films with highly controllable morphologies are required instead of bulk powders. Two thin-film deposition methods in particular have received much attention in the past years, being layer-by-layer synthesis and direct solvothermal synthesis. Layer-by-layer synthesis relies on the alternating exposure of metal and linker solutions to a SAM-terminated substrate. This method provides high thickness and orientational control, but is slow and economically not viable, except for specialty applications. In contrast, direct synthesis combines the metal and linker solutions in a single mixed solution, and offers rapid thin-film growth at the expense of morphological control.[4,8,11,53] However, fundamental improvement of the morphology of directly synthesized thin-film is still possible. This could potentially allow this industrially viable method to tailor thin-film properties at a comparable level relative to layer-by-layer grown films. Strong improvements, however, rely on the advent and application of advanced characterization tools, which can fill the knowledge gap to

achieve such thin-film design.

The nucleation and growth behaviour of ZIF thin-films, to the best of our knowledge, has not been studied before, and in particular the role of synthesis parameters have not been reported in a systematic way. In this Chapter, a combined AFM-vibrational spectroscopy research strategy is presented to investigate the chemistries governing the nucleation and growth of ZIF thin-films. In particular, single step deposition via direct synthesis method is utilized for the investigation of different synthesis parameters, namely metal/linker ratio, temperature and metal type. In addition, a multistep direct synthesis method is further employed for controlling the thickness of Co-ZIF-67 and Zn-ZIF-8 thin-films. Finally, a mechanism regarding the multistep thin-film growth mechanism is proposed.

4.2. Experimental

4.2.1. Synthesis of Bulk Zn-ZIF-8 and Co-ZIF-67

The synthesis of bulk Zn-ZIF-8 and Co-ZIF-67 have been reported previously and we have used these literature recipes.[29,32] In a typical synthesis, 0.3 g of $Zn(NO_3)_2 \cdot 6H_2O$ (Sigma-Aldrich, 99%) and 0.66 g of 2-methylimidazole (Sigma-Aldrich, 99%) were dissolved separately in 11.3 g of methanol (Acros, extra dry). The organic linker solution was transferred into the Zn-based solution and the corresponding mixture was stirred and let to react for 24 h. The solid ZIF-8 particles were collected from solution by centrifugation at 4000 rpm for 10 min and washed with methanol. After washing with methanol, the solution was centrifuged again and washed with methanol. The ZIF-8 material was dried at room temperature for 24 h and then further dried in an oven at 75°C overnight. For the synthesis of Co-ZIF-67, $Co(NO_3)_2 \cdot 6H_2O$ (Acros, 99%) was used as a precursor and the same procedure was followed as for the synthesis of Zn-ZIF-8.

4.2.2. Synthesis of Thin-films of Zn-ZIF-8 and Co-ZIF-67

The room temperature preparation of Zn-ZIF-8 and Co-ZIF-67 thin-films through direct synthesis method was described previously by Tu et al..[3] and adapted for this work. For the preparation of Zn-ZIF-8 thin-films, a methanolic (Acros, extra dry) solution of 90 mM $Zn(NO_3)_2 \cdot 6H_2O$ (Sigma-Aldrich, 99%) and a methanolic (Acros, extra dry) solution of 660 mM 2-methylimidazole (Sigma-Aldrich, 99%) were used in order to obtain a metal to linker ratio of 1/6.6. Gold-coated silicon wafers (60 nm Au particles sputtered on silicon wafer with a Ge adhesion layer) were used as substrates and were purchased from AMOLF (https://amolf.nl/). 4 mL of both metal and linker solutions were mixed in a glass vial and the substrate was immersed for

10 min vertically into the solution in order to avoid sedimentation. This process is called the deposition step. One, two and four deposition steps were applied in this work, where the intermediate washing steps with fresh methanol have been followed by a gentle drying by flowing N_2. For the preparation of Co-ZIF-67 thin-films, the same procedure was performed where $Co(NO_3)_2 \cdot 6H_2O$ (Acros, 99%) was used as the metal precursor. The reaction conditions and metal/linker ratios are further detailed in the result section where needed. Finally, an ice-bath and water-bath were used for maintaining 0°C and 40°C, respectively with a strict temperature control.

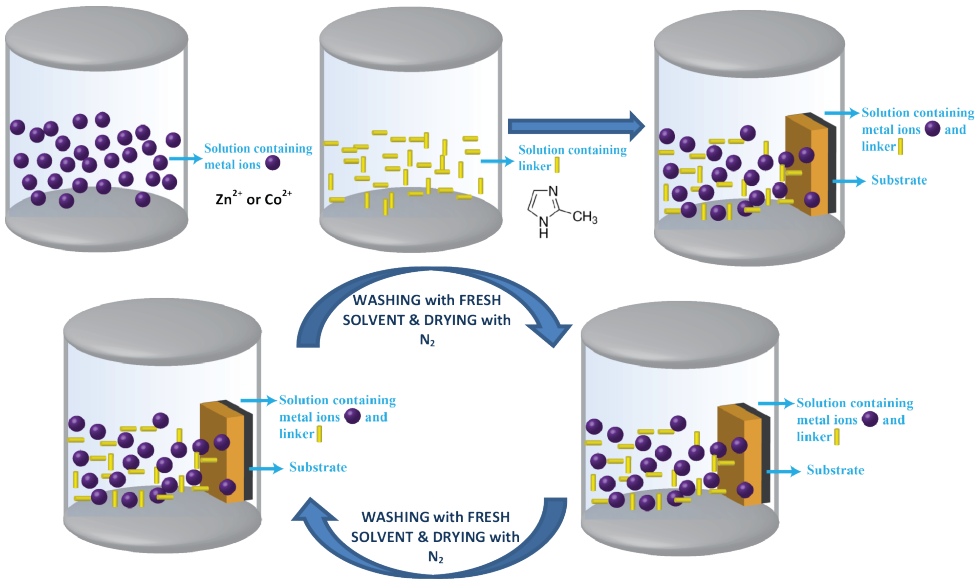

Figure 4.1. Illustration of the direct synthesis preparation approach for Zn-ZIF-8 and Co-ZIF-67 thin-films at room temperature

4.2.3. Characterization

X-ray diffraction (XRD) patterns of the as-synthesized materials were obtained using a CoKα radiation of a Bruker AXS D2 Phaser diffractometer. Atomic Force Microscopy (AFM) measurements were performed on a NT-MDT NTEGRA Spectra upright AFM unit. Olympus AC 160TS tips were used for all AFM measurements. AFM scans of 10x10 μm^2 in size were made with high resolution (i.e., 512x512 pt^2). The iTEM software was used for the particle size analysis performed on AFM micrographs. Focus Ion Beam Scanning Electron microscopy (FIB-SEM) measurements were executed with a Helius 600 FEI instrument with an acceleration voltage of 2 kV and working distance of 4 mm by using secondary electrons. A Gallium source

is used for Focus Ion beam (FIB) operating at 30 kV. Diffuse Reflectance Infrared Fourier Transform (DRIFT) spectroscopy experiments were carried out by using Praying Mantis™ Diffuse Reflection Accessory (Harrick) in a Perkin Elmer Frontier spectrometer equipped with DTGS detector. The spectra were collected in the region of 400-4000 cm^{-1} with a 4 cm^{-1} resolution and 64 scans. Raman spectroscopy measurements were performed with a Renishaw InVia micro-spectrometer making use of a 785 nm laser and the spectra were recorded in the spectral region of 100-3200 cm^{-1}.

4.3. Results and Discussion

4.3.1. Single Step Deposition

Three sets of experiments were carried out to study the impact of the (1) metal/linker ratio, (2) synthesis temperature and (3) metal cation on the nucleation and growth behaviour of Co-ZIF-67 thin-films prepared in MeOH. First, the influence of the metal/linker ratio on the resulting ZIF particle deposition –being the onset of thin-film formation– is studied by atomic force microscopy (AFM). Figure 4.2.a-c respectively shows three AFM topology maps (10 x 10 μm^2) of Co-ZIF-67 particles deposited on a Au coated substrate after 10 min at room temperature with metal/linker ratios of 1/3, 1/4, and 1/6. Visual inspection of the AFM micrographs clearly shows that the number of particles increases with decreasing metal/linker ratio. In order to quantify this observation, particle size histograms are obtained as shown in Figure 4.2.d. Based on these histograms, the number of particles increases from 66 to 239 per 100 μm^2 with decreasing metal/linker ratio from 1/3 to 1/6.6 (Figure 4.2.e), respectively. In addition, the particle size histograms show a significant average particle size increase with increasing metal/linker ratio within the investigated range. These results imply that the number of nuclei increases with increasing linker concentration, at the expense of the eventual nucleus size, which decreases. Furthermore, the particle histograms in Figure 4.2.d show congruent shapes –within experimental errors– across different metal/linker conditions. It is clear that for all metal/linker cases small particles are always observed in the presence of larger ones (Figure 4.2.a-d), suggesting that nucleation of new nuclei is a frequent and an ongoing process throughout the 10 min synthesis time. Complementary characterization by Raman spectroscopy and X-ray diffraction (XRD) is performed for all samples and shown in Figures 4.3 and 4.4.

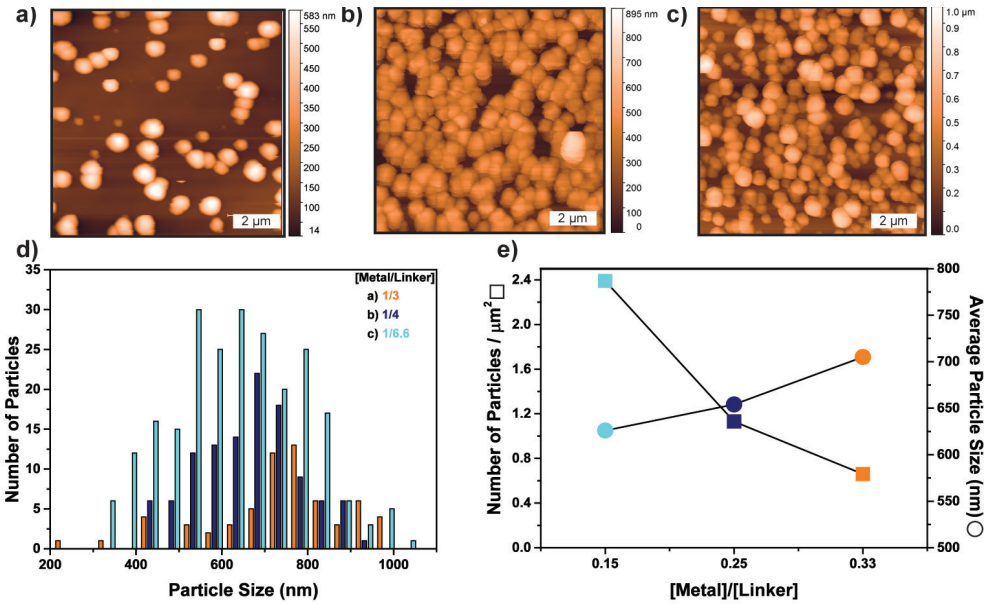

Figure 4.2. AFM micrographs for the Co-ZIF-67 thin-films prepared at different metal to linker concentrations **a)** 1/3, **b)** 1/4, **c)** 1/6.6. The resulting particle size histograms **d)**, and **e)** the variation of number of particles / µm^2 and average particle size at the aforementioned concentration regime.

Raman micro-spectroscopy measurements were executed for the identification of the Co-ZIF-67 thin-films prepared by metal to linker concentrations of 1/3, 1/4 and 1/6.6 along with its bulk analogue and the linker, 2-methylimidazole and the results are shown in Figure 4.3. The spectral features, appearing in the spectra of Co-ZIF-67 thin-films, are in good agreement with those of the bulk Co-ZIF-67 material along with the reported Raman spectra of the isostructural zinc variant of Co-ZIF-67, Zn-ZIF-8,[54,55]and confirming the formation of the desired porous material. The thin-films are also characterized by XRD in order to confirm the structure and the crystallinity. The results are illustrated in Figure 4.4. The comparison of the XRD diffractograms of the thin-films with their bulk analogue shows the formation of the crystalline Co-ZIF-67 structure.[56,57]

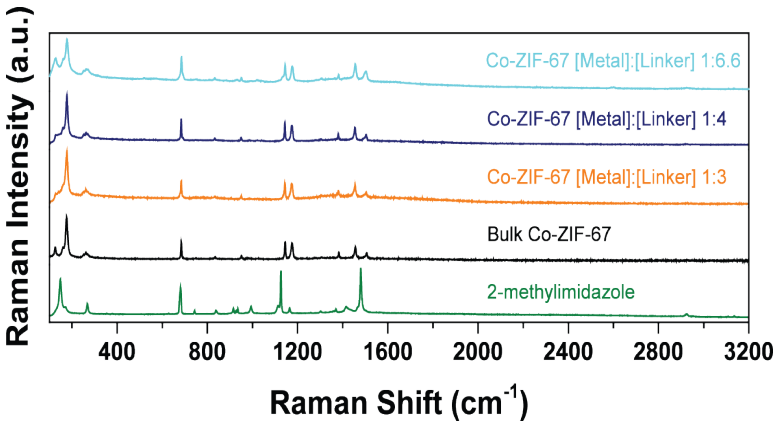

Figure 4.3. Comparison of Raman spectra of 2-methylimidazole linker, bulk Co-ZIF-67 and Co-ZIF-67 thin-films prepared with 1/3, 1/4 and 1/6.6 metal to linker concentrations.

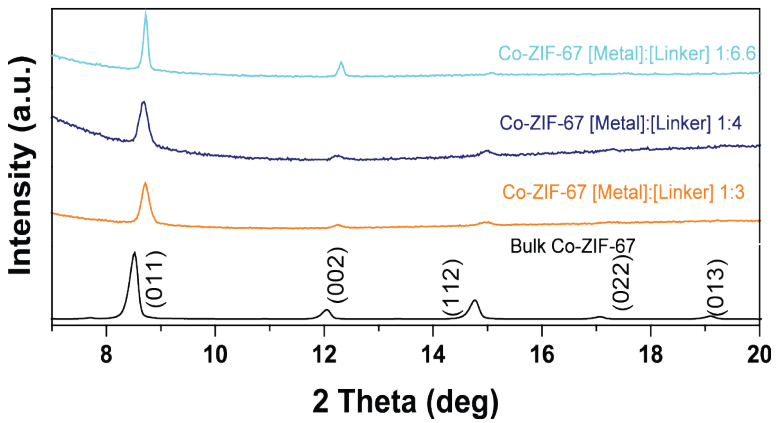

Figure 4.4. Comparison of XRD diffractograms of bulk Co-ZIF-67 and Co-ZIF-67 thin-films prepared with 1/3, 1/4 and 1/6.6 metal to linker concentrations.

In the second set of experiments, the effect of the synthesis temperature was examined by performing deposition at 0°C, 20°C and 40°C, while keeping the metal to linker ratio (1/4) and reaction time (10 min) constant. The resulting Co-ZIF-67 thin-films on a gold-coated substrate were probed by AFM (10x10 μm^2) as illustrated in Figure 4.5.a-c. Visual inspection of the AFM micrographs demonstrates that the average particle sizes increase with increasing synthesis temperature, while the number of nuclei remains constant. Indeed, the quantified AFM histograms (Figure 4.5.d-e) show that the overall number of particles detected is constant within experimental error, but that the average particle size significantly increases upon temperature increase. More precisely, the average calculated particle sizes range from 292 nm to 654 nm and 1098 nm for temperatures from 0°C, 20°C and 40°C,

respectively (Figure 4.5.e). Such temperature-induced particle growth clearly results in an increase in the surface coverage. These results point out that the nucleus size increases with an increase in the temperature, whereas the number of nuclei formed is not affected to a lesser extent within the temperature range under study. Figures 4.6 and 4.7 show the further characterization of the thin-films through Raman spectroscopy and XRD, respectively. The results are in good agreement with the previously reported literature reports for Raman spectra[54,58] obtained and also for the XRD diffractograms[56,57] recorded. For the sample synthesized at 0°C, due to the low surface coverage and low crystallinity of the sample, it was not possible to obtain relevant information.

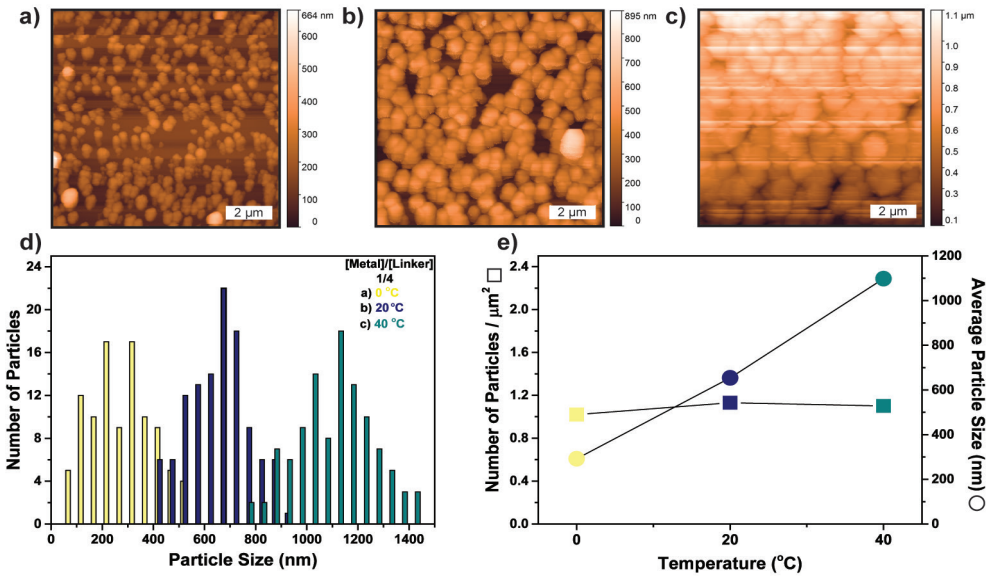

Figure 4.5. AFM micrographs of Co-ZIF-67 thin-films prepared at **a)** 0°C, **b)** 20°C, **c)** 40°C. The resulting particle size histograms **d)**, and **e)** the variation of number of particles / µm² and average particle size at the aforementioned temperature regime.

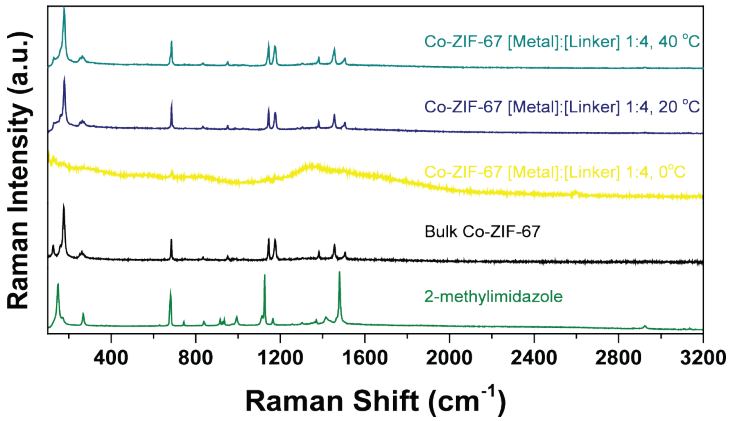

Figure 4.6. Comparison of the Raman spectra of 2-methylimidazole, bulk Co-ZIF-67 and the Co-ZIF-67 thin-films, prepared at 0°C, 20°C and 40°C.

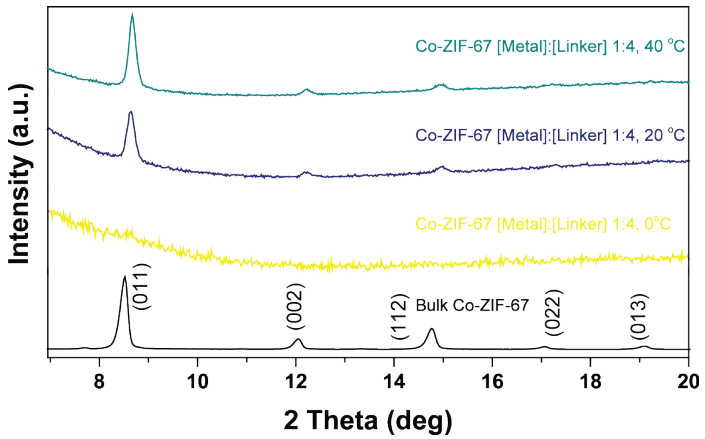

Figure 4.7. Comparison of the XRD diffractograms of bulk Co-ZIF-67 and the Co-ZIF-67 thin-films, prepared at 0°C, 20°C and 40°C.

Figure 4.8.a. illustrates a proposed reaction scheme, which leads to the formation of Zn-ZIF-8 and Co-ZIF-67. The mechanism involves three reaction steps: (1) linker coordination of Co^{2+} centers, (2) deprotonation of the 2-methylimidazole linker(s) and (3) oligomerization by linking together different Co^{2+} centers via deprotonated 2-methylimidazole ligands. The effect of varying metal/linker ratio and temperature can be explained by taking into account the proposed reaction mechanism. The increase in the linker concentration (decreasing metal/linker ratio) gives rise to an increase in the rate and extent of ligand exchange reactions between 2-methylimidazole linkers and methanol/water/nitrate ligands around Co^{2+}. Hence a higher linker concentration will lead to a Co^{2+} coordination sphere, which is richer in 2-methylimidazole linkers, established in a shorter period of time. As a result, a

higher concentration of linker coordinated Co^{2+} complexes will result in an increased reaction rate of 2-methylimidazole deprotonation. These deprotonated Co^{2+} complexes are vital for nucleation, since a single deprotonated 2-methylimidazole ligand can bridge two Co^{2+} centers, leading to oligomerization and therefore nucleus formation. It is thus expected that the nucleation rate increases for higher linker concentrations owing to the increase in the deprotonation rate, eventually yielding more nuclei/particles for higher linker concentrations (i.e., lower metal/linker ratios). Apparently, more nuclei formed per μm^2 leads to smaller particles, as shown in the AFM micrographs (Figure 4.2). This can be rationalized by the fact that the metal and linker constituents in the solution are to be distributed amongst a larger number of nuclei for lower metal/ linker ratios, leading to smaller particles. These findings regarding the eventual nucleus size are in line with previously reported literature results of Cravillon et al., Lim et al., and Saha et al..[29,50,59]

The influence of the synthesis temperature is significantly different compared to the metal/linker ratio. For increasing temperatures, the number of nuclei remains constant, but their eventual size increases significantly after 10 min of synthesis time. This suggests that the nucleation rate is not affected by a temperature change, though the growth rate is strongly sensitive to temperature alterations. Alternatively, it could be hypothesized that the oligomerization rate exhibits a strong temperature dependency. By increasing the temperature, the activation energy of oligomerization can be overcome more easily, eventually yielding larger particles. While the linker/metal ratio has a major influence on the nucleation rate –though the particle size is also influenced– the temperature only influences the eventual size of the particles deposited in the thin-film. This knowledge allows to rationally tune the size of particles by changing the synthesis temperature.

For the third set of experiments, the influence of the metal ion type on the nucleation and growth is examined by comparing isostructural Co-ZIF-67 and Zn-ZIF-8 under identical synthesis conditions (metal/linker = 1/4, room temperature and 10 min deposition time). AFM micrographs along with the corresponding particle size distributions of Zn-ZIF-8 and Co-ZIF-67 thin-films are shown in Figure 4.9.a. The average particle sizes were calculated as 75 and 626 nm for Zn-ZIF-8 and Co-ZIF-67, respectively. However, the number of nuclei formed for single layered Zn-ZIF-8 was observed to be double compared to the number of particles nucleated for single layered Co-ZIF-67 (Figure 4.9.a). It can be seen that the surface area below the curve for Co-ZIF-67 is much larger compared to Zn-ZIF-8. This implies that the total amount of material deposited for Co-ZIF-67 is exceedingly larger compared to the Zn-ZIF-8 case, suggesting more rapid growth for Co-ZIF-67. This particle size analysis shows that Co-ZIF-67 nucleates and grows faster under the same synthesis conditions, which will be explained in more detail below.

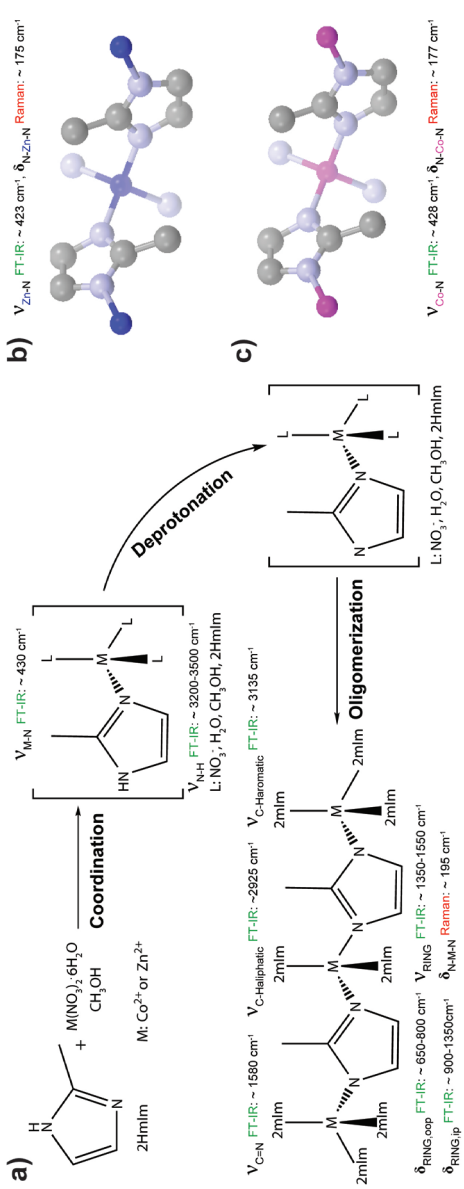

Figure 4.8. a) A proposed mechanism for the formation of Zn-ZIF-8 and its cobalt variant Co-ZIF-67 along with the characteristic FT-IR and Raman band signatures, **b)** coordination sphere of Zn-ZIF-8, **c)** coordination sphere of Co-ZIF-67 (hydrogen atoms are omitted for clarity, grey : carbon, light blue: nitrogen, dark blue: zinc, purple: cobalt).

4.3.2. Multistep Deposition

As shown above, the particle size and density in ZIF thin-films can be controlled by the synthesis temperature and linker/metal ratio. Obtaining fully closed films initially, and tuning the ZIF thin-films thickness in a later stage of deposition, is another film parameter to be controlled. This can be achieved by multilayer growth,

implying repetitive layer deposition.

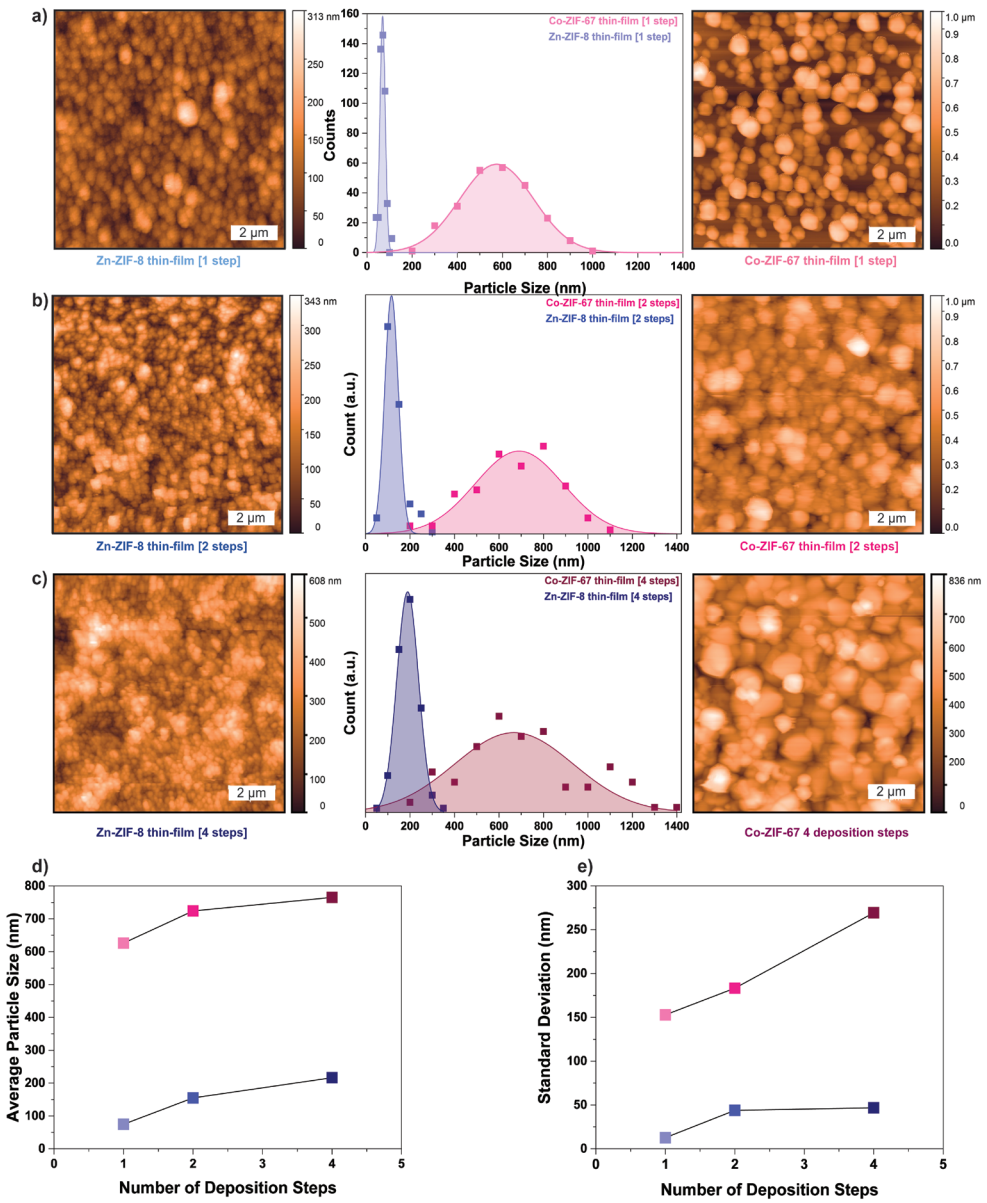

Figure 4.9. Comparison of AFM micrographs and particle size distributions of Zn-ZIF-8 and Co-ZIF-67 thin-films obtained through **a)** 1 step deposition, **b)** 2 steps deposition, **c)** 4 steps deposition. The variation of number of particles / μm^2 and average particle size through multiple deposition steps **d)**, and **e)** standard deviation of the given particle size distributions (Metal/Linker: 1/6.6, 20°C, each deposition step with a time of 10 min).

In order to assess the controllability of this synthetic strategy, a combined AFM-vibrational spectroscopy investigation is performed for thin-films obtained *via* one, two and four deposition steps. Figure 4.9 shows the AFM data of Zn-ZIF-8 and Co-ZIF-67 thin-films deposited by two (Figure 4.9.b) and four (Figure 4.9.c) deposition steps besides single step deposition previously discussed (Figure 4.9.a). First, the AFM micrographs show a coverage increase of the Au substrate with increasing number of deposition cycles for both Zn-ZIF-8 and Co-ZIF-67 thin-films. The particles on the top surface of the thin-film display a clear Gaussian distribution, from which the average and standard deviation are plotted in the graphs of Figure 4.9. The average particle size of Co- and Zn-based thin-films increases to a similar absolute extent as a result of film closure and growth. Likewise, a significant broadening is observed in the particle size distribution for both film types, as evident from the Gaussian standard deviation. This broadening is a consequence of the growth mechanism schematically represented in Figure 4.10.

During the first deposition step, ZIF particles are nucleated on the Au substrate surface and/or deposited from the synthesis solution. During the next step, these particles gradually grow through assembly from (oligomerized) linker-coordinated metals in the synthesis solution. In addition, newly nucleated particles are deposited on top of the particle layer, grown during step 1. After multiple steps, the particle layer becomes an increasingly intergrown thin-film through growth from the synthesis solution, yielding a polycrystalline intergrown ZIF thin-film. Indeed, SEM confirms the presence of a closed film on which newly nucleated, rhombic dodecahedrally shaped ZIF particles are deposited during the last synthesis step of the multistep process (Figure 4.10).

This growth mechanism is compatible with the particle broadness observation in the AFM histograms, which arises from (1) previously deposited particles which increased size via repetitive growth from the synthesis solution, in combination with (2) newly deposited (smaller) ZIF particles at the top surface. These findings suggest that, through the proposed multiple deposition step approach, eventual particle size and density, as well as surface coverage/film thickness can be manipulated. This can be achieved by selecting the correct synthesis conditions, including the optimal (1) metal/linker ratio, (2) temperature and (3) the number of deposition steps. The thickness of thin-films can also be varied by a method proposed by Caro et al.[60]. However the multi-step approach proposed here can achieve better control over thickness of the film in particular, as well as a control over the other aforementioned film properties (grain size and density of particles).

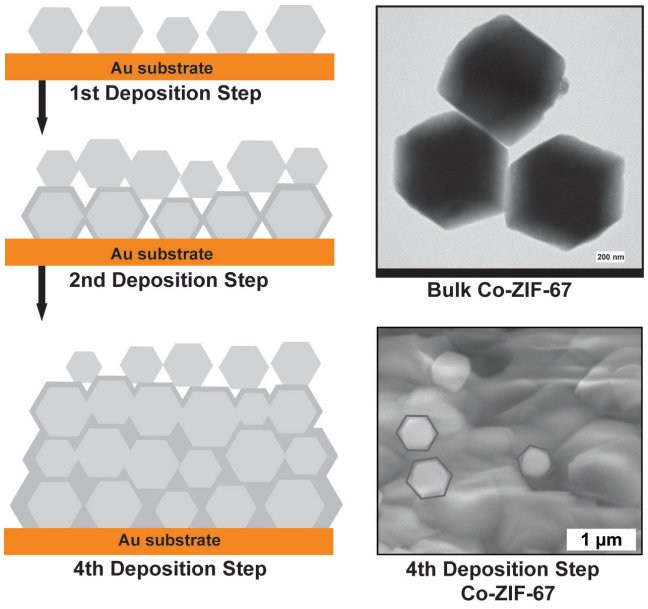

Figure 4.10. (left) Mechanism proposed regarding ZIF thin-film growth through direct synthesis method with multiple deposition steps; (right, top) TEM of bulk Co-ZIF-67 crystals shown in schematic representation; (right, bottom) SEM image of Co-ZIF-67 thin film after 4 deposition steps.

SEM measurements were also carried out for bulk Zn-ZIF-8 and Co-ZIF-67. The results, shown in Figure 4.7, indicate that the average particle sizes for Co-ZIF-67 is five times larger than for Zn-ZIF-8 (i.e., ~ 141 vs. ~ 786 nm).

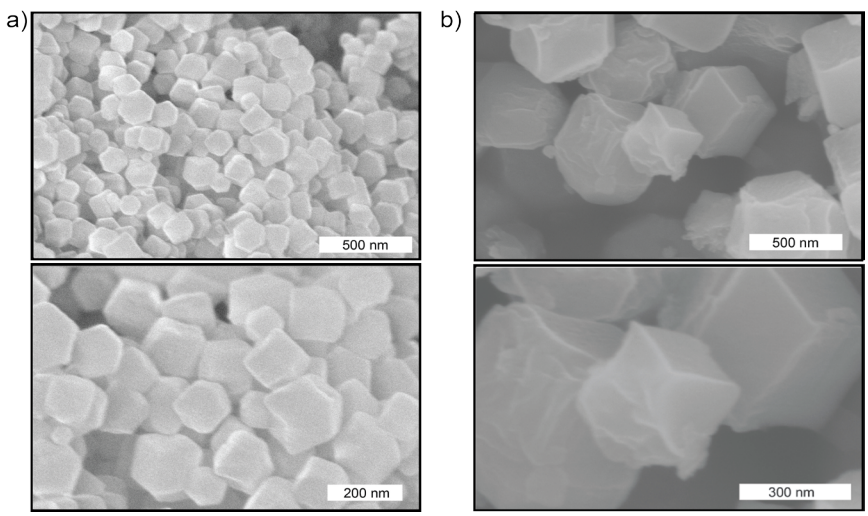

Figure 4.11. SEM micrographs of bulk **a)** Zn-ZIF-8 and **b)** Co-ZIF-67 materials.

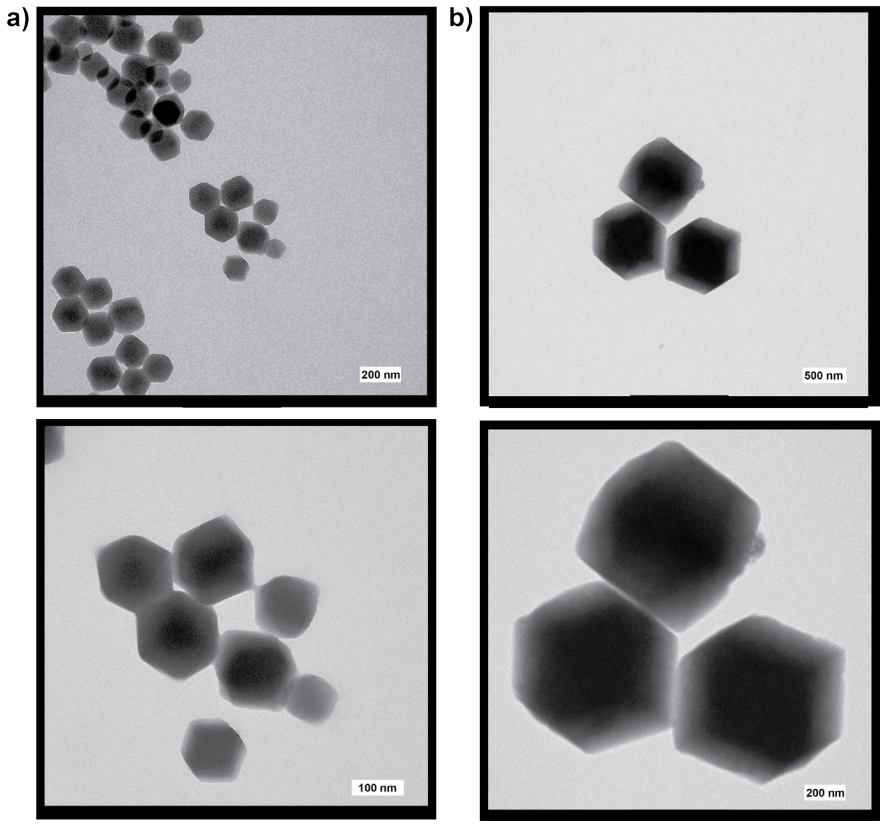

Figure 4.12. TEM micrographs of bulk **a)** Zn-ZIF-8 and **b)** Co-ZIF-67 materials.

Rhombic dodecahedra particles were observed for Zn-ZIF-8 and Co-ZIF-67 materials. For clarity, TEM measurements were also carried out for more visual inspection of bulk Zn-ZIF-8 and Co-ZIF-67, as shown in Figure 4.12.

Besides AFM mapping of the Co- and Zn-based thin-film morphology, complementary chemical information is gained by vibrational spectroscopy, namely diffuse reflectance infrared Fourier transformed spectroscopy (DRIFTS) and Raman spectroscopy. DRIFT spectroscopy measurements are carried out in a spectral region ranging from 400-4000 cm^{-1} in order to provide molecular scale chemical bond information. Figure 4.13.a. displays the DRIFTS spectra of the Zn-ZIF-8 and Co-ZIF-67 thin-films obtained after 4 depositions steps, as well as their bulk analogues and the 2-methylimidazole linker references. DRIFTS spectra of the thin-films of Zn-ZIF-8 and Co-ZIF-67 obtained after 1 and 2 step depositions are provided in Figure 4.14, displaying similar spectral features compared to their 4 step analogues.

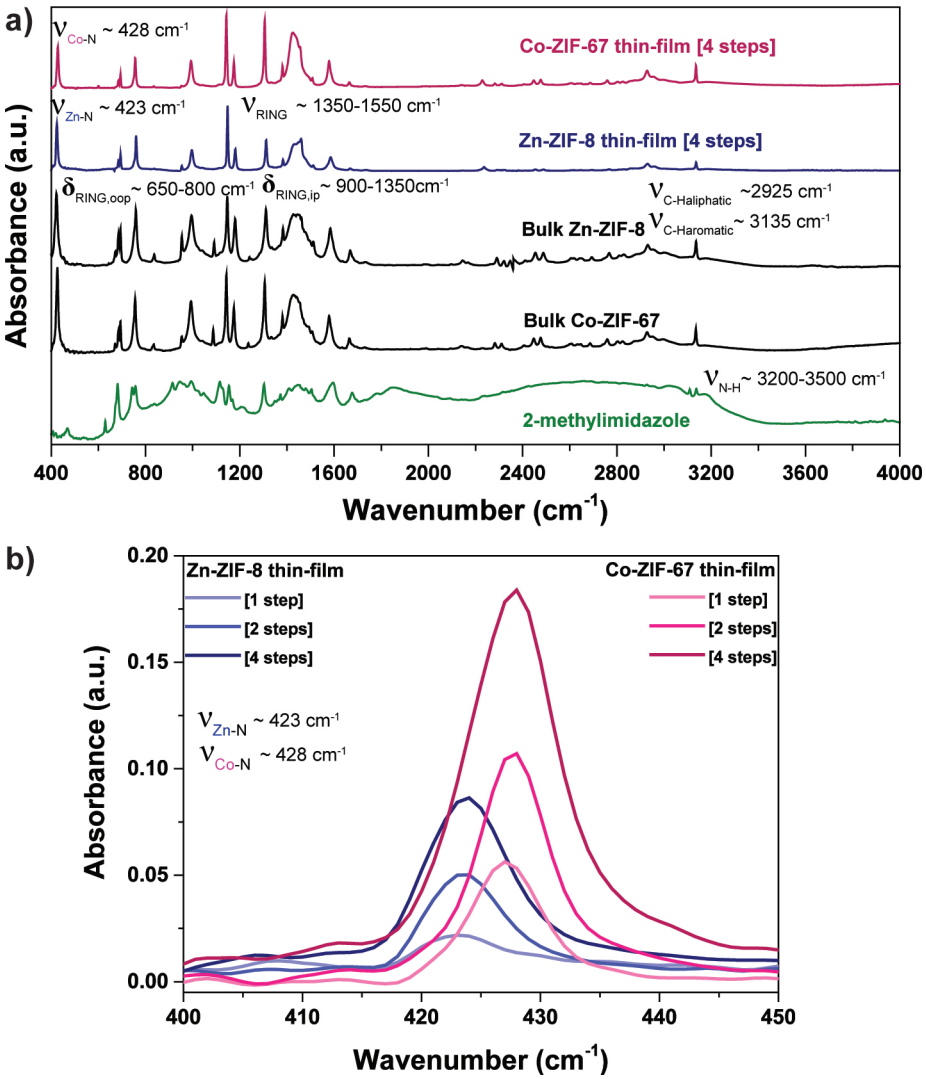

Figure 4.13. Comparison of DRIFT spectra of the 2-methylimidazole linker, bulk Co-ZIF-67, bulk Zn-ZIF-8, Zn-ZIF-8 and Co-ZIF-67 thin-films obtained by 4 deposition steps, **b)** DRIFT spectra of Zn-ZIF-8 and Co-ZIF-67 thin-films obtained through, 1, 2 and 4 deposition steps in the region of 400-450 cm^{-1}. The characteristic bands were also provided.

In general, the Zn-ZIF-8 and Co-ZIF-67 thin-film spectra obtained after four deposition steps (as well as 1 and 2 deposition steps, Figure 4.14) exhibit IR bands which are typical of bulk ZIF materials.[41,61–64] In particular, going from low to high wavenumbers, multiple bending/stretching vibrations are identified: Co-N/Zn-N stretching (~ 430 cm^{-1}), ring out-of-plane bending (~ 650-800 cm^{-1}), ring in-plane bending (~ 900-1350 cm^{-1}), ring stretching (~ 1350-1550 cm^{-1}), C=N stretching (~ 1580 cm^{-1}), CH_3 (~ 2925 cm^{-1}) and C-H aromatic (~ 3135 cm^{-1}) stretching modes. In

Figure 4.8.a-c and 4.13.a, characteristic vibrations are highlighted as observed for both Zn-ZIF-8 and Co-ZIF-67 (thin-films).[41,45,61,62,64]

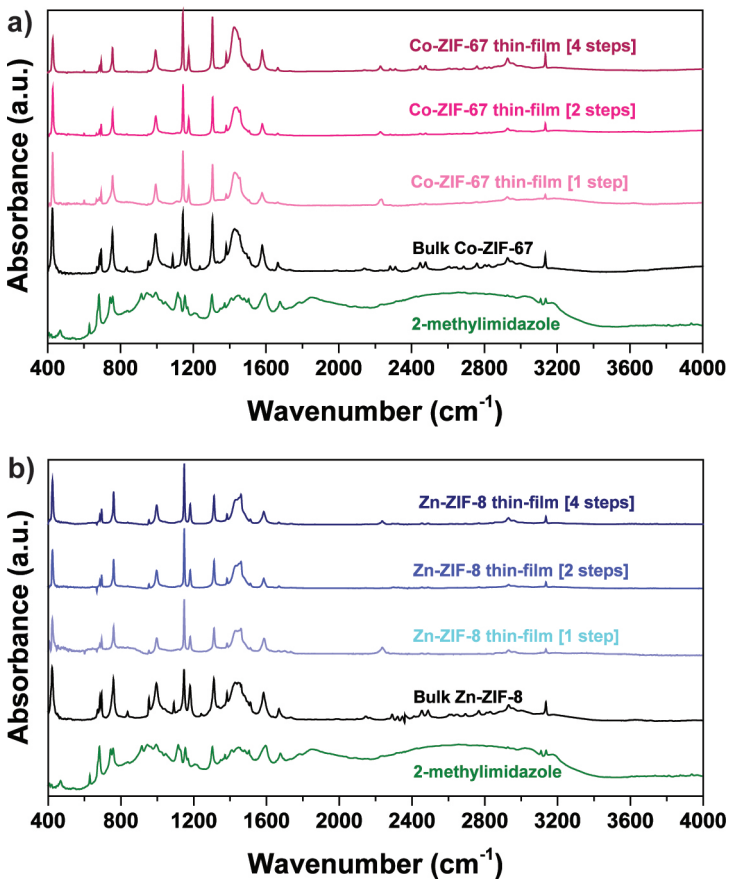

Figure 4.14. Comparison of the DRIFT spectra of the 2-methylimidazole linker, bulk Co-ZIF-67, bulk Zn-ZIF-8, Zn-ZIF-8 and Co-ZIF-67 thin-films obtained by 4 deposition steps, **b)** DRIFT spectra of Zn-ZIF-8 and Co-ZIF-67 thin-films obtained through, 1, 2 and 4 deposition steps in the region of 400-450 cm^{-1}. The characteristic bands were also provided.

A detailed comparison between the IR spectra of bulk and thin-film grown materials shows that more distinct IR bands are observable for bulk ZIFs, especially in the ring stretching and vibrational regions (~ 830 cm^{-1}, 940 cm^{-1}, 1070 cm^{-1}, 1240 cm^{-1}, etc.). This suggests that bulk ZIF framework is less defective/perturbed in nature relative to its thin-film analogue, leading to less bond/ring disorder. Note that the absence of broad N-H stretching bands in the region between 3200-3500 cm^{-1} in the DRIFT spectra of Zn-ZIF-8 and Co-ZIF-67 demonstrate that the linker 2-methylimidazole is incorporated in the ZIF-8/-67 thin-films in their deprotonated state.[65] A detailed

zoom into the Co-N and Zn-N stretching region (Figure 4.13.b) of Co-ZIF-67 and Zn-ZIF-8 thin-film IR spectra shows a blue shift for Co- (~ 428 cm^{-1}) relative to Zn-based (~ 423 cm^{-1}) thin-films. The more electronegative nature of Co^{2+} compared to Zn^{2+} induces more ionized bonds,[45] leading to more tight bonds with M-N stretching vibrations at higher wavenumbers. The spectral shift observed for the metal-nitrogen vibrations is supported by DFT calculations reported by Krokidas et al.. The authors obtained a higher force constant for Co-ZIF-67 compared to Zn-ZIF-8. [66] Furthermore, Krokidas et al. simulated the Zn-N/Co–N bond length and angle, yielding 1.98 Å Zn-N and 1.96 Å Co-N bonds, in line with stronger Co-N bonds.

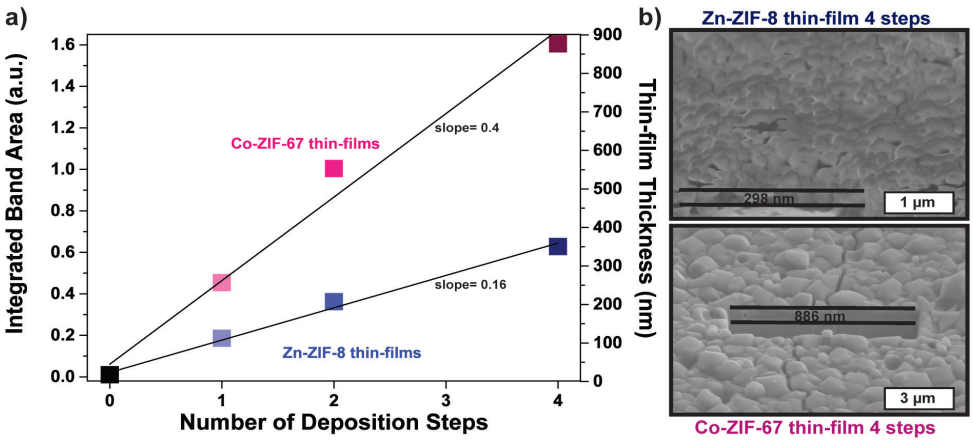

Figure 4.15. a) The variation of absorbance in terms of integrated band area and expected thin-film thickness as a function of number of deposition steps, **b)** FIB-SEM micrograph and the cross-section thickness of the Zn-ZIF-8 and Co-ZIF-67 thin-films prepared with 4 deposition steps.

The more electronegative nature of Co^{2+} is not only manifested at the molecular scale. Its higher reactivity/electronegativity results in a faster nucleation and growth, as microscopically observed by AFM. Therefore, the chemically sensitive information abstracted by IR can, in strong connection with AFM, provide the underlying clarification for film properties manifested at a microscopic level. Further linking of IR information to the Zn-ZIF-8 and Co-ZIF-67 thin-film morphology can be achieved by using the Co-N/Zn-N vibrational band intensities as markers for the thickness of Zn-ZIF-8 and Co-ZIF-67 thin-films. Indeed, AFM allows to image the top surface of thin-films, and is therefore ideal to study the onset of thin-film nucleation and growth, but cannot provide thickness information after film closure. In this respect, IR can probe bulk information in contrast to surface sensitive AFM. In Figure 4.13.b, an intensity increase of the Zn-N and Co-N spectral bands is observed upon deposition of multiple steps. In Figure 4.15.a, the integrated areas

below these bands are plotted versus the number of deposition steps: the band areas are proportional to the average film thickness. The latter is calibrated through measurement of the local thickness of Zn-ZIF-8 (~ 300 nm) and Co-ZIF-67 (~ 900 nm) thin-films after four deposition steps by FIB-SEM (Figure 4.13.b). These trends confirm that the nucleation and growth rate of Co-ZIF-67 thin-films exceeds the one of Zn-ZIF-8. In addition, a linear increase in the film thickness is observed within experimental uncertainty for both Co-ZIF-67 and Zn-ZIF-8 thin-films synthesized by multistep synthesis. This is a natural consequence of the fact that during the multistep synthesis method, every step involves an identical direct synthesis solution, which is contacted with the thin-film under the same reaction time. This repetitive synthetic protocol is therefore ideally suited for the thickness control of ZIF thin-films on the micrometer scale. The as-prepared thin-films were further characterized by XRD and Raman spectroscopy.

With the purpose of getting further information concerning the crystallinity and the structure of the as-prepared Zn-ZIF-8 and Co-ZIF-67 thin-films, XRD diffractograms of the thin-films were recorded and compared with their bulk analogues. The results are given in Figure 4.16. In the XRD diffractograms of the Zn-ZIF-8 thin-films, the most prominent diffraction peak corresponding to the (011) plane is observed for all deposition steps and as the number of deposition steps increased the (002) and (112) planes become more apparent in the XRD diffractograms (Figure 4.16.a). Furthermore, the diffractograms of the Zn-ZIF-8 thin-films confirm the structure of the crystallinity when compared with their bulk analogue, which is also in good agreement with the previously reported XRD diffractograms.[50,54,67–69] Figure 4.16.b shows the comparison of XRD diffractograms of bulk Co-ZIF-67 and Co-ZIF-67 thin-films. Comparison of the XRD diffractograms reveal the presence of the first three diffraction peaks corresponding to the (011), (002) and (112) planes, respectively and also confirms the nature and structure of the as-prepared Co-ZIF-67 thin-films. [45,56,57,70,71]

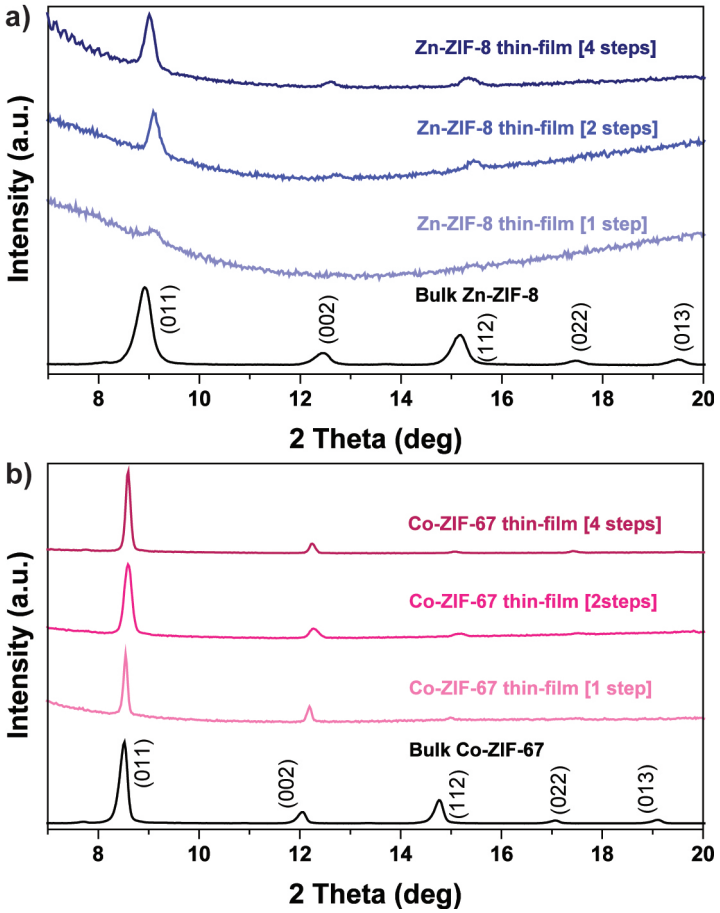

Figure 4.16. Comparison of the XRD diffractograms of **a)** bulk Zn-ZIF-8 and **b)** Co-ZIF-67 thin-films obtained through 1, 2 and 4 deposition steps along with their bulk analogues.

Figure 4.17.a shows the Raman spectra of the 2-methylimidazole linker, bulk Zn-ZIF-8 and Zn-ZIF-8 thin-films obtained after one, two and four deposition steps. Although ZIF-8 and ZIF-67 are most probably the most studied ZIF materials, it is important to remark that there have not been very detailed Raman spectroscopy studies except for the paper published by Kumari et al. on Zn-ZIF-8.[54] The spectral features, appearing in the spectra of Zn-ZIF-8 thin films, are in good agreement with those of the bulk Zn-ZIF-8 material confirming the formation of the desired porous material.[54,72] Raman micro-spectroscopy measurements were also executed for Co-ZIF-67 thin-films obtained after one, two and four deposition steps along with its bulk analogue and the linker, 2-methylimidazole. These results are included in Figure 4.17.b. Here again, the Raman spectra of the Co-ZIF-67 thin-films are in good agreement with its bulk analogue, confirming the formation of the desired porous material.

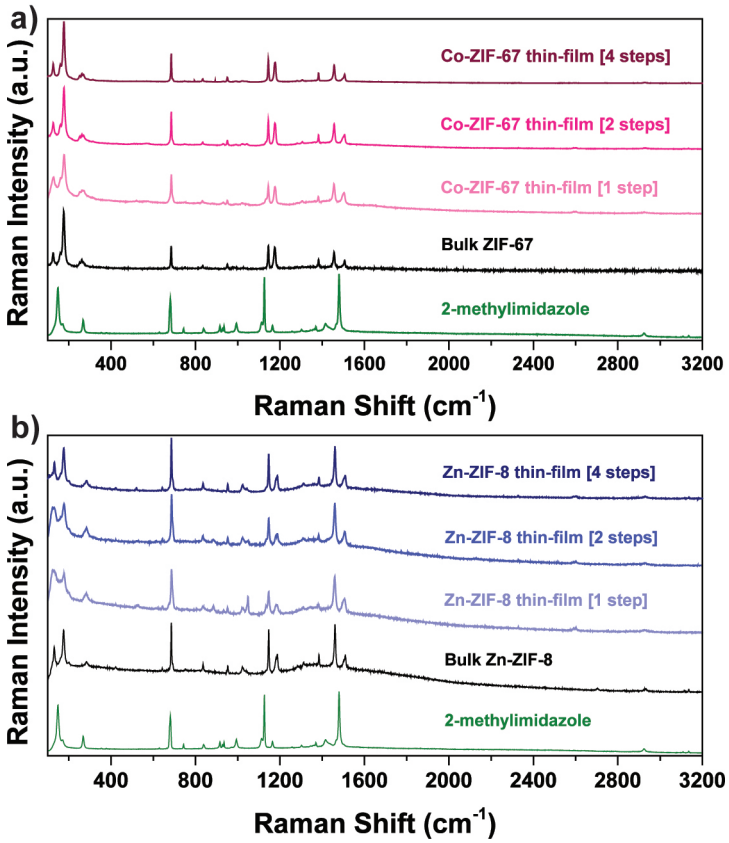

Figure 4.17. Comparison of the Raman spectra of **a)** 2-methylimidazole linker, bulk Co-ZIF-67 and Co-ZIF-67 thin-films with 1, 2 and 4 depositions steps and **b)** 2-methylimidazole linker, bulk Zn-ZIF-8 and Zn-ZIF-8 thin-films with 1, 2 and 4 depositions steps.

Figure 4.18.a and 4.18.b illustrate the comparison of Raman spectra of Zn-ZIF-8 and Co-ZIF-67 thin-films in the region of 145-195 cm^{-1} where the nitrogen-metal-nitrogen (N-M-N) deformation vibration is observed (Figure 8).[73] Figure 4.18.b. shows the variation in the N-M-N band maxima with one, two and four deposition steps. This characteristic band is located at higher wavenumbers for Co-ZIF-67 than that of Zn-ZIF-8 for all deposition steps (including bulk analogues). The differing spectral positions of the Zn-ZIF-8 and Co-ZIF-67 series observed for the N-M-N vibration is in line with the DRIFTS data, showing the presence of more stiff N-Co-N bonds compared to N-Zn-N, which can be attributed to the higher electronegativity/ionicity of Co^{2+}. In addition, the band maxima slightly shifts from higher to lower wavenumber with increasing deposition steps indicating that the force constant decreases for both Zn-ZIF-8 and Co-ZIF-67 thin-films. It is plausible to propose that the more intergrown films undergo a bond relaxation to a certain extent owing to an increased structural stability.

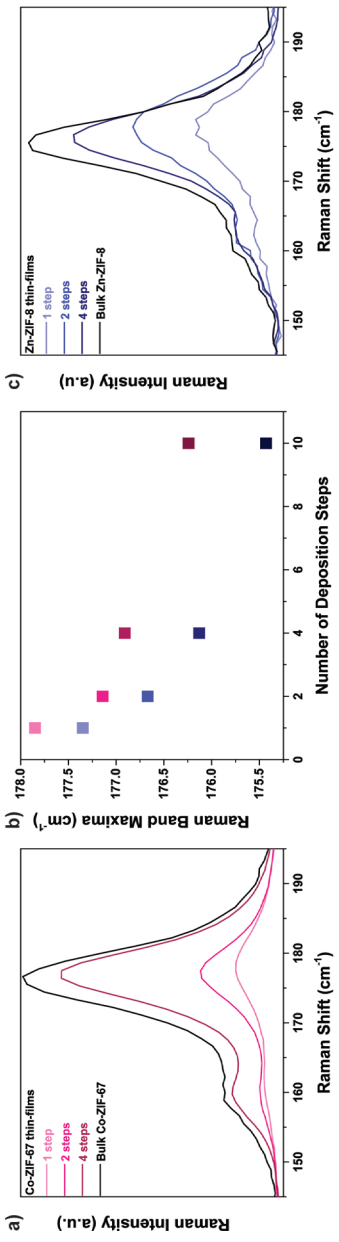

Figure 4.18. Comparison of the Raman spectra of **a)** Co-ZIF-67 thin-films obtained after 1, 2 and 4 deposition step along with bulk Co-ZIF-67, **c)** Zn-ZIF-8 thin-films obtained after 1, 2 and 4 deposition steps along with their bulk analogue in the region of 145-195 cm^{-1}. **b)** Raman band maxima (deformation mode, N-M-N) vs. number of deposition steps for the bands shown in **a)** and **c)**.

4.4. Conclusions

The influence of different synthesis parameters on the formation and properties of isostructural Co-ZIF-67 and Zn-ZIF-8 thin-films is investigated. Direct synthesis is employed for ZIF thin-film deposition, a method involving both metal and linker constituents in a single solution. To unravel the influence of synthesis parameters,

such as (1) metal/linker ratio, (2) temperature and (3) metal type, a single deposition step is used. Atomic force microscopy (AFM) is utilized to map the surface topology in 10 x 10 μm regions at the initial stages of ZIF thin-film formation, allowing quantification of the number and size of deposited ZIF nuclei during synthesis. A decreasing metal/linker ratio –i.e. higher linker concentration- induces a higher nucleation rate, resulting in an increased number of nuclei populating the early thin-film structure. It is suggested that the nucleus size is inversely proportional to the number of nuclei when varying the metal/linker ratio. A factor strongly dictating the particle size is the synthesis temperature: while the number of nuclei remains constant, the particle size strongly increases with increasing thermal activation. Finally, Co^{2+} as the constituent metal in Co-ZIF-67 exhibits a more reactive nucleation and growth behaviour compared to Zn^{2+} in isostructural Zn-ZIF-8. This is caused by the higher electronegativity of Co^{2+} cations compared to Zn^{2+}, leading to more polarized/ionic Co-N bonds relative to Zn-N. This has been observed in the Co/Zn-N stretching vibration in infrared (IR) spectroscopy, where the Co-N vibrational band is blue shifted with 5 cm^{-1} relative to the Zn-N vibrational band.

While the number and size of particles constituting the thin-film can be controlled by parameters, such as metal/linker ratio and the temperature, the eventual film thickness can be tuned by multistep direct synthesis. By repetitive single step synthesis, a linear growth rate is observed by bulk IR with the number of repeating synthesis steps. During the first deposition step, new nuclei populate the substrate surface. After multiple steps, however, pre-existing particles undergo continuous growth and coalesce, leading to film closure. In addition, newly nucleated particles are deposited on top of the film. In general, it is observed for all ZIF thin-films that the IR spectra contain less pronounced features compared to bulk ZIF-67 and ZIF-8. This suggests that the thin-film structure at the molecular level is more perturbed, i.e. more defective in nature. Finally, this work shows that coupling molecular-scale vibrational spectroscopy information with topologic knowledge acquired via atomic force microscopy aids in linking molecular interactions, which manifest at the microscale of the thin-film morphology.

4.5. Acknowledgements

Iván Garcia Torregrosa (Utrecht University) is thanked for acquiring the FIB-SEM data, while Peter de Peinder (VibSpec) is thanked for his help with DRIFT spectroscopy measurements.

4.6. References

[1] G. Férey, *Chem. Soc. Rev.* **2008**, *37*, 191–214.

[2] M. Tu, S. Wannapaiboon, R. A. Fischer, *Dalt. Trans.* **2013**, *42*, 16029–16035.

[3] M. Tu, S. Wannapaiboon, K. Khaletskaya, R. A. Fischer, *Adv. Funct. Mater.* **2015**, *25*, 4470–4479.

[4] O. Shekhah, J. Liu, R. A. Fischer, C. Wöll, *Chem. Soc. Rev.* **2011**, *40*, 1081–1106.

[5] S. T. Meek, J. A. Greathouse, M. D. Allendorf, *Adv. Mater.* **2011**, *23*, 249–267.

[6] S. Qiu, M. Xue, G. Zhu, *Chem. Soc. Rev.* **2014**, *43*, 6116–6140.

[7] D. J. Tranchemontagne, J. L. Mendoza-Cortés, M. O'Keeffe, O. M. Yaghi, *Chem. Soc. Rev.* **2009**, *38*, 1257–1283.

[8] A. Betard, R. A. Fischer, *Chem. Rev.* **2012**, *112*, 1055–1083.

[9] O. M. Yaghi, M. O'Keeffe, N. W. Ockwig, H. K. Chae, M. Eddaoudi, J. Kim, *Nature* **2003**, *423*, 705–714.

[10] B. Liu, *J. Mater. Chem.* **2012**, *22*, 10094–10101.

[11] D. Zacher, O. Shekhah, C. Wöll, R. A. Fischer, *Chem. Soc. Rev.* **2009**, *38*, 1418.

[12] N. W. Ockwig, O. Delgado-Friedrichs, M. O'Keeffe, O. M. Yaghi, *Acc. Chem. Res.* **2005**, *38*, 176–182.

[13] A. U. Czaja, N. Trukhan, U. Müller, *Chem. Soc. Rev.* **2009**, *38*, 1284–1293.

[14] R. J. Kuppler, D. J. Timmons, Q.-R. Fang, J.-R. Li, T. a. Makal, M. D. Young, D. Yuan, D. Zhao, W. Zhuang, H.-C. Zhou, *Coord. Chem. Rev.* **2009**, *253*, 3042–3066.

[15] U. Mueller, M. Schubert, F. Teich, H. Puetter, K. Schierle-Arndt, J. Pastré, *J. Mater. Chem.* **2006**, *16*, 626–636.

[16] H. B. Tanh Jeazet, C. Staudt, C. Janiak, *Dalt. Trans.* **2012**, *41*, 14003–14027.

[17] J.-R. Li, R. J. Kuppler, H.-C. Zhou, *Chem. Soc. Rev.* **2009**, *38*, 1477–1504.

[18] H.-L. Jiang, Q. Xu, *Chem. Commun.* **2011**, *47*, 3351–3370.

[19] A. C. McKinlay, B. Xiao, D. S. Wragg, P. S. Wheatley, I. L. Megson, R. E. Morris, *J. Am. Chem. Soc.* **2008**, *130*, 10440–10444.

[20] M. Eddaoudi, J. Kim, N. Rosi, D. Vodak, J. Wachter, M. O'Keeffe, O. M. Yaghi, *Science* **2002**, *295*, 469–472.

[21] M. Ranocchiari, J. A. van Bokhoven, *Phys. Chem. Chem. Phys.* **2011**, *13*, 6388–6396.

[22] J. Gascon, M. D. Hernández-Alonso, A. R. Almeida, G. P. M. van Klink, F. Kapteijn, G. Mul, *ChemSusChem* **2008**, *1*, 981–983.

[23] C. Chizallet, S. Lazare, D. Bazer-Bachi, F. Bonnier, V. Lecocq, E. Soyer, A.-A. Quoineaud, N. Bats, *J. Am. Chem. Soc.* **2010**, *132*, 12365–12377.

[24] E. V. Ramos-Fernandez, M. Garcia-Domingos, J. Juan-Alcañiz, J. Gascon, F. Kapteijn, *Appl. Catal. A Gen.* **2011**, *391*, 261–267.

[25] J. Gascon, A. Corma, F. Kapteijn, F. X. Llabrés i Xamena, *ACS Catal.* **2014**, *4*, 361–378.

[26] K. S. Park, Z. Ni, A. P. Cote, J. Y. Choi, R. Huang, F. J. Uribe-Romo, H. K. Chae, M. O'Keeffe, O. M. Yaghi, *Proc. Natl. Acad. Sci.* **2006**, *103*, 10186–10191.

[27] Z. Öztürk, J. P. Hofmann, M. Lutz, M. Mazaj, N. Z. Logar, B. M. Weckhuysen, *Eur. J. Inorg. Chem.* **2015**, 1625–1630; Chapter 2 of this PhD Thesis.

[28] J. Cravillon, C. a. Schröder, H. Bux, A. Rothkirch, J. Caro, M. Wiebcke, *CrystEngComm* **2012**, *14*, 492–498.

[29] J. Cravillon, R. Nayuk, S. Springer, A. Feldhoff, K. Huber, M. Wiebcke, *Chem. Mater.* **2011**, *23*,

2130–2141.

[30] J. Cravillon, S. Münzer, S.-J. Lohmeier, A. Feldhoff, K. Huber, M. Wiebcke, *Chem. Mater.* **2009**, *21*, 1410–1412.

[31] J. Cravillon, C. A. Schröder, R. Nayuk, J. Gummel, K. Huber, M. Wiebcke, *Angew. Chem. Int. Ed.* **2011**, *50*, 8067–8071.

[32] S. R. Venna, J. B. Jasinski, M. A. Carreon, *J. Am. Chem. Soc.* **2010**, *132*, 18030–18033.

[33] A. Phan, C. J. Doonan, F. J. Uribe-Romo, C. B. Knobler, M. O'Keeffe, O. M. Yaghi, *Acc. Chem. Res.* **2010**, *43*, 58–67.

[34] H. Hayashi, A. P. Côté, H. Furukawa, M. O'Keeffe, O. M. Yaghi, *Nat. Mater.* **2007**, *6*, 501–506.

[35] S. R. Venna, M. A. Carreon, *J. Am. Chem. Soc.* **2010**, *132*, 76–78.

[36] H. Bux, A. Feldhoff, J. Cravillon, M. Wiebcke, Y.-S. Li, J. Caro, *Chem. Mater.* **2011**, *23*, 2262–2269.

[37] A. Huang, H. Bux, F. Steinbach, J. Caro, *Angew. Chem.* **2010**, *49*, 4958–4961.

[38] G. Lu, J. T. Hupp, *J. Am. Chem. Soc.* **2010**, *132*, 7832–7833.

[39] H. Jiang, B. Liu, T. Akita, M. Haruta, H. Sakurai, Q. Xu, *J. Am. Chem. Soc.* **2009**, *131*, 11302–11303.

[40] C. M. Miralda, E. E. Macias, M. Zhu, P. Ratnasamy, M. a. Carreon, *ACS Catal.* **2012**, *2*, 180–183.

[41] Y. Hu, H. Kazemian, S. Rohani, Y. Huang, Y. Song, *Chem. Commun.* **2011**, *47*, 12694–12696.

[42] C.-Y. Sun, C. Qin, X.-L. Wang, G.-S. Yang, K.-Z. Shao, Y.-Q. Lan, Z.-M. Su, P. Huang, C.-G. Wang, E.-B. Wang, *Dalt. Trans.* **2012**, *41*, 6906–6909.

[43] S. A. Moggach, T. D. Bennett, A. K. Cheetham, *Angew. Chem. Int. Ed.* **2009**, *48*, 7087–7089.

[44] G. Kaur, R. K. Rai, D. Tyagi, X. Yao, P.-Z. Li, X. Yang, Y. Zhao, Q. Xu, S. K. Singh, *J. Mater. Chem. A* **2016**, *4*, 14932–14938.

[45] H. T. Kwon, H.-K. Jeong, A. S. Lee, H. S. An, J. S. Lee, *J. Am. Chem. Soc.* **2015**, *137*, 12304–12311.

[46] C. Wang, F. Yang, L. Sheng, J. Yu, K. Yao, L. Zhang, Y. Pan, *Chem. Commun.* **2016**, *52*, 12578–12581.

[47] H. Yang, X.-W. He, F. Wang, Y. Kang, J. Zhang, *J. Mater. Chem.* **2012**, *22*, 21849–21851.

[48] J. P. Patterson, P. Abellan, M. S. Denny, C. Park, N. D. Browning, S. M. Cohen, J. E. Evans, N. C. Gianneschi, *J. Am. Chem. Soc.* **2015**, *137*, 7322–7328.

[49] Y. Pan, D. Heryadi, F. Zhou, L. Zhao, G. Lestari, H. Su, Z. Lai, *CrystEngComm* **2011**, *13*, 6937–6940.

[50] I. H. Lim, W. Schrader, F. Schüth, *Chem. Mater.* **2015**, *27*, 3088–3095.

[51] B. Pattengale, S. Yang, J. Ludwig, Z. Huang, X. Zhang, J. Huang, *J. Am. Chem. Soc.* **2016**, *138*, 8072–8075.

[52] P. Y. Moh, P. Cubillas, M. W. Anderson, M. P. Attfield, *J. Am. Chem. Soc.* **2011**, *133*, 13304–13307.

[53] M. Tu, S. Wannapaiboon, R. A. Fischer, *Inorg. Chem. Front.* **2014**, *1*, 442–463.

[54] G. Kumari, K. Jayaramulu, T. K. Maji, C. Narayana, *J. Phys. Chem. A* **2013**, *117*, 11006–11012.

[55] S. Tanaka, K. Fujita, Y. Miyake, M. Miyamoto, Y. Hasegawa, T. Makino, S. Van der Perre, T. Van Assche, G. V. Baron, J. F. M. Denayer, *J. Phys. Chem. C* **2015**, *119*, 28430–28439.

[56] J. Qian, F. Sun, L. Qin, *Mater. Lett.* **2012**, *82*, 220–223.

[57] A. F. Gross, E. Sherman, J. J. Vajo, *Dalt. Trans.* **2012**, *41*, 5458–5460.

[58] X. Zeng, L. Huang, C. Wang, J. Wang, J. Li, X. Luo, *ACS Appl. Mater. Interfaces* **2016**, *8*,

20274–20282.

[59] S. Saha, S. Springer, M. E. Schweinefuß, D. Pontoni, M. Wiebcke, K. Huber, *Cryst. Growth Des.* **2016**, *16*, 2002–2010.

[60] Y. Liu, N. Wang, J. H. Pan, F. Steinbach, J. Caro, *J. Am. Chem. Soc.* **2014**, *136*, 14353–14356.

[61] E. L. Bustamante, J. L. Fernández, J. M. Zamaro, *J. Colloid Interface Sci.* **2014**, *424*, 37–43.

[62] X. Xu, Y. Sun, Q. Zhang, S. Wang, L. Zhang, Z. Wu, G. Lu, *ChemistrySelect* **2016**, *1*, 1763–1767.

[63] J. Yao, R. Chen, K. Wang, H. Wang, *Microporous Mesoporous Mater.* **2013**, *165*, 200–204.

[64] M. He, J. Yao, Q. Liu, K. Wang, F. Chen, H. Wang, *Microporous Mesoporous Mater.* **2014**, *184*, 55–60.

[65] K. Zhou, B. Mousavi, Z. Luo, S. Phatanasri, S. Chaemchuen, F. Verpoort, *J. Mater. Chem. A* **2017**, *5*, 952–957.

[66] P. Krokidas, M. Castier, S. Moncho, D. N. Sredojevic, E. N. Brothers, H. T. Kwon, H.-K. Jeong, J. S. Lee, I. G. Economou, *J. Phys. Chem. C* **2016**, *120*, 8116–8124.

[67] K. S. Park, Z. Ni, A. P. Cote, J. Y. Choi, R. Huang, F. J. Uribe-Romo, H. K. Chae, M. O'Keeffe, O. M. Yaghi, *Proc. Natl. Acad. Sci. U S A* **2006**, *103*, 10186–10191.

[68] L. Ge, A. Du, M. Hou, V. Rudolph, Z. Zhu, *RSC Adv.* **2012**, *2*, 11793–11800.

[69] J. Liu, J. He, L. Wang, R. Li, P. Chen, X. Rao, L. Deng, L. Rong, J. Lei, *Sci. Rep.* **2016**, *6*, 23667-1–11.

[70] J. Zhang, H. Hu, Z. Li, X. W. D. Lou, *Angew. Chem. Int. Ed.* **2016**, *55*, 3982–3986.

[71] H. Hu, J. Zhang, B. Guan, X. W. D. Lou, *Angew. Chem. Int. Ed.* **2016**, *55*, 9514–9518.

[72] D.-Y. Kim, B. N. Joshi, J.-G. Lee, J.-H. Lee, J. S. Lee, Y. K. Hwang, J.-S. Chang, S. Al-Deyab, J.-C. Tan, S. S. Yoon, *Chem. Eng. J.* **2016**, *295*, 49–56.

[73] K. H. Schmidt, A. Mueller, *Inorg. Chem.* **1975**, *14*, 2183–2187.

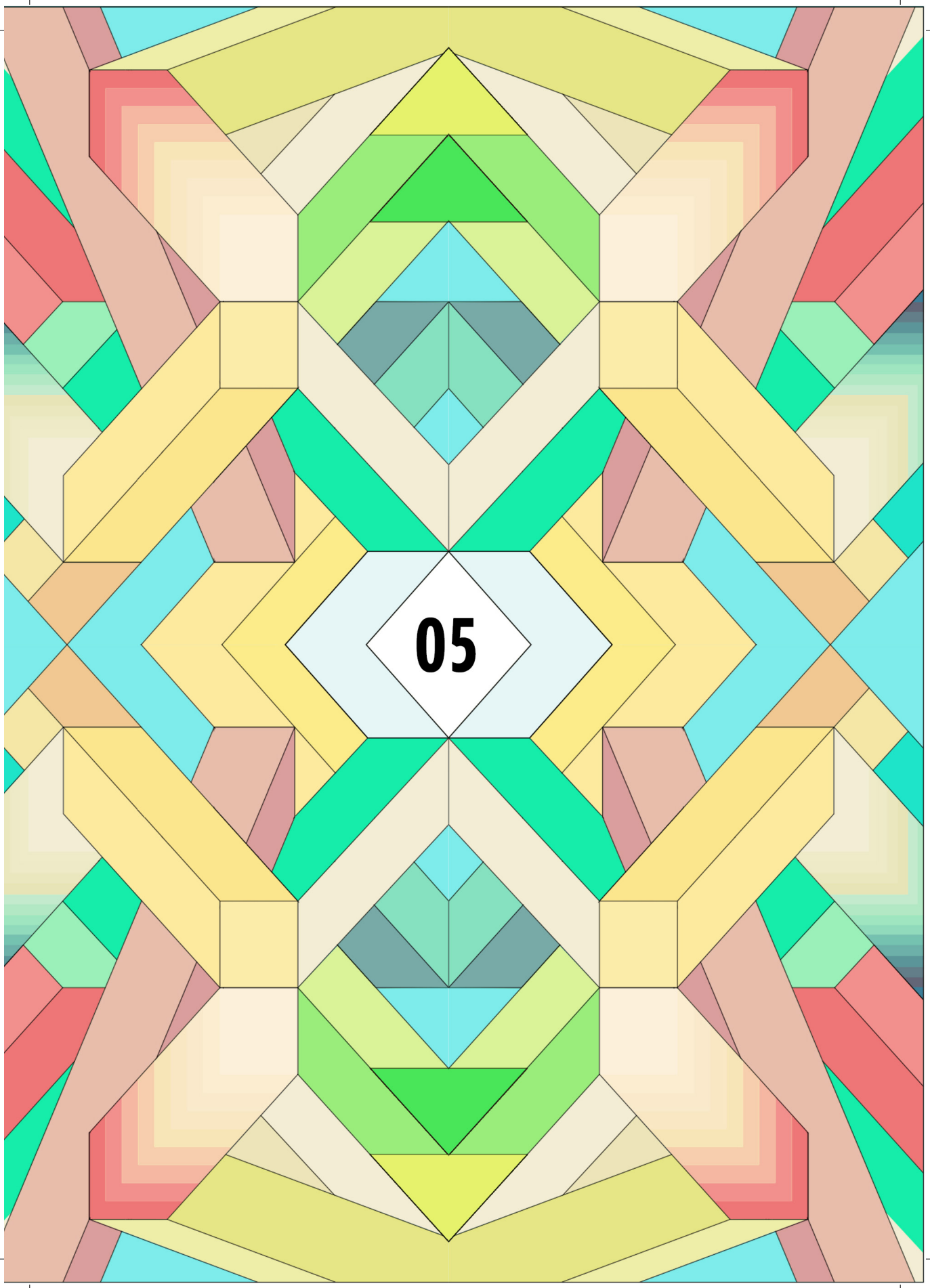
05

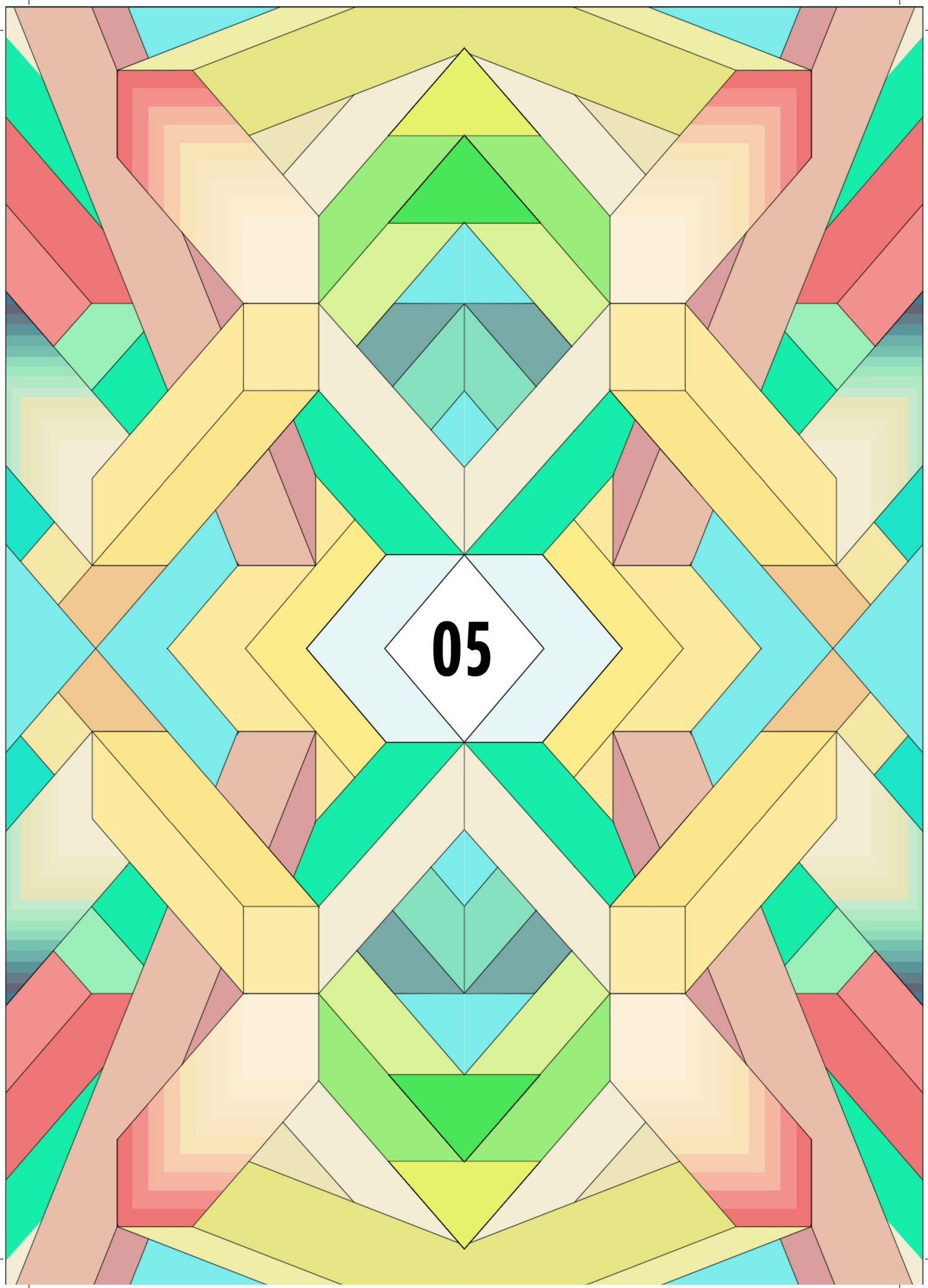
05

05

Summary, Concluding Remarks & Future Perspectives

Porous materials are of great importance to chemical industries because of the capability to react with molecules at their surfaces. Active carbon, alumina, titania, silica, and zeolites are important members of this family of functional porous materials. Their (possible) applications, such as gas separation, ion exchange and catalysis, are directly linked to how the (local) chemical composition as well as the size, shape and volume of the void space are distributed. This explains the worldwide efforts going on to synthesize new porous materials or modify the synthesis of existing porous materials. In the past two decades, Metal-Organic Frameworks (MOFs), which are highly crystalline and porous materials with a hybrid organic-inorganic compositional nature, have attracted a lot of attention. Zeolitic Imidazolate Frameworks (ZIFs) are an important sub-class of MOFs and are constructed from transition metals (e.g. Co^{2+} and Zn^{2+}) tetrahedrally coordinated to bridging imidazolates and its derivatives. In this PhD thesis, the main focus was devoted to the spectroscopy and microscopy on the formation of bulk as well as thin-films of ZIFs. In what follows, I will summarize the main findings of my research work, present some concluding remarks and provide some ideas for future research.

5.1 Summary

Understanding the synthesis of bulk ZIFs through the variation of the synthesis parameters is essential to alter their physicochemical and functional properties. In Chapter 2, the bulk synthesis of Co-ZIF-9 has been studied. The reported Co-ZIF-9 synthesis procedure by Park et al. yielded a secondary phase, namely cobalt formate. In order to circumvent this co-formation of cobalt formate we have developed an alternative synthesis recipe. More specifically, the phase-pure controlled synthesis of Co-ZIF-9 was carried out by a so-called pH adjustment method. The synthesized materials were characterized by a combination of UV-Vis, FT-IR and Raman spectroscopy as well as by TGA and XRD. The importance of the pH of the synthesis medium has been highlighted. An isostructural zinc variant of Co-ZIF-9, which is known as Zn-ZIF-7, was also synthesized in order to evaluate the formation of the secondary phase. In contrast to the Co-ZIF-9 case, a phase-pure Zn-ZIF-7 was obtained. The reason for the formation of a secondary phase in the case of Co-ZIF-9 could be related to the acid hydrolysis of the solvent N,N-dimethylformamide. A mechanism for the formation of this second phase was proposed, which was explained by the coordination flexibility of Co^{2+} ions. The crystal structures of Co-ZIF-9 and cobalt formate have been determined by single crystal X-ray crystallography and the resolved structures also reflected the coordination flexibility of framework cobalt ions. Figure 5.1 highlights the mains findings of Chapter 2.

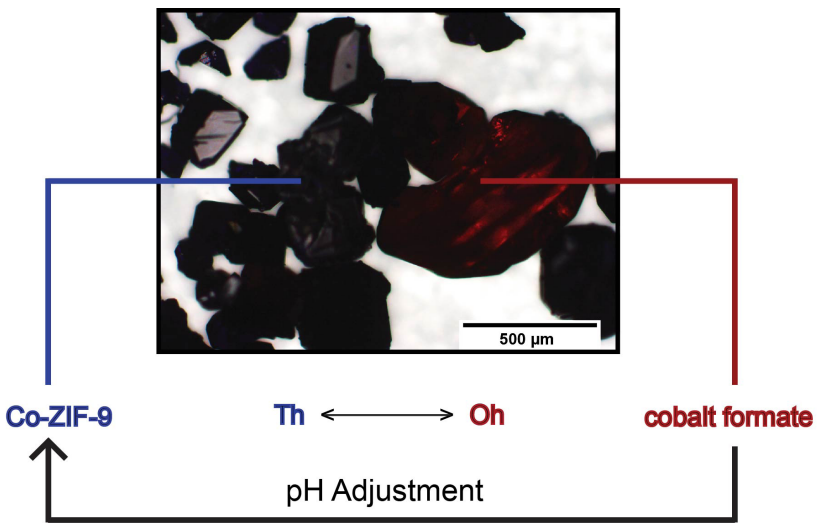

Figure 5.1. Schematic figure representing the pH adjustment method, which was used in Chapter 2, to synthesize phase-pure Co-ZIF-9.

In the next step of our study, as described in Chapter 3, we have focused on the synthesis of the so-called Surface-mounted metal-organic frameworks (SURMOFs).

SURMOFs are crystalline films of MOFs anchored onto a substrate and they have received significant amount of attention in the last decade. Direct growth from a mother liquor, assembly of preformed MOF crystals and step-wise layer-by-layer growth onto a substrate are the three main strategies reported for the preparation of SURMOFs in the literature. Synthesis of SURMOFs is of importance as it may give new insights into the formation principles of these crystalline porous materials.

In Chapter 3, we report on the experimental evidence of an inter-grown nature of surface-mounted thin-film of Zn-ZIF-8 (SURZIF-8). Two distinct samples have been prepared by the stepwise layer-by-layer liquid epitaxy method, namely 20 and 50 LBL cycle thin-films of Zn-ZIF-8, and subsequently characterized with multi-modal micro-spectroscopy. The detailed chemical imaging of these Zn-ZIF-8 thin-films was done with Raman micro-spectroscopy, while for the height information and the surface topology Atomic Force Microscopy (AFM) was used. In-depth analysis of the Raman mapping data and subsequent data analysis with PCA, revealed the existence of phase boundaries within the 20 cycles Zn-ZIF-8 sample, whereas the 50 LBL cycle Zn-ZIF-8 material is chemically much more homogeneous in nature, although still full of chemical heterogeneities. DFT calculations were conducted in order to calculate the molecular vibrations, helping to identify the observed shifts and intensity changes in the experimental vibrations on three model systems, namely linker (i.e., 2-methylimidazole) coordinated with two Zn^{2+}-ions, a protonated linker coordinated to one Zn^{2+}, and an isolated protonated linker (with no Zn^{2+}-ions coordinating to the linker). By the help of these assignments in four diagnostic spectral regions, we were able to identify several spectroscopic markers, indicative for the presence of defects sites. Raman bands which undergo spectral changes are diagnostic for the presence of these structural defects and can be used for spectral zoning and Raman mapping.

In Chapter 4, a combined AFM-vibrational spectroscopy research strategy is presented to investigate the chemistries governing the nucleation and growth of Zn-ZIF-8 and Co-ZIF-67 thin-films. This approach is illustrated in Figure 5.3. The influence of linker concentration, temperature and constituent metal (i.e., Zn^{2+} or Co^{2+}), on the nucleation and growth behavior of zeolitic imidazolate framework (Co-ZIF-67 and Zn-ZIF-8) thin-films was investigated by means of AFM, infrared spectroscopy and Raman spectroscopy. It was found that both the linker concentration and synthesis temperature have an influence on the nucleation and growth of thin-films of ZIFs. The obtained results demonstrate that Co-ZIF-67 has a higher nucleation and growth rate than Zn-ZIF-8 under identical synthesis conditions. This could be explained by the higher electronegativity of Co^{2+} compared to Zn^{2+}, leading to more polarized/ionic Co-N bonds relative to Zn-N. This has been observed in the Co/Zn-N

stretching vibration, where the Co-N vibrational band is blue shifted with 5 cm^{-1} relative to the Zn-N vibrational band. Both the particle size and thin-film coverage are the thin-film properties, which can be varied by changing the mentioned synthesis parameters. Furthermore, a multiple step direct deposition method was used for the preparation of thicker Co-ZIF-67 and Zn-ZIF-8 materials.

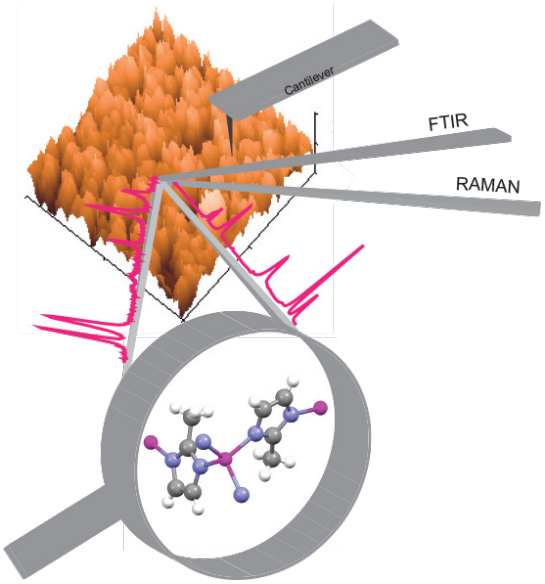

Figure 5.2. Schematic illustrating a combined AFM-vibrational spectroscopy strategy to investigate the nucleation and growth of Zn-ZIF-8 and Co-ZIF-67 thin-films.

5.2. Concluding Remarks & Future Perspectives

The field of metal organic frameworks (MOFs) thin-films, and its sub-family of ZIFs thin-films, possesses a lot of potential for increasing our fundamental understanding of materials synthesis and the related surface properties, which are created during the synthesis of these functional porous materials. Many new fabrication methods have been developed in the past years and most of these methods for the preparation of the thin-films stem from their bulk analogues. However, a detailed understanding of the chemistries governing the synthesis of ZIFs and their related thin-films is essential in order to 1) design new ZIFs with desired functionalities and 2) unlock their full potential for existing or new applications.

Chapter II deals with the bulk synthesis of ZIFs, whereas Chapters III and IV deal with thin-films of ZIFs. Chapter II provides insight into the effect of synthesis parameters, such as pH of the reaction medium and the coordination behaviour of the metal

ion, on the bulk synthesis through their detailed characterization by multiple spectroscopy and microscopy techniques. Instead, Chapters III and IV are related to the synthesis of ZIF thin-films through layer-by-layer and direct synthesis methods, respectively. In these two Chapters, a powerful combination of AFM and vibrational spectroscopy technique(s) was utilized. In Chapter III, a detailed data analysis of the Raman spectroscopy data was performed by PCA, while a vibrational spectroscopy data library was build up through DFT calculations. Consequently, new insights into the presence of defects sites through several spectroscopic markers were obtained. Chapter IV highlights the importance of the influence of synthesis parameters on thin-film properties, such as coverage/density, particle size and thickness as well as their influence on nucleation and growth for the thin-films as well as the impact of the coordination chemistry and flexibility of Co^{2+} and Zn^{2+}. These findings are of importance in the field of ZIF thin-film research and can enable to design ZIFs with desired properties and further unlock their full potential. To illustrate this point, thin-films constituted of particles with smaller/larger sizes could exhibit different diffusion properties for membrane applications. Furthermore, the structure-performance relationship can prove the importance of tailoring the synthesis of the thin-films, therefore testing these thin-films in certain fields, such as gas adsorption, is of great of importance.

As a future recommendation to extend our knowledge gained for the nucleation and growth of thin-films, in particular as a continuation of Chapter IV, time-resolved UV-Vis spectroscopy measurements should be used to provide insights into the early growth stages. This may bring new information on the table regarding the reaction kinetics taking place prior and during particle size formation, coordination sphere and particle formation. In-situ time-resolved Dynamic Light Scattering (DLS) experiments can be complementary to the in-situ UV-Vis spectroscopy findings in terms of rate of particle size formation and particle size distribution. Furthermore, pH monitoring during course of reaction at different linker concentrations and temperature ranges is another approach to provide additional information by correlating the deprotonation rate with the nucleation rate. Another parameter to investigate is the effect of reaction time during the growth of thin-films of MOFs through the direct synthesis method at reduced metal ion and linker concentrations, which can provide information on the early growth stages. As well as determination of the extent of crystallization at different reaction times, concentrations and temperatures for the investigation of the kinetics of crystal growth at both the bulk and thin-film scale.

For Chapter III, further investigation of synthesis parameters for LbL synthesis is required. In particular, there is a need for, more optimization regarding the metal

ion to linker concentrations, concentration of the SAMs, type of terminal group of SAMs, solvent, temperature and metal type. Furthermore, the synthesis of the isostructural cobalt variant of Zn-ZIF-8, namely Co-ZIF-67, through the LbL method allows for the comparison of their nucleation of growth behaviour and the influence of the transition metal ion on the kinetics of crystal growth. Here, it is clear that a more extended dataset could further shed light on the synthesis mechanism.

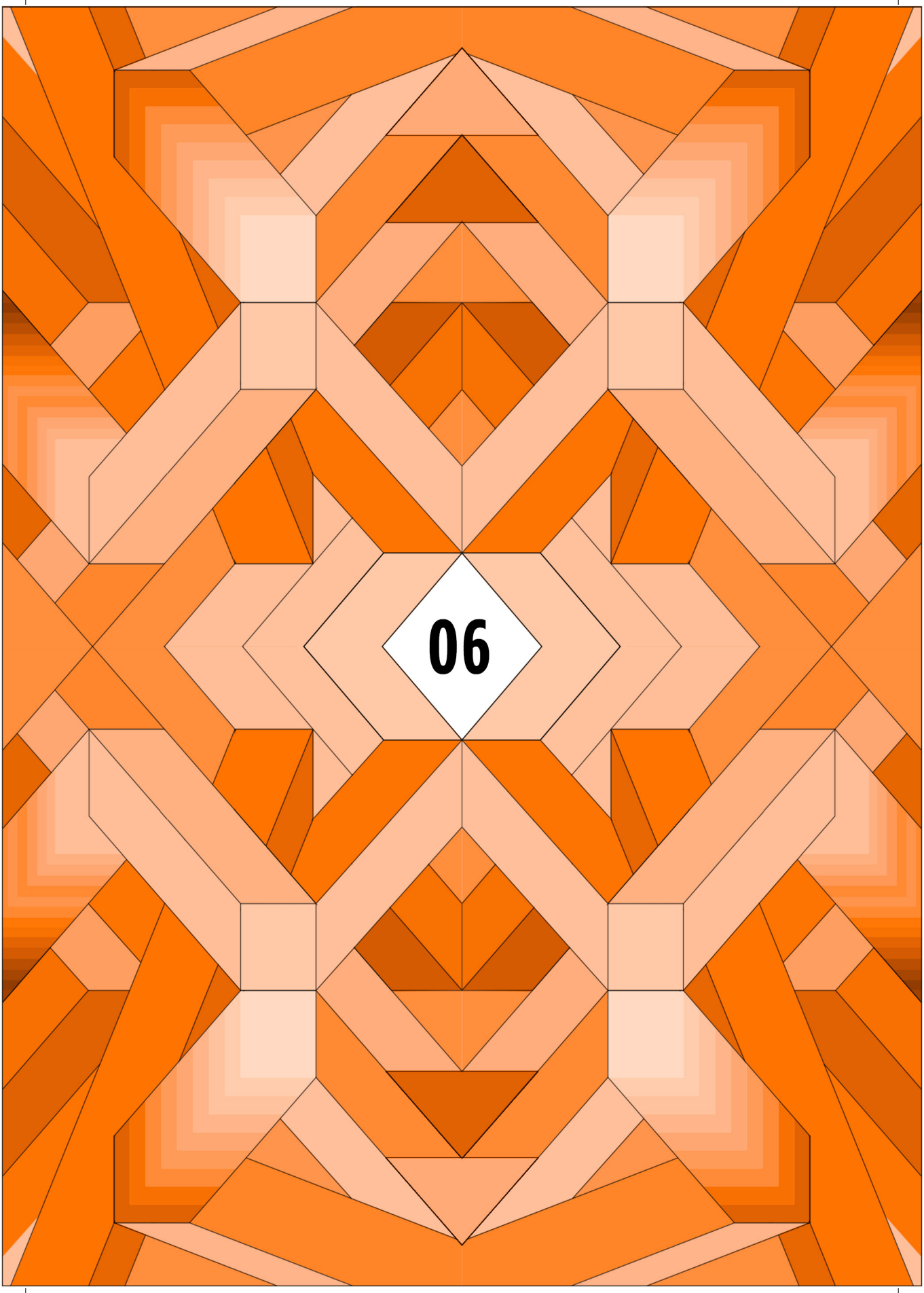
06

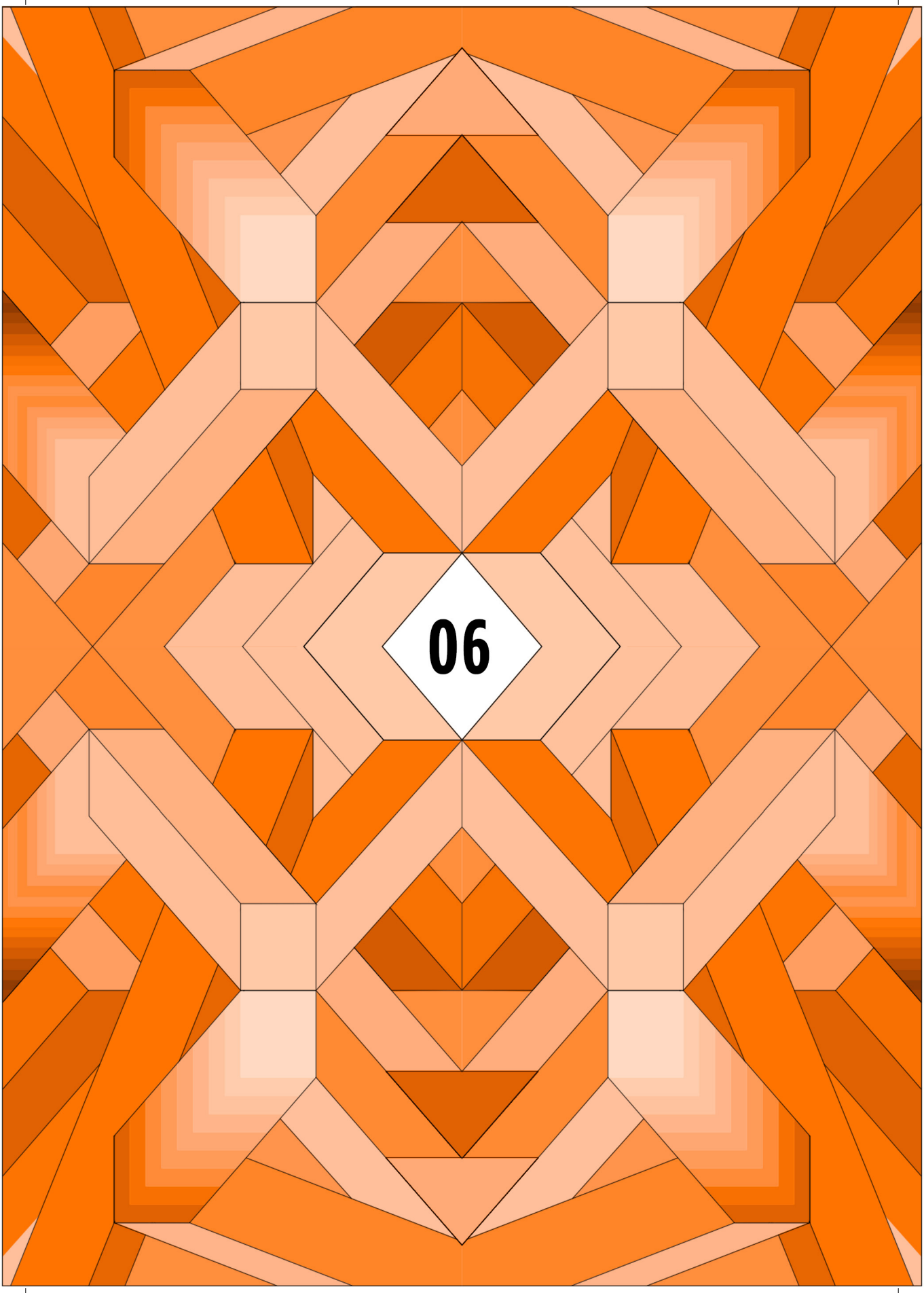
06

06

Nederlandse Samenvatting

Poreuze materialen zijn zeer belangrijk voor de chemische industrie omdat ze op hun oppervlak kunnen reageren met moleculen. Aktieve kool, aluminiumoxide, titaniumoxide en siliciumoxide zijn belangrijke leden van deze familie van functionele poreuze materialen. Hun (mogelijke) toepassingen, zoals gasscheiding, ionuitwisseling en katalyse zijn direct gerelateerd aan hoe de (lokale) chemische samenstelling, alsmede de grootte, vorm en volume van de lege ruimte zijn verdeeld. Dit verklaart de wereldwijde inspanningen om nieuwe poreuze materialen te maken of de synthese van bestaande poreuze materialen aan te passen. In de afgelopen twee decennia hebben Metal-Organic Frameworks (MOFs), materialen die kristallijn en poreus zijn met een hybride organische-anorganische samenstelling, veel aandacht getrokken. Zeoliet Imidazolaat Structuren (ZIFs) zijn een belangrijke subklasse van MOFs en zijn samengesteld uit overgangsmetalen (zoals Co^{2+} en Zn^{2+}) die tetraedrisch gecoordineerd zijn met overbruggende imidazolaatmoleculen of moleculen afgeleid van imidazolaat. Het vakgebied van Metal-Organic Frameworks (MOFs) dunne laag materialen en de subklasse van ZIF-dunne laag materialen bied veel potentie om ons fundamenteel begrip van materiaalsynthese en de hieraan gerelateerde oppervlakte-eigenschappen uit te breiden. Echter, de meeste methodes voor de synthese van dunne laag materialen zijn afgeleid van synthese methodes voor bulk equivalenten. Om nieuwe dunne laag ZIF materialen met de gewenste functionaliteiten te ontwikkelen en optimaal toe te passen, is gedetaileerd en fundementeel begrip van de relevante chemie essentieel.

6.1 Samenvatting

In deze PhD thesis is de meeste aandacht gewijd aan de spectroscopie en microscopie van de vorming van ZIF kristallen, zowel in bulk als voor dunne laag materialen. Hoofdstuk 2 bespreekt de bulk synthese van ZIF materialen. Dit hoofdstuk biedt inzicht in het effect van verschillende synthese parameters op de bulksynthese, zoals de pH van de synthesemedium en het coordinatiegedrag van het metaalion. Dit inzicht wordt verkregen door een gedetaileerde karakterisering met meerdere spectroscopische en microscopische technieken. Er is hierbij specifiek naar de synthese van Co-ZIF 9 gekeken. De door Park *et al*. gerapporteerde Co-ZIF-9 syntheseprocedure leverde een tweede component in het eindproduct op, namelijk kobaltformaat. Om de vorming van dit ongewenste component te voorkomen, hebben wij een alternatief syntheserecept ontwikkeld. De gecontroleerde synthese van zuiver Co-ZIF-9 is uitgevoerd door middel van een zogenaamde pH aanpassingsmethode. Het belang van de pH van het synthesemedium is hierbij onderstreept. Een zinkvariant met dezelfde structuur als Co-ZIF-9, ook wel bekend als Zn-ZIF-7, is gesynthetiseerd volgens dezelfde procedure om de vorming van secundaire componenten te kunnen beoordelen. In tegenstelling tot Co-ZIF-9 is voor zink wel zuiver Zn-ZIF-7 verkregen. De reden voor de vorming van een tweede component in het geval van kobalt zou gerelateerd kunnen zijn aan de zuurhydrolyse van het oplosmiddel. Wij hebben een mechanisme voor de vorming van deze tweede component voorgesteld, waarin de flexibiliteit van de coordinatiesfeer van Co^{2+} ionen de oorzaak is van de vorming van kobaltformaat.

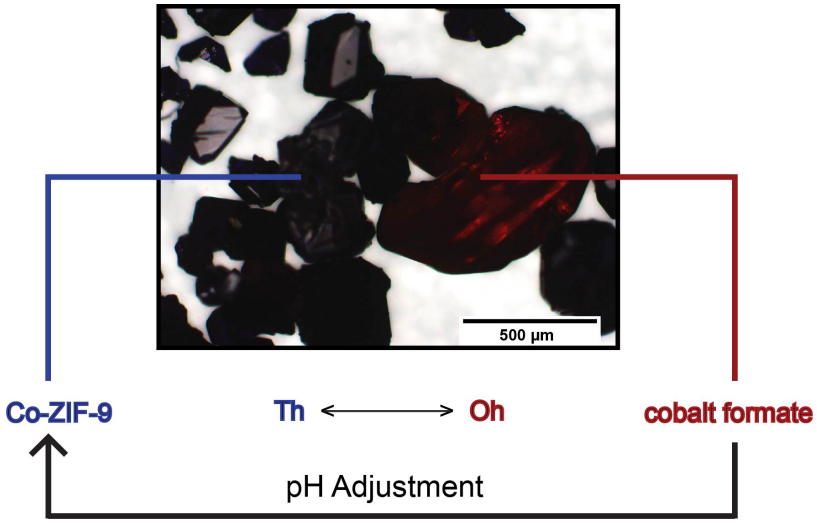

Figure 6.1. Dit schematische figuur laat de pH aanpassingsmethode zien die gebruikt is in Hoofdstuk 2 om zuiver Co-ZIF-9 te maken.

In een volgende stap in deze studie, zoals beschreven in Hoofdstuk 3, hebben we de focus gelegd op het maken van zogenaamde oppervlakgebonden metal-organic frameworks (SURMOFs). Een SURMOF is een kristallijne dunne laag van MOFs, die gebonden zijn aan een substraat. Het laatste decennium is er veel interesse voor deze materialen. Directe groei vanuit de vormingsoplossing, het aanbrengen van voorgevormde MOF kristallen en de stapsgewijze, laag-voor-laag groei op het substraat zijn de drie belangrijkste strategieën, die gerapporteerd zijn in de literatuur voor het maken van SURFMOFs. De synthese van SURMOFs is interessant om te onderzoeken aangezien het nieuwe inzichten kan geven in de vormingsprincipes van deze kristallijne poreuze materialen. In het geval van Zn-ZIF-8 (SURZIF-8) rapporteren we de samengroeiing van oppervlakgebonden SURZIF-8 tot een dunne laag, onderzocht met een diepgaande analyse van Raman micro-spectroscopie en bijhorende Hoofdcomponenten Analyse (PCA, of *Principal Component Analysis*, in de Engelse taal). Hiermee laten we het bestaan van fase overgangen zien voor een lage oppervlakte belading, terwijl voor hoge beladingen het oppervlak chemisch veel homogener is. *Density Functional Theory* (DFT) is gebuikt om de moleculaire vibraties te berekenen, hetgeen helpt om de geobserveerde verschuivingen en intensiteitsveranderingen in de Raman vibraties te identificeren. Drie modelsystemen werden hiermee bestudeerd, namelijk de brug (in dit geval 2-methylimidazol) gecoördineerd met 2 Zn^{2+}ionen, een geprotoneerde brug gecoördineerd met 1 Zn^{2+}, en een geïsoleerde geprotoneerde brug (zonder Zn^{2+}). Met de hulp van de toewijzingen van deze modelsystemen waren wij in staat verschillende spectrale *markers* te identificeren die indicatief zijn voor de aanwezigheid van defecten in het ZIF kristal.

Hoofdstuk 4 belicht het belang van de syntheseparameters op de eigenschappen van het resulterende dunne laag ZIF materiaal. Een aantal eigenschappen, zoals de oppervlaktedichtheid, deeltjesgrootte en laagdikte van de ZIF kristallen blijken cruciaal voor de uiteindelijke eigenschappen van het materiaal. Dit biedt de mogelijkheid om materialen met specifieke eigenschappen te ontwerpen. Door bijvoorbeeld de deeltjesgrootte te varieren, kan de diffusie door een ZIF membraan gevarieerd worden. Inzicht in de synthese wordt in ons geval verkregen door de chemie die plaatsvindt tijdens de nucleatie en groei van dunne laag kristallen van Zn-ZIF-8 en Co-ZIF-67 te bestuderen met gecombineerde AFM-vibratiespectroscopie. Hierbij is de invloed van de brugmolecuul concentratie, temperatuur en metaal (*i.e.* Zn^{2+} of Co^{2+}) op het nucleatie- en groeigedrag van dunne kristallagen van zeolitische imidazolaat frameworks (Co-ZIF-67 en Zn-ZIF-8) onderzocht door middel van AFM, IR spectroscopie en Raman spectroscopie. Het bleek dat zowel de brugmolecuul concentratie als de synthesetemperatuur een invloed hebben op de nucleatie en groei van dunne lagen van ZIFs. De gevonden resultaten laten zien dat Co-

ZIF-67 een hogere nucleatie en groeisnelheid heeft dan Zn-ZIF-8 onder identische synthesecondities. Dit kan verklaard worden door de hogere electronegativiteit van Co^{2+} vergeleken met Zn^{2+}. Zowel de deeltjesgrootte als de bedekkingsgraad van de dunne laag bepaalt de eigenschappen van de dunne laag, hetgeen gevarieerd kan worden door de hiervoor genoemde syntheseparameters te veranderen. Daarnaast is ook een meerdere-staps directe depositiemethode gebruikt om dikkere Co-ZIF-67 and Zn-ZIF-8 materialen te maken. Door dit niveau van controle over de synthese, kan inzicht verkregen worden in de relatie tussen de structuur en het gedrag van het materiaal.

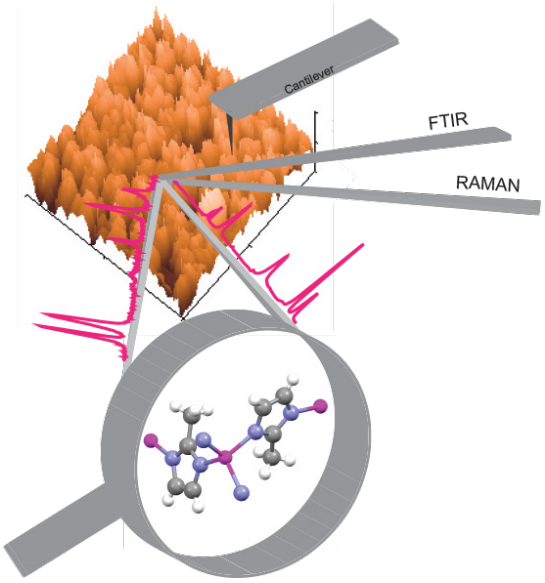

Figure 6.2. Schematische illustratie van de gecombineerde AFM-vibratiespectroscopie om de nucleatie en groei van dunne lagen van Zn-ZIF-8 en Co-ZIF-67 te onderzoeken.

6.2. Conclusies & Toekomstperspectief

Het vakgebied van *Metal-Organic Frameworks* (MOFs) dunne laag materialen en de subklasse van ZIF-dunne laag materialen biedt veel potentie om ons fundamenteel begrip van materiaalsynthese en de hieraan gerelateerde oppervlakte-eigenschappen uit te breiden. De laatste jaren zijn er veel nieuwe methodes voor de bereiding van dit soort materialen ontwikkeld. De meeste van deze methodes voor de synthese van dunne laag materialen zijn afgeleid van bereidingsmethodes voor bulk analogen. Gedetaileerd, fundamenteel begrip van de relevante chemie is echter essentieel om nieuwe ZIF materialen met de gewenste functionaliteiten te ontwikkelen en om optimaal gebruik te maken van deze materialen voor bestaande

of nieuwe toepassingen.

Hoofdstuk 2 bespreekt de bulk synthese van ZIF materialen. Dit hoofdstuk biedt inzicht in het effect van verschillende synthese parameters op de bulk synthese, zoals de pH van de synthesemedium en het coordinatiegedrag van het metaal ion. Dit inzicht wordt verkregen door een gedetaileerde karakterisering met meerdere spectroscopische en microscopische technieken. In Hoofdstukken 3 en 4 wordt er gekeken naar respectievelijk laag-voor-laag en directe synthese methodes voor dunne film ZIF materialen. Hierbij wordt er gebruik gemaakt van de krachtige combinatie van AFM en vibratiespectroscopie. In Hoofdstuk 3 is een gedetaileerde analyse van Raman spectroscopische data uitgevoerd met behulp van PCA. Hiernaast is er door middel van DFT berekeningen een bibliotheek voor vibratiespectroscopische frequenties opgebouwd. Deze additionele analysemethodes en de daaruit volgende spectroscopische *markers* hebben geleid tot nieuwe inzichten in de aanwezigheid van defecten in de ZIF kristallen. Hoofdstuk 4 belicht het belang van de syntheseparameters op de eigenschappen van het resulterende dunne laag materiaal. Een aantal eigenschappen, zoals de oppervlaktedichtheid, deeltjesgrootte en laagdikte van de ZIF kristallen blijken cruciaal voor de uiteindelijke eigenschappen van het materiaal. Deze bevindingen zijn van belang voor het vakgebied van ZIF dunne laag synthese en bieden de mogelijkheid om materialen met specifieke eigenschappen te ontwerpen. Door bijvoorbeeld de deeltjesgrootte te varieren, kan de diffusie door een ZIF membraan gevarieerd worden. Daarnaast kan door meer controle over de synthese, inzicht verkregen worden in de relatie tussen de structuur en het gedrag van het materiaal.

In de toekomst moeten we onze kennis op het gebied van nucleatie en groei van dunne films verder uitbreiden. Met name tijdsafhankelijke UV-Vis spectroscopie, zoals beschreven in Hoofdstuk 4, zouden meer inzicht kunnen verschaffen in de eerste groeifase van de kristallen. Dit zou met nieuwe informatie verschaffen over de reactiekinitiek voor en tijdens de vorming van de deeltjes en de coordinatie om de metaal centra. Hierbij kan in-situ *Dynamic Light Scattering* (DLS) gemeten tijdens de reactie de bevindingen ondersteunen met betrekking tot de snelheid van deeltjesgroei en de deeltjesgrootte verdeling. Daarnaast kan het volgen van de pH tijdens reacties met verschillende concentraties van brugmoleculen en verschillende temperaturen meer inzicht geven in de correlatie van de snelheid van deprotonatie met de snelheid van nucleatie. Door de tijd waarin de dunne laag is toegestaan te groeien te varieren, kan meer informatie verkregen worden over de initiele groei van de kristallen. Dit kan tijdens de directe synthese gedaan worden door bij lagere concentraties van het metaal ion en het brugmolecuul te meten.

Verder onderzoek naar de synthese parameters voor de laag-voor-laag synthese is vereist. Hierbij moet de verhouding van de metaal ion en brugmolecuul concentraties geoptimaliseerd worden. Daarnaast spelen ook de concentratie van de *Self-Assembled Monolayer* (SAMs), het soort eindgroep op de SAMs, het oplosmiddel, de temperatuur en het metaal een rol. Door middel van de directe vergelijking van kobalt en zink ZIF materialen met dezelfde structuur kan inzicht verkregen worden in het nucleatie- en groeigedrag van dit soort materialen. Het is hierbij duidelijk dat een uitgebreidere dataset meer inzicht zal bieden in het mechanisme.

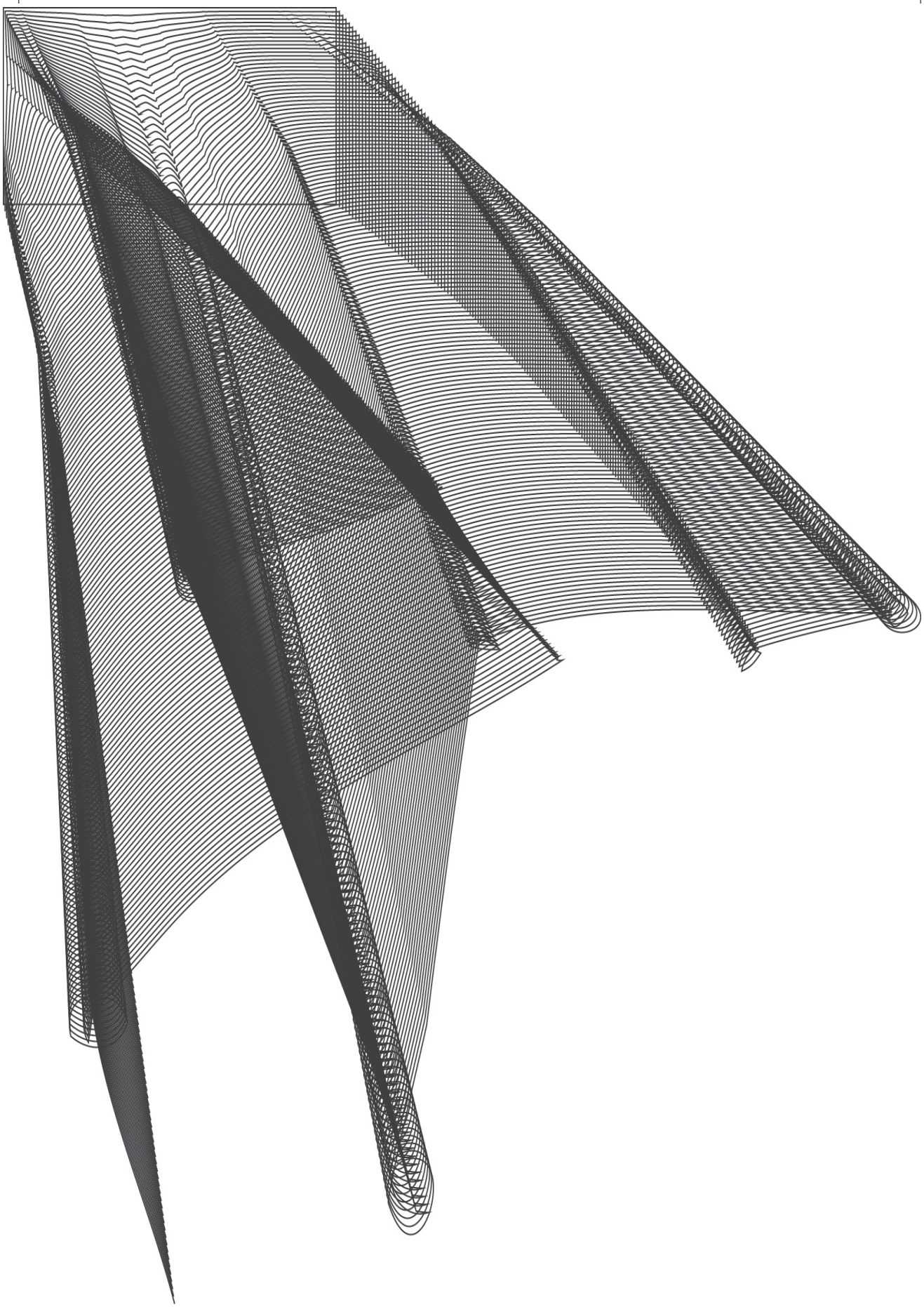

List of Abbreviations

AFM	atomic force microscopy
BDC	benzene-1,4-dicarboxylate
BET	Brunauer-Emmet-Teller
BTC	benzenetricarboxylate
CIF	crystallographic information file
COF	covalent organic framework
DMF	N-N-dimethylformamide
DRIFTS	diffuse reflectance infrared Fourier transform spectroscopy
ESI-MS	electrospray ionization mass spectrometry
FIB-SEM	focus ion beam scanning electron microscopy
FT-IR	Fourier-transform infrared
HKUST-1	Hong Kong University of Science and Technology-1
Im	imidazole
LB	Langmuir-Blodgett
LbL	layer-by-layer
m	medium
M	metal
MOF	metal organic framework
PCA	principal component analysis
PCP	porous coordination polymer
QCM	quartz crystal microbalance
s	strong

SAM	self-assembled monolayer
SAXS	small angle X-ray scattering
SBA-15	Santa Barbara amorphous type material no 15
SBU	secondary building unit
SEM	scanning electron microscopy
SLS	static light scattering
SOD	sodalite
SURMOF	surface mounted metal organic framework
TEM	transmission electron microscopy
TGA	thermogravimetric analysis
UV-Vis	ultraviolet-visible
vw	very weak
w	weak
WAXS	wide angle X-ray scattering
XRD	X-ray diffraction
ZIF	zeolitic imidazolate framework
ZSM-5	zeolite socony mobil-5

SCIENTIFIC PUBLICATIONS AND CONFERENCE PRESENTATIONS

SCIENTIFIC PUBLICATIONS

Chapter II

Z. Öztürk, J. P. Hofmann, M. Lutz, M. Mazaj, N. Z. Logar, and B. M. Weckhuysen, "Controlled Synthesis of Phase-Pure Zeolitic Imidazolate Framework Co-ZIF-9" *Eur. J. Inorg. Chem.* **2015**, 1625–1630.

Chapter III

Z. Öztürk, R. P. Brand, J. Boereboom, F. Meirer, and B. M. Weckhuysen, "Vibrational Fingerprinting of Defects Sites in SURZIF-8 Thin-films", *in preparation.*

Chapter IV

Z. Öztürk, M. Filez, and B. M. Weckhuysen, "Decoding Nucleation and Growth of Zeolitic Imidazolate Framework Thin-Films with Atomic Force Microscopy and Vibrational Spectroscopy" *Chem. Eur. J.* **2017**, 23, 10915-10924.

Other scientific publications

L. Wu, N. Y. Dzade, Lu Gao, D. O. Scanlon, Z. Öztürk, N. Hollingsworth, B. M. Weckhuysen, E. J. M. Hensen, N. H. de Leeuw, and J. P. Hofmann, "Enhanced Photoresponse of FeS_2 Films: The Role of Marcasite–Pyrite Phase Junctions" *Adv. Mater.* **2016**, 28, 9602–9607.

Z. Öztürk, F. Sen, S. Sen, and G. Gokagac, "The preparation and characterization of nano-sized Pt–Pd/C catalysts and comparison of their superior catalytic activities for methanol and ethanol oxidation" *J. Mater. Sci.* **2012**, 47, 8134–8144.

CONFERENCE PRESENTATIONS

The Netherlands' Catalysis and Chemistry Conferences

Z Öztürk, and B. M. Weckhuysen, "Differences in the Growth Rates of Zn-ZIF-8 and Co-ZIF-67 Thin-films Grown through Direct Synthesis"

Noordwijkerhout, The Netherlands, March **2016 [oral]**

Z Öztürk, and B. M. Weckhuysen, "Preparation and Characterization of Surface-mounted Co-ZIF-67"

Noordwijkerhout, The Netherlands, March 2**015 [poster]**

Z Öztürk, J. P. Hofmann, M. Lutz, M. Mazaj, N. Zabukovec Logar, and B. M. Weckhuysen, "Synthesis of Phase-pure Zeolitic Imidazolate Framework Co-ZIF-9 and its Implications on Catalysis"

Noordwijkerhout, The Netherlands, March **2014 [poster]**

Netherlands Research School Combination-Catalysis (NRSCC) Workshops

Z Öztürk, and B. M. Weckhuysen, "Preparation and Characterization of Surface-Mounted Metal Organic Frameworks"

Utrecht, The Netherlands, February **2015 [oral]**

Z Öztürk, J. P. Hofmann, M. Lutz, M. Mazaj, N. Zabukovec Logar, and B. M. Weckhuysen, "Synthesis of Phase-pure Zeolitic Imidazolate Framework Co-ZIF-9 and its Implications on Catalysis"

Utrecht, The Netherlands, February **2014 [oral]**

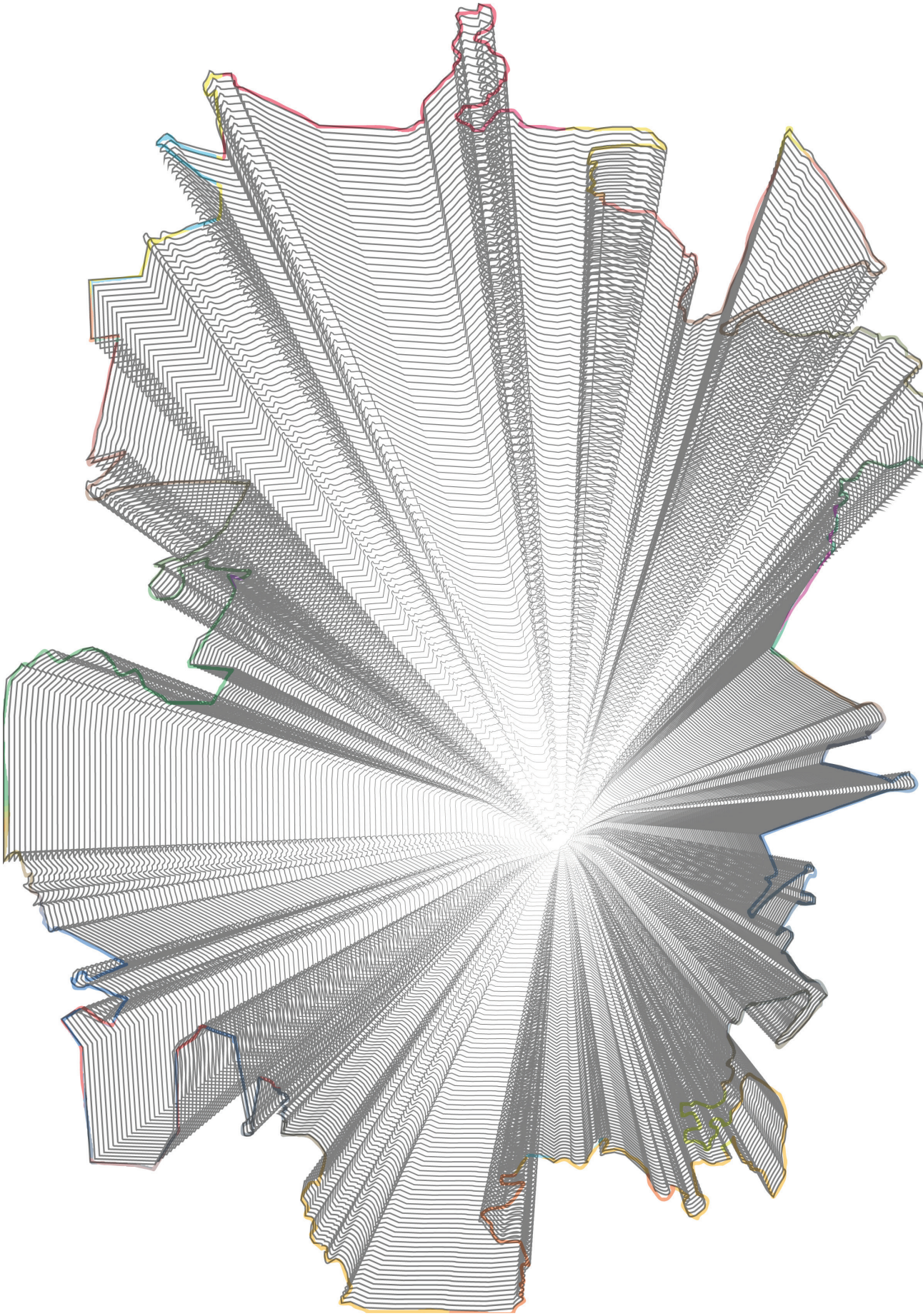

ACKNOWLEDGEMENTS

This has been a long journey for me to reach this day, the completion of this PhD book, and there are many people that supported me in different aspects during the last five years and I owe them a debt of gratitude.

Above all, I would like to thank my promoter **Professor Bert Weckhuysen**. **Bert**, thanks a lot for giving me the opportunity to be a part of this amazing research group with advanced facilities and to work with you. I had a rough start with this new research topic of MOFs in the group, and I sincerely appreciate all the collaborations with Ljubljana and Bochum that you arranged in the first year of my PhD in order to get me dive into this new field of research for the group. During my PhD time, I haven't been the luckiest in terms of health concerns and I had a very severe spinal hernia in the first year of my PhD and I wasn't able to work almost for a year. Thanks a lot for all the motivation and support during this period, it meant a lot to me and your caring approach made this transition of getting back to work much easier. From you, I learnt how to get the maximum out of my research work, how to do result-oriented experiments and how to write the work down and present them in the best way. I really would like to thank you for all your guidance and true patience through my PhD period, which contributed a lot to both my scientific and professional development and now I am completing my PhD with an invaluable experience for life.

The scientific content described in this PhD thesis would not be possible without help of numerous colleagues and collaborators. I would like to thank **Dr. Jan Philipp Hofmann** for all his support and guidance especially in the first year of my PhD. **Jan Philipp**, you made my start and adaptation to the group really faster and I have learnt how to develop different approaches in my research and data interpretation. Thanks a lot for joining me in Ljubljana and Bochum and your presence made these collaborations much more proficient. All the fruitful discussions and skype meetings after you have left the group helped me a lot to further shape my research. Besides work, thanks a lot for all the drinks, lunches, dinners in and travelling to Utrecht, Grenoble, Ljubljana and Bochum, those were great memories. I wouldn't continue without mentioning **Dr. Matthias Filez**. **Matthias**, I am thankful for all the support, motivation, input and guidance in the last year of my PhD thesis. I really learnt a lot regarding the data processing and related analysis. Thank you very much for performing additional experiments, which was beneficial for the completion of Chapter IV. It was also a great pleasure for me to work with you, **Dr. Florian Meirer**. **Florian,** I would like to thank you for your help and useful discussions. Your input in Chapter III in terms of data analysis was a great of importance. Here, I would like

to acknowledge **Jelle Boereboom**, my colleague PhD student in the group, for his computational contribution to the same chapter.

As mentioned before, I had the chance to be a visiting PhD researcher in Ljubljana and Bochum. I would like to thank to **Professor Nataša Zabukovec Logar** from the National Institute of Chemistry in Ljubljana (Slovenia). It was a great pleasure for me to be able to work with you. Thanks a lot for all the guidance; this has helped me to develop a better understanding of the crystal structures of MOF materials. Your research group was an amazing host (**Matjaz**, **Alenka** and **Tadeja**), thanks for all the useful arrangements and priorities that you gave to my own research. Besides, many thanks for being such a caring and down-to-earth person as you picked me up from the airport, even filled the fridge with all the basic foods, drove us around, took us out for wonderful dinners. Thanks a lot for everything. I would also like to thank to Professor **Roland Fischer** and Dr. **Rochus Schmid** from Ruhr University Bochum (Germany) for visiting their labs. Thanks a lot **Angelique**, **Min Tu** and **Suttipong** for sharing your knowledge and expertise in the thin-film research.

Dymph and Monique, there are no words to thank you for all the help, arrangements and support as well as your welcoming attitude. **Monique,** I am truly thankful for all the support, advice and help during the period of my sickness, it really means a lot to me. **Emke**, **Iris**, and **Ines**, I appreciate your help and professionalism during my PhD period. **Ad^{E}**, **Ad^{M}**, **Marjan**, **Fouad**, **Pascal** and **Oscar** thank you for the assistance with many inquiries during this period. In particular, **Fouad** and **Peter de Peinder**, thanks a lot for the help during DRIFT spectroscopy measurements.

I would like to thank to former AFM-Raman folks, **Clare, Evelien** and **Rogier**. Working with you was a delight and in particular, I would like to thank my friend and colleague PhD student **Rogier Brand**. **Rogier**, we worked in the same project throughout our PhDs and we share a mutual Chapter. Your expertise in AFM-Raman spectroscopy was of great value to make this work a success. Thanks a lot for the AFM teaching sessions, technical support, fruitful discussions, and most importantly for your friendship. We both struggled during this period and I am sure you are going to make it as well to the finish line. I will be there for you whenever you need help. Good luck with the completion of your PhD thesis. The current squad of AFM-Raman team needs a referral here; **Katinka**, **Thomas**, **Laurens** and **Guusje**, all the best of luck in your own research work.

Working in the Inorganic Chemistry and Catalysis group was an incredible experience with all the advanced characterization tools available. In addition to these instrumental capabilities, the inorganic chemistry and catalysis group has an amazing working athmosphere, which is created by numerous colleagues from different technical and cultural backgrounds. Here is a list of people that I had a

chance to meet and work with: **Abhishek**, **Ad^{E}**, **Ad^{M}**, **Angeloclaudio**, **Ana**, **Andy**, **Anne Mette**, **Anne-Eva**, **Annelie**, **Anton**, **Antonio**, **Ara**, **Arjan**, **Arjen**, **Baira**, **Bart**, **Beatriz L.**, **Beatriz S.**, **Bert**, **Boyang**, **Carlo**, **Carlos**, **Carolien**, **Cedric**, **Charlotte**, **Christa**, **Christoph**, **Clare**, **Daniel**, **Diego**, **Dilek**, **Donglong**, **Dymph**, **Eelco**, **Egor**, **Elena**, **Emke**, **Emma**, **Evelien**, **Fang**, **Fernando**, **Fiona**, **Florian**, **Fouad**, **Frank dG**, **Frank H**, **Gang**, **Gareth**, **Gonzalo**, **Guusje**, **Hans**, **Harry**, **Hebatalla**, **Hendrik**, **Herrick**, **Hirsa**, **Homer**, **Ilona**, **Ilse**, **Ines Uno**, **Ines Dos**, **Inez**, **Inge**, **Iris**, **Ivan**, **Jan**, **Jan Philipp**, **Jan Willem**, **Jamal**, **Javi**, **Jelle**, **Jens**, **Jesper**, **Jeroen**, **Jessi**, **Jinbao**, **Jochem**, **Joe**, **Joe Z**, **Joel**, **Joris**, **Jose**, **Jovana**, **JX**, **Karst**, **Katarina**, **Katinka**, **Khaled**, **Koen**, **Korneel**, **Krijn**, **Lars**, **Laurens**, **Leila**, **Lennart**, **Lisette**, **Luis**, **Maarten**, **Mahnaz**, **Manuel**, **Marianna**, **Mario**, **Marjan**, **Marleen**, **Marjolein**, **Mark**, **Martin**, **Matthew**, **Matthias**, **Matti**, **Michal**, **Miguel**, **Mita**, **Monica**, **Monique**, **Mozzafar**, **Mustafa**, **Nazila**, **Nynke**, **Oscar**, **Ozgun**, **Pascal**, **Pasi**, **Patric**, **Pengfei**, **Peter B**, **Peter H**, **Peter M**, **Peter N**, **Peter dP**, **Peter S**, **Petra**, **Pierre**, **Pieter B**, **Pieter M**, **Qingyun**, **Rafael**, **Ramon**, **Remco**, **Rien**, **Rob**, **Robin**, **Rogier**, **Rolf**, **Rosa**, **Roy**, **Ru-Pan**, **Sam**, **Sander**, **Sandra**, **Sang-Ho**, **Sankar**, **Selvedin**, **Silvia**, **Sophie**, **Stanislav**, **Stefan**, **Suwarno**, **Suzanne**, **Tamara**, **Tao**, **Thomas E**, **Thomas vH**, **Thomas H**, **Ties**, **Tom D**, **Tom vD**, **Upakul**, **Wenhao**, **Wouter L**, **Ying**, **Yuen** and **Zoki**. I would like to thank you all for the collaborations, borrels, coffee breaks, work discussions, talks, conferences, very interesting Debye lunch lectures, DO days, Debye spring schools, labuitjes, dinners, parties, nights out and sports events.

Moving to another country where I have met numerous amazing people was also coming with the fact that I was leaving behind my dear friends back home. **Ayşegül**, **Coşkun**, **Ercan**, **Mehmet, Nihan**, **Özge**, **Seda**, **Tuğba** and **Zeynep,** I would like to thank you all for proving that distance is not a real obstacle for keeping the connection and remembering all those great years we had together. **Aysegül**, **Çınar**, **Mehmet**, and **Seda**, thanks for the support, motivation and the great times both in Ankara and in Amsterdam. **Zeynep**, **Mert** and **Coskun**, thanks for being there whenever I need you guys. **Nihan**, **Çağan** and **Ercan**, your visit to Utrecht was amazing and thanks for all the good times and memories. During these years, I couldn't visit Turkey often due to many problems and couldn't witness the amazing moments (e.g., weddings and births) you had guys. I will try to visit you often and make the new members of your family get familiar with their Zafer uncle. **Tuğbam, Zoscum, Ercüm, and Ayşegülüm** your friendship, support, motivation and help whenever I need was there and it means a lot to me. Thanks a lot for being my friends and your trip to Utrecht for my birthday was an amazing motivation and support for me when it was needed most. Love you all!

The friends back in Turkey and throughout the world, thanks for all the great moments. **Bariş**, **Ebrusan**, **Burcusan**, **Feruş**, **Tolga**, **Merve**, **Rukan**, **Tuğce**, **Huriye**,

Kaan, **Lilim Tilim**, **Tugba O.**, **Inga**, **Nastya**, **Cansu**, **Willem**, **Federico**, **Gül**, **Neriman**, **Cobus**, **Heekyung**, **Gamze**, **Zeynep** and **Alex**. **Inga** thanks for being such a positive and fun person. We had too many laughs during the trips in the Netherlands, Belgium and France. Heekyung, thank you very much for designing the inner separator pages of my thesis and all the nice chats and drinks as well. **Bariş**, my old friend, I am so glad our roads crossed again after many years. Thanks for all the support and laughs bro. **Ebrusancim**, **Lilim Tilim**, **Ferusum** and **Rukan** a.k.a **Osmannn**, thanks for being there whenever needed in particular **Rukan**, your visit to Utrecht and Amsterdam was so much fun, thanks. **Willem**, my true friend, thanks for all the support, drinks, lunches, dinners and laughs. **Neriman**, my beautiful friend with a great heart; thanks for all the great memories. I can't wait to meet with you, **Cobus** and your beautiful baby girl **Luna** in South Africa. **Zeynepim Öktemim**, your friendship and support mean a lot to me. Thanks for being there especially in the last period of my PhD my true friend; we had too many great memories together with **Gül**, **Isin K.** and **Sezen A.**. Let's gather more and more memories!

My Turkish diaspora in my second home Utrecht, you guys made it feels like a real home for me as well. **Ali P.**, **Ali O'Haydn**, **Deniz**, **Doğal**, **Fikret**, **Giray**, **Müge**, **Sema, Zeynep A. B.,** thanks for all the support and laughs that we had together. Your presence made this journey much nicer and softer. **Ali O'Haydn** thanks for all the support and fun moments; I am so glad that our roads crossed here in Utrecht. **Deniz**, you are a big inspiration for me and thanks a lot for being there and supporting me during this period. Let's keep the good vibes and connection as we will have much more memories together. **Doğal**, you have a very big heart and thanks for letting me get into your life. We had many drinks, dinners, night outs and laughs together. Thanks for the amazing dinners at abrikoos. **Fikret** and **Giray**, thanks a lot for the fun moments, game nights, long deep talks and designing my cover page. **Sema**, thanks for all the positive attitude and friendship during the last year of my PhD. **Zeynep A. B.**, I am so glad that we met and your caring and supporting approach helped me a lot, thanks for everything. Good luck in the completion of your PhD thesis. Special thanks go to my paranimfs **Ali P.**, and **Müge** who are my safe haven. **Ali P.**, my dear **bidikopolous**, thanks for being such a caring, smart, funny, strong and real friend. Whenever I feel like falling down, you were always there to hold me and make me stand up. I have learnt a lot from you, your support and friendship means a lot to me. **Müge**, I have never seen such a big heart and soul full with love and positivity. You have been always there in the good and bad days, comforting me and telling me that everything is going to be alright. Thanks for being in my life and for letting me be a part of your life as well, and introducing yoga to my life. I will always be there for you as well, all the best of luck in completing your PhD. Love you all guys!

I owe my amazing friends and colleagues a debt of gratitude as well. I will start with

the old corner of our floor whom were really friendly when I first started my PhD. **Ilona**, **Dilek**, **Jinbao**, **Annelie**, **Luis**, **Upakul** and **Robin**; thanks for all the welcoming and friendly ambiance as well as scientific discussions. **Annelie**, **Ilona**, and **Robin**, thanks a lot for the nice company and help during my alcohol oxidation experiments. **Annelie**, **Clare** and **Ilona**; thanks for the support, in particular cooking help during my sickness. **Dilek**, thank you for all the useful information regarding the group and help in the beginning of my PhD, in particular during my illness. Your support and motivation was very meaningful.

The new members of my 4th floor corner, **Peter**, **Gang**, **Nazila**, **Jeroen**, **Sam**, **Rogier**, **Ramon** and **Frank**, thanks for the great working atmosphere. I had a chance to have short trips with my colleagues and to mention; Istanbul trip was so nice with you guys; **Nazila**, **Dilek**, **Peter**, **Ramon**, **Jeroen**, **Jinbao**, **Roy**, **Jespe**r, **JX** and **Rafael**, thanks for the good company and nice gifts. **Ramon**, **Jeroen**, **Gang** and **Peter**, thanks for all the great times during our trip to Madrid. **Sam**, **Gang**, **Peter** and **Dimitrije**; it was so nice to travel with you to Copenhagen. **Gang**, **Roy**, **Peter** and **Gang**, our trip to Luxembourg was really fun. My two traveling buddies; **Gang** and **Peter**; thank you for all the company to Stockholm and other cities in the Netherlands, those were great times. **Gang**, **Jesper**, **Ramon**, **Ara**, **David**, **Roy** and **Peter**, thanks for the amazing time in Winterberg.

Gang, you are a very special person with a great sense of humour and with a great depth inside. **Peter**, the master of faking an English accent with all these funny nature inside, thanks guys for all the laughs, drinks, dinners and competition during the NIOK CAIA exam. **Nazila**, thanks for all the scientific discussions and coffee breaks. **Ramon** and **Jeroen**, thanks for all the work related discussions and drinks. **Royje**, thanks for being this international friendly in the group and thanks for all the pool events, drinks, dinners and driving us around. **Roy** and **Jeroen**, your help for my Dutch summary was highly appreciated, thanks.

Zoran and **Jovana**, thanks for all the coffee breaks and talks, I really appreciated your support during this period. **Zoran**, **Upakul** and **Ines** dos, thanks for all the help at my one and only one incredible beam trip experience in Grenoble. **Joe**, thanks for being such a caring friend and for all the drinks, good times and effort to keep in touch as well as coffee breaks and many work related discussions. **Sang-ho**, my dear former colleague and neighbour, thanks for all the good times and being such a good friend and neighbour.

Me gustaría continuar en español para **Ana** y **Ara**. Querida **Ana**, tu apoyo y cuidado ayudaron mucho en el último año de mi doctorado. Gracias por todo. Mi guapa, querida **Ara**, mi compañía y el mayor apoyo después del final de mi contrato. No estoy seguro si podría hacerlo sin su apoyo. Te quiero mucho y estoy deseando

verte pronto. Gracias por estar ahí para mí.

Dear **Carlo**, thanks for all lab-related arrangements and introduction to the group when I first started. **Carlito**, thank you very much for all the help and support as well as work related discussions, coffee breaks, drinks, dinners, deep talks and laughs with **Gosia**. Thanks guys for being there for me.

Ilona, thanks for being such a caring and good friend. We had many coffee breaks, drinks, dinners, deep and fun talks, horse riding, yoga and many more. It has been a great delight to have you in my life. Thanks for all the support and motivation and my mom says hi and say hi to Rufus.

Dimitrije and **JX**, thanks for being there in my life, I feel so lucky to have you guys as my friends. **JX**, the greatest inspiration for me, a true friend with all the directness and honesty which made me get back to the straight line each time when I stumble. Thanks a lot for all the scientific discussions, support and motivation. You said you will be waiting for me at the finish line and see you soon there. **Mita**, your pure friendship and support as well as your great sense of humour made these years really great. Your sometimes harsh way of support and motivation made me stronger in this path. Thanks guys for all the support and caring attitude with all these deep talks, work related discussions, drinks, dinners and great company. Love you!

Last but not least, the special thanks go to the amazing parents that I have been so lucky to have and to whom this thesis is dedicated to, my dear mother, **Güngör** and father, **Metin**. My dear brother, **Mevlüt**, I would also like to acknowledge for his support. I will continue in Turkish to express my deepest gratitude for them. Canım **abiciğim**, mi hermanom, bu donem içinde çok fazla ben Türkiye'ye gelemesem de sen fazlasıyla geldin ve aile özlemimi gidermem de çok yardımcı oldun. Iyi ki varsın ve herşey için çok teşekkürler canım benim, seni çok seviyorum!

Anneciğim ve **babaciğim**, size her ne kadar teşekkür etsem az ve bu tez üzerinde emeğiniz çok büyük oldugundan bu tezi size armağan ediyorum. Her zaman yanımdaydınız, her ne kadar uzakta olsam da varlığınızı ve desteğinizi her zaman üzerimde hissettirdiniz. Benim annem ve babam olduğunuz ve beni koşulsuz bu kadar çok sevdiğiniz için çok teşekkürler. Zorlu bir dönemi sizin sayenizde atlatıyorum ve nice aydınlık güzel günlerimiz olacak. Sizleri çok seviyorum canlarım benim…

Zafer

CURRICULUM VITAE

Zafer Öztürk was born on 16th November 1983 in Ankara, Turkey. After graduating from Cumhuriyet Science High School, Ankara, Turkey in 2001, he began his undergraduate studies in Chemistry at the Middle East Technical University (METU), Ankara, Turkey in 2002. He performed his Bachelor thesis at the Condensed Matter and Interfaces (CMI) group under the supervision of Prof. dr. Daniël Vanmaekelbergh at Utrecht University, the Netherlands in 2007 with a thesis title of "Magic in Nanoscience: On the formation of binary nanoparticles of PbSe and CdSe and synthesis of thiol capped gold nanoparticles". He received his M.Sc. degree in Chemistry under the supervision of Prof. dr. Gulsun Gokagac from METU in 2011 with the thesis entitled "Carbon supported Platinum-Palladium Catalysts for Methanol and Ethanol Oxidation Reactions". During his M.Sc. studies he received a research scholarship by the Scientific and Technological Research Council of Turkey (TUBITAK). Between the years of 2011 and 2012, he was a PhD candidate in Polymer Science and Technology Department at METU. In March 2012, He began his PhD research in the group of Inorganic Chemistry and Catalysis, Utrecht University, the Netherlands under the supervision of Prof. dr. ir. Bert M. Weckhuysen. In August and October 2012, he was a visiting scientist in the National Institute of Chemistry, Ljubljana, Slovenia and in the Ruhr Universitat Bochum, Bochum, Germany, respectively. The most significant findings of his PhD research on "Spectroscopy and Microscopy on the Formation of Zeolitic Imidazolate Frameworks" are described in this thesis text.